Department of Physics and Astronomy

University of Heidelberg

Master thesis

in Physics

submitted by

Lina Norton

born in Munich

June 2015

Determination of the branching fraction

and

a new method for reconstructing

$B^{\pm} \rightarrow K^*(892)^{\pm}\mu^+\mu^-$ decays at LHCb

This master thesis was put forward by
Lina Norton
at the
Physikalisches Institut
under the supervision of
Prof. Dr. Ulrich Uwer
and
Dr. Michel De Cian

ABSTRACT

In this thesis, the branching fraction of the rare decay $B^{\pm} \to K^{*\pm} (\to K^{\pm} \pi^0) \mu^+ \mu^-$ is determined relative to the decay $B^{\pm} \to K^{*\pm} (\to K^{\pm} \pi^0) J/\psi (\to \mu^+ \mu^-)$ using data taken at the LHCb detector in 2011 and 2012, corresponding to $3\,\text{fb}^{-1}$. 65 ± 21 reconstructed B^+ mesons were determined from the $B^+ \to K^{*+} \mu^+ \mu^-$ decay with a statistical significance of 3.23σ. Using the known branching fraction of the reference decay [1], the absolute branching fraction is determined to be:

$$\mathcal{B}(B^+ \to K^{*+}\mu^+\mu^-) = (1.02 \pm 0.33(\text{stat.})) \times 10^{-6}.$$

The reconstruction of the neutral pion suffers from low reconstruction efficiencies resulting in a large statistical uncertainty of the obtained branching fraction. This motivates the use of a new method to reconstruct the neutral pion from decay kinematics. This method has been developed and tested in the course of this thesis. While the efficiency to reconstruct neutral pions significantly improves, the method results into additional background.

ZUSAMMENFASSUNG

In dieser Arbeit wird das Verzweigungsverhältnis des seltenen Zerfalls $B^{\pm} \to K^{*\pm}$ $(\to K^{\pm} \pi^0) \mu^+ \mu^-$ relativ zum Zerfall $B^{\pm} \to K^{*\pm} (\to K^{\pm} \pi^0) J/\psi (\to \mu^+ \mu^-)$ bestimmt. Es werden dabei Daten ausgewertet, welche 2011 und 2012 am LHCb Detektor aufgenommen wurden, was einer integrierten Luminosität von $3\,\text{fb}^{-1}$ entspricht. Es wurden 65 ± 21 rekonstruierte B^+ Mesonen aus dem $B^+ \to K^{*+} \mu^+$ μ^- Zerfall mit einer Signifikanz von 3.23σ nachgewiesen. Mit dem Literaturwert des Verzweigungsverhältnisses des Referenzkanals [1] wird das absolute Verzweigungsverhältnis wird zu

$$\mathcal{B}(B^+ \to K^{*+}\mu^+\mu^-) = (1.02 \pm 0.33(\text{stat.})) \times 10^{-6}$$

bestimmt.
Die Rekonstruktion des neutralen Pions geht mit geringen Rekonstruktionseffizienzen einher, was sich in einer großen statistischen Unsicherheit im Verzweigungsverhältnis widerspiegelt. Diese Tatsache motiviert den Einsatz einer neuen Methode, in der das neutrale Pion aus der Zerfallskinematik rekonstruiert wird. In dieser Arbeit wird diese Methode präsentiert und die Realisierbarkeit im Detail diskutiert. Während sich die Effizienz $B^+ \to K^{*+} J/\psi$ Zerfälle zu rekonstruieren signifikant verbessert, führt die Methode zu zusätzlichem Untergrund.

CONTENTS

INTRODUCTION

The Standard Model of particle physics describes the fundamental particles and their interactions by weak, strong and electromagnetic forces. Since its development in the 1970s it has become a well-tested physics theory. However, incorporating the general theory of relativity into this framework has proven to be a difficult challenge. Moreover, the Standard Model lacks an explanation of the nature of Dark Matter, which, from experimental observations, is known to account for a vast fraction of the visible universe. The matter-antimatter imbalance in the universe also is an unanswered question. This makes people believe that the Standard Model is an effective theory of a more general picture which would lead to new phenomena at higher energies. Possible new phenomena are probed in many high - energy physics experiments throughout the entire world. Currently, some of the most important experiments trying to discover physics beyond the Standard Model are located at the Large Hadron Collider (LHC) at CERN, near Geneva, Switzerland. While the ATLAS and CMS experiment look directly for new physics produced in the high-energy collisions, the LHC also provides the possibility to search for new effects indirectly such as in Flavor Changing Neutral Currents (FCNCs). These currents are highly suppressed in the Standard Model but their occurrence could be enhanced by higher-order contributions which involve possible new particles. FCNCs can occur in rare decays of B mesons [2]. As the abundance of these rare decays is very low, it is crucial to obtain a large number reconstructed B decays. The LHCb detector is designed to reconstruct B and D hadron decays with high precision from the copious quantity of approximately 10^{11} $b\overline{b}$ pairs produced in a nominal running period at the LHC [3][4].

This thesis focuses on the reconstruction of the rare decay[1] $B^+ \rightarrow K^{*+} (\rightarrow K^+ \pi^0) \mu^+ \mu^-$. A relative branching fraction for this decay is determined by fully reconstructing the final state, i.e. all decay products in the detector are reconstructed. The reference channel is the resonant decay $B^+ \rightarrow K^{*+} J/\psi$. The data which is used to determine the relative branching ratio the was taken at the LHC in 2011 and 2012 with center-of-mass energies of $\sqrt{s} = 7\,\text{TeV}$ and $\sqrt{s} = 8\,\text{TeV}$, respectively. The total integrated luminosity of these data samples is approximately $3\,\text{fb}^{-1}$. While the reconstruction of charged muons and kaons works well at LHCb, the reconstruction of neutral particles, such as the neutral pion, faces experimental challenges [5], which results in a low signal yield and high statistical uncertainties. In a different approach this thesis tries to reconstruct the π^0 from decay kinematics. This procedure is referred to as *partial reconstruction* and can generally be applied to B decays with an intermediate resonance and the knowledge of the flight di-

---

1 Charge conjugation is implied throughout this document unless stated otherwise.

rection of the b hadron. In this thesis, the concept of this technique is presented and its feasibility tested on a simulated signal sample of $B^+ \to K^{*+} J/\psi$ decays. Furthermore, the partial reconstruction method is evaluated on measured and simulated data.

A short overview of this thesis:
Following a brief introduction to rare B decays with focus on the electroweak penguin decay $B^+ \to K^{*+} \mu^+ \mu^-$ in chapter 1, chapter 2 describes production and decay of B mesons. Chapter 3 presents the LHCb detector and its components. Chapter 4 focuses on the full reconstruction and provides a detailed description of the selection process of $B^+ \to K^{*+} \mu^+ \mu^-$ candidates. The result of the selection process is discussed in chapter 5. Furthermore, the branching fraction $\mathcal{B}(B^+ \to K^{*+}\mu\mu)$ is determined. After discussing the full reconstruction, chapter 6 addresses the partial reconstruction method and its procedure is explained in detail. Feasibility studies are performed on a simulated data sample and the efficiency to reconstruct $B^+ \to K^{*+} J/\psi$ decays is determined. In chapter 7 the method is applied to a real data sample as well as a simulated sample to evaluate its feasibility. The latter is a simulation "cocktail" which approximately reflects the contents of the real data, making it possible to examine whether this method can be used as an alternative concept in the reconstruction of $B^+ \to K^{*+} \mu^+ \mu^-$ decays.

RARE DECAYS OF B MESONS

In this chapter, the important theoretical aspects underlying this thesis are explained. After a short introduction to the Standard Model of Particle Physics, the further part is committed to flavor physics. The concepts are briefly explained and a more detailed illustration can be found in many textbooks and publications.

1.1 THE STANDARD MODEL OF PARTICLE PHYSICS

The Standard Model of Particle Physics is a Quantum Field Theory which explains the interplay between strong, electromagnetic and weak forces, though lacking a complete explanation of Dark Matter and gravity. Also the baryon asymmetry[1] in the universe is a puzzle which cannot be explained by the Standard Model.

1.1.1 *Fundamental Particles*

The fundamental particles can be split into three groups: Fermions (Spin 1/2), gauge bosons (Spin 1) and the scalar Higgs boson (Spin 0). While the fermions are the building blocks of matter, the gauge bosons are responsible for the mediation of fundamental forces and the Higgs boson for the mass of the fermions and massive gauge bosons. The latter can be divided into two more groups, quarks and leptons, depending on their interactions. Quarks and leptons each consist of three generations with two particles accompanied by a differentiating property called flavor. Including the antiparticles which solely have a different charge than the corresponding particles, this amounts to a total number of 24 fundamental particles. Quarks carry color, weak and electromagnetic charge and thus participate in all fundamental interactions. Leptons, on the other hand, have weak charge, and electron, muon and taon additional electromagnetic charge, while the corresponding neutrinos are neutral particles. The photon, the eight gluons as well as the $W^{\pm}$ and Z^0 belong to the category of gauge bosons. The photon couples to the electric charge and plays the role of the electromagnetic mediator. The gluons couple to the color charge and function as the carrier of the strong interaction. Since they also possess color charge, gluon-gluon coupling is possible. The weak interaction is mediated by the $W^{\pm}$ and Z^0 bosons. All fundamental particles as well as their charge and mass are listed in Figure 1.
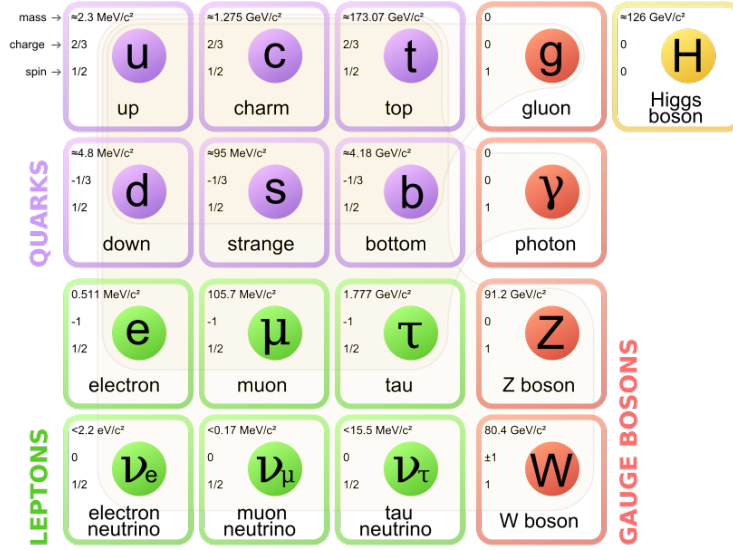
---

1 matter-antimatter asymmetry

Figure 1: The fundamental particles with their individual mass and charge. Figure from [6].

1.2   FLAVOR PHYSICS

In the electroweak interaction the quark eigenstates (d', s', b') are not equivalent to the mass eigenstates (d, s, b) which gives rise to a transformation between these two eigenstates. This transformation can be described by a unitary matrix, the so-called Cabibbo-Kobayashi-Maskawa (CKM) matrix V_{CKM}:

$$\begin{pmatrix} d' \\ s' \\ b' \end{pmatrix} = \begin{pmatrix} V_{ud} & V_{us} & V_{ub} \\ V_{cd} & V_{cs} & V_{cb} \\ V_{td} & V_{ts} & V_{tb} \end{pmatrix} \begin{pmatrix} d \\ s \\ b \end{pmatrix}.$$

The probability of the flavor eigenstate i to decay into flavor eigenstate j is proportional to $|V_{ij}|$. The V_{CKM} matrix can be complex, which results in 18 free parameters. Due to the unitarity relation $V_{CKM}(V_{CKM})\dagger$, these parameters can be reduced to nine, while another five of the parameters can be absorbed into non-observable quark phases. Consequently, the matrix can be parametrized by three Euler angles Θ_{12}, Θ_{23} and Θ_{31} and the phase δ. This results in following representation of V_{CKM}:

$$V_{CKM} = \begin{pmatrix} c_{12}c_{13} & s_{12}c_{13} & s_{13}e^{-i\delta} \\ -s_{12}c_{23} - c_{12}s_{23}s_{13}e^{i\delta} & c_{12}c_{23} - s_{12}s_{23}s_{13}e^{i\delta} & s_{23}c_{13} \\ s_{12}c_{23} - c_{12}s_{23}s_{13}e^{i\delta} & -c_{12}s_{23} - s_{12}c_{23}s_{13}e^{i\delta} & c_{23}c_{13} \end{pmatrix}$$

with $s_{ij} = \sin\Theta_{ij}$ and $c_{ij} = \cos\Theta_{ij}$. The phase δ is responsible for *CP violating* effects in flavour-changing processes within the SM. CP violation[2] is a necessary condition to explain the observed matter-antimatter asymmetry in our universe. The Standard Model prediction of CP violation in terms of the complex phase of the CKM matrix is several orders of magnitude too small to explain the observed excess of matter over antimatter. Therefore, new sources of CP violation must exist. Experiments have shown that $s_{13} \ll s_{23} \ll s_{12}$. Implementing this in V_{CKM}, the hierarchy of the matrix elements are demonstrated in the so-called Wolfenstein parametrization. By using $s_{12} = \lambda$, $s_{23} = A\lambda^2$ and $s_{13}e^{-\delta} = A\lambda^3(\rho + i\eta)$, this results in:

$$V_{CKM} = \begin{pmatrix} 1 - \frac{1}{2}\lambda^2 & \lambda & A\lambda^3(\rho - i\eta) \\ -\lambda & 1 - \frac{1}{2}\lambda^2 & A\lambda^2 \\ A\lambda^3(1 - \rho - i\eta) & -A\lambda^2 & 1 \end{pmatrix} + \mathcal{O}(\lambda^4).$$

The parameter λ is related to the two-generation mixing angle Θ_C by $\lambda = \sin\Theta_C = |V_{us}|$. The value of λ is a crucial ingredient when testing the unitarity of the CKM matrix

$$|V_{ud}|^2 + |V_{us}|^2 + |V_{ub}|^2 = 1.$$

The current value for λ is: $\lambda \approx 0.23$ [1]. Inserting this value into the Wolfenstein-parametrized CKM matrix demonstrates the hierarchy of the matrix elements: off-diagonal elements are small, while diagonal elements are close to 1.

1.3 PENGUIN DECAYS OF B MESONS

Transitions between different d-type or u-type quarks which are mediated by neutral currents[3] are forbidden at tree-level by the Standard Model. By introducing higher order contributions, called quantum loops, FCNC such as the transition of a b quark to a d quark or an s quark can occur. These processes involve at least two charged flavor-changing currents, and since each current between two quark families is suppressed by the corresponding CKM matrix element, their abundance is much lower than the tree-level ones. Originating in a bet during a game of darts, a group of physicists at CERN started referring to these types of rare[4] decays as "penguin" decays [8].

The study of these penguin diagrams is especially interesting for studying non-

---

2 C denotes charge conjugation and P parity transformation. The CP transformation describes the transition between particles and antiparticles. CP-violation describes the effect that particles have different properties than their antiparticles.

3 These currents are therefore called flavor-changing neutral currents (FCNC).

4 All B- meson decays that do not occur through the $b \to c$ transition are usually denoted as rare B decays, including both semileptonic and hadronic tree-level $b \to u$ processes as well as high-order $b \to s$ (d) decays including electroweak and gluonic penguin decays [7]

Standard Model effects, since loop decays are highly suppressed in the Standard Model and are therefore sensitive to new effects. The loops are formed by the heaviest off-shell particles t and W, changing the flavor of the quark content of the decaying particle twice under the emission and reabsorbation of the particle mediating the loop[5]. A measurement of an enhanced branching ratio compared to the Standard Model prediction therefore can be an indicator for the contribution of *new physics*[6] such as particles from supersymmetric models or non-standard model extensions such as the charged Higgs [2].

In the $B^+ \rightarrow K^{*+} \mu^+ \mu^-$ decay, the quantum loop of the weak FCNC transition $\bar{b} \rightarrow \bar{s}$ exchanges a virtual W boson, which itself can emit a Z^0 or a virtual photon, decaying into a pair of leptons. This type of decay can occur in the form of an electroweak penguin or box diagram. The corresponding Feynman diagrams are depicted in Figure 2. Non-Standard Model contributions can occur, for instance, by the exchange of new particles such as the charged Higgs in a supersymmetric model [9] as shown in the Feynman diagram d) in Figure 2.
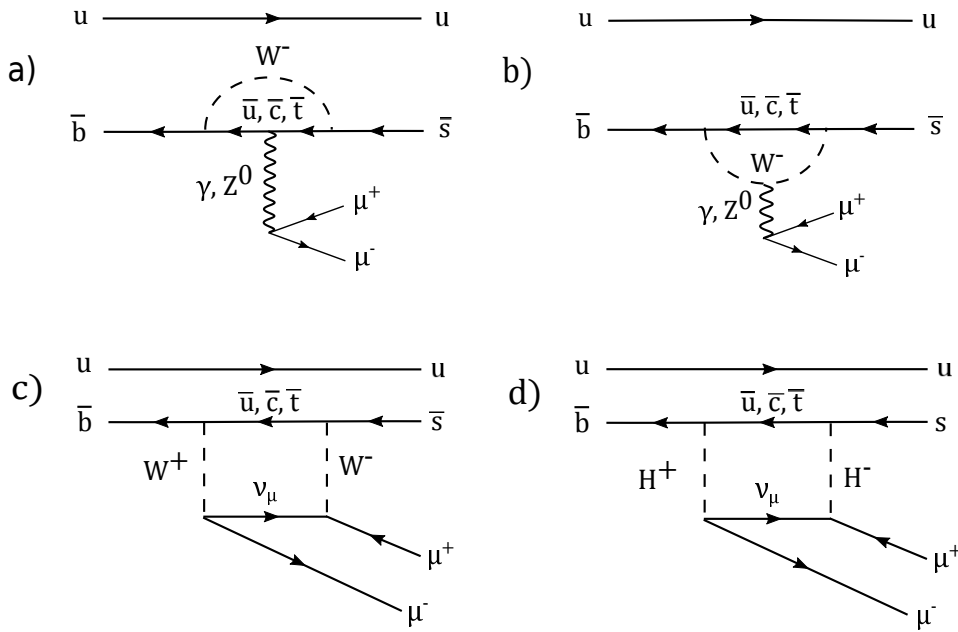
Figure 2: Electroweak penguin diagrams for $B^+ \rightarrow K^{*+} \mu^+ \mu^-$. a) and b) show Standard Model contributions, c) shows a Standard Model box diagram, d) a box diagram with charged Higgs exchange corresponding to a supersymmetric model.

---

5 The loops can also include other quarks; since the mass of the top quark is more than 100 times heavier than the charm quark, the transition amplitudes in the Standard Model are dominated by transitions involving virtual top quarks.

6 New physics refers to any process which cannot be described by the Standard Model.

In this analysis, the relative branching ratio $\frac{\mathcal{B}(B^+ \to K^{*+}\mu\mu)}{\mathcal{B}(B^+ \to K^{*+}J/\psi)}$ is determined. The charmonium mode $B^+ \to K^{*+}$ J/ψ, which is used as the reference channel, has a branching ratio of [1]

$$\mathcal{B}(B^+ \to K^{*+} J/\psi) = (1.44 \pm 0.08) \times 10^{-3}.$$

The absolute branching fraction of the non-resonant $B^+ \to K^{*+} \mu^+ \mu^-$ decay stated by the Particle Data Group (PDG) is [1]

$$\mathcal{B}(B^+ \to K^{*+}\mu\mu) = (1.12 \pm 0.15) \times 10^{-6}.$$

Various B physics collaborations have experimentally determined this non-resonant branching fraction. Measurements from LHCb and BaBar, for instance, result in $\mathcal{B}(B^+ \to K^{*+}\mu\mu) = (1.16 \pm 0.19) \times 10^{-6}$ [10] and $\mathcal{B}(B^+ \to K^{*+}\mu\mu) = (1.46^{+0.79}_{-0.75} \pm 0.12) \times 10^{-6}$ [11].

The branching fractions of B^+ decays into two oppositely charged muons are well predicted by the Standard Model. On the other hand, several theories that extend the Standard Model, like supersymmetry, allow significant modifications to these branching fractions and therefore an observation of any significant deviation from the Standard Model prediction would indicate a discovery of new effects.

Decays of the B mesons into an excited kaon and a dimuon pair[7], $B \to K^*\mu\mu$, are considered an important channel for new physics searches. However, theoretical predictions suffer from large uncertainties. To maximize sensitivity, observables can be constructed from ratios or asymmetries where the leading uncertainties cancel which makes the measurement of CP asymmetries more reliably to be predicted than the total branching fractions.

For instance, the direct CP asymmetry A_{CP} of the decay $B^+ \to K^{*+} \mu \mu$ and $B^- \to K^{*-} \mu \mu$ is defined as:

$$A_{CP} = \frac{\mathcal{B}(B^- \to K^{*-}\mu\mu) - \mathcal{B}(B^+ \to K^{*+}\mu\mu)}{\mathcal{B}(B^- \to K^{*-}\mu\mu) + \mathcal{B}(B^+ \to K^{*+}\mu\mu)}.$$

A_{CP} is expected to be $\mathcal{O}(10^{-3})$ in the Standard Model, but new physics could produce a significant enhancement [12].

Another source of a possible new physics manifestation is the weak isospin[8] asymmetry, which is the difference in the measurements of the $B^+ \to K^{*+} \mu \mu$ decay and the isospin "partner" decay $B^0 \to K^{*0} \mu \mu$. The isospin asymmetry A_I is defined as:

$$A_I = \frac{\mathcal{B}(B^0 \to K^{*0}\mu\mu) - r\mathcal{B}(B^\pm \to K^{*\pm}\mu\mu)}{\mathcal{B}(B^0 \to K^{*0}\mu\mu) - r\mathcal{B}(B^\pm \to K^{*\pm}\mu\mu)},$$

---

7 The B meson and the K* meson can be neutral, have positive charge or negative charge.
8 The weak isospin is not explained in detail at this point, though detailed information can be found in many textbooks [13] [14].

where $r = \tau_0/\tau_+$ is the ratio of B^0 and B^+ lifetimes. The Standard Model calculations predict this isospin asymmetry to be $\mathcal{O}(1\%)$ [15] in the dimuon mass squared region, q^2, below the J/ψ resonance. As q_2 approaches zero, the isospin asymmetry of $B \to K^* \mu \mu$ is expected to be around $(5 \pm 3)\%$ [16]. A deviation from the Standard Model prediction can also here be a indication for new physics. Recent measurements from LHCb [15] are consistent with Standard Model expectations. The results are shown in Figure 3.
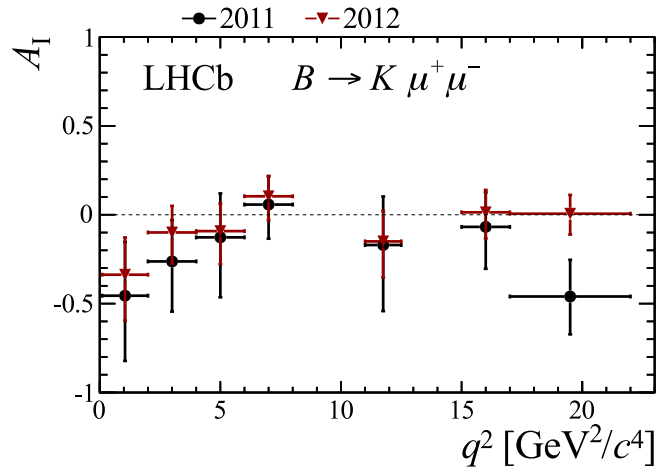

Figure 3: Isospin asymmetry of $B \to K^* \mu \mu$ obtained separately from data sets recorded at LHCb in 2011 and 2012. Figure from [15].

PRODUCTION AND DECAY

The detection and reconstruction of hadrons containing beauty quarks is one of the key aspects which motivated the design of the LHCb detector. This chapter concisely denotes the production of b quarks as well as the decay kinematics of the heavy flavored beauty hadrons.

2.1 B PRODUCTION

At proton-proton colliders, quark-antiquark annihilation and gluon fusion are the leading-order production mechanisms of $b\bar{b}$ pairs. The Feynman diagrams for these processes are shown in Figure 4 where a) corresponds to the annihilation process and b) to gluon fusion. For center-of-mass energies at the TeV scale, next-to-leading order (NLO) contributions such as flavor excitations and gluon splitting become increasingly important. At $\sqrt{s} = 7\,\text{TeV}$, the operating energy of the LHC in 2011, the dominant process is flavor excitation [17], the corresponding Feynman diagrams are depicted in figures c) and d).

Compared to the available energies in the TeV scale, the mass of a b quark ($\approx$ 4.2 GeV) is small. Considering the parton density functions of the proton, a low momentum fraction corresponds to a large gluon density [18]. Statistically it is more likely to find two gluons or $q\bar{q}$ pairs with different momentum fractions which results in a boost of the created $b\bar{b}$ pair in the direction of the beam axis, predominantly producing them in the forward or backward direction as depicted in Figure 5.
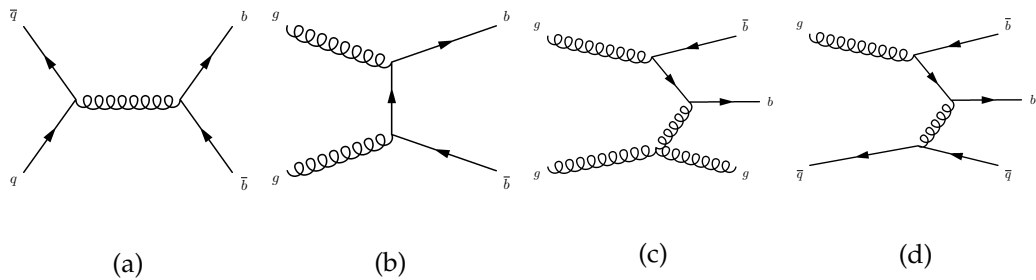

(a) (b) (c) (d)

Figure 4: Feynman diagrams for the production of $b\bar{b}$ pairs at the LHC. Figures a) and b) show exemplary diagrams for quark-antiquark annihilation and gluon fusion, respectively. Figures c) and d) show Next-to-leading-order contributions from flavor excitation. Figures taken from [19].
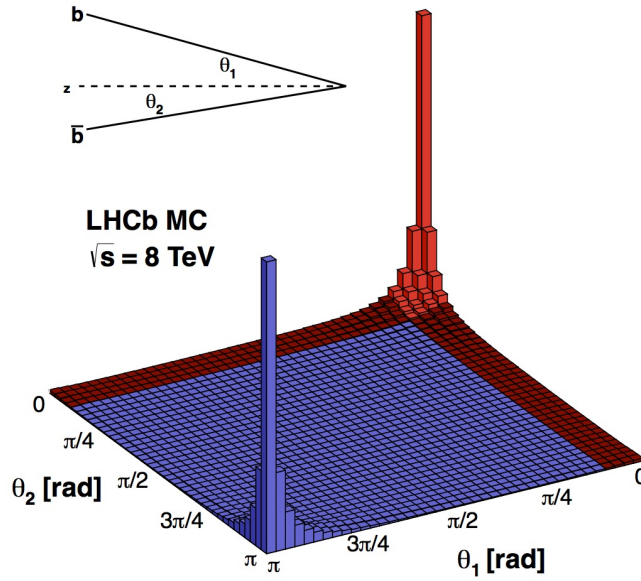
Figure 5: Correlation of the polar angle for simulated $b\bar{b}$ events. The LHCb angular acceptance is shown in red [20].

2.2   DECAY TOPOLOGY AND EXPERIMENTAL OBSERVABLES

Figure 6 shows the topology of the $B^+ \to K^{*+} (\to K^+ \pi^0) \mu^+ \mu^-$ decay chain. With a decay time of approximately 1.638×10^{-12}s [1], corresponding to a decay length of $c/\tau = 491.4\,\mu$m in the rest frame, the B^+ has a relatively long lifetime. Considering the Lorentz boost, the meson travels several millimeters from the *primary vertex* until it decays at the *secondary vertex*. The primary vertex is the position of the primary pp interaction. The muons, kaons and pions do not decay within the detector and are therefore considered stable particles. The heavy decay products K^{*+} and J/ψ on the other hand, dominantly decay via the strong interaction and are very short-lived particles[1]. The decay time of K^{*+} amounts to only $\tau \approx \frac{\hbar}{\Gamma} = 10^{-23}$s. It can therefore be assumed to decay instantaneously into a K^+ and π^0. Since neither the flight distance of K^{*+} nor that of J/ψ can be resolved, the secondary vertex represents the effective vertex of all the final state particles in decays of the type $B^+ \to K^{*+} (\to K^+ \pi^0) J/\psi (\to \mu^+ \mu^-)$. In the full reconstruction of a decay chain, every daughter particle is reconstructed. In the $B^+ \to K^{*+} \mu^+ \mu^-$ decay, with the intermediate resonance $K^{*+} \to K^+ \pi^0$, this implies the reconstruction of the four daughter particles μ^+, μ^-, K^+ and π^0. In contrast to the three charged particles, the π^0 does not have a track associated to it. It decays into two photons which are reconstructed in the electromagnetic calorimeter. This is explained in the following chapter and the selection of π^0 candidates is also treated in Chapter 5.

---

[1] More than 87% of the J/ψ mesons and more than 99% of the K^{*+} mesons decay via the strong interaction.
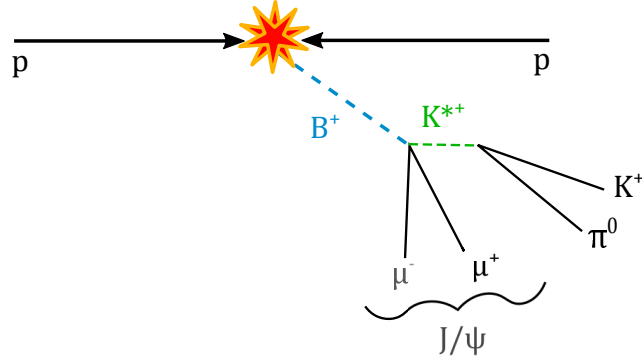
Figure 6: Illustration of the decay topology $B^+ \rightarrow K^{*+} \mu^+ \mu^-$. The K^{*+} is a short-lived resonance and is therefore assumed to decay immediately.

The four momentum of a particle can be expressed through the energy[2] $E^2 = m^2 + \vec{p}^2$ with the three momentum $\vec{p}$. As the mass m of a particle is not measured in the detector, it is assigned the constant PDG (Particle Data Group [1]) mass of the corresponding particle hypothesis. This results in the four momentum of the particle:

$$p = \begin{pmatrix} E \\ \vec{p} \end{pmatrix} = \begin{pmatrix} m_{PDG}^2 + p^2 \\ \vec{p} \end{pmatrix}. \tag{1}$$

---

[2] Natural units are used in the following, i.e. $c = 1$).

THE LHCB EXPERIMENT

3.1 THE LARGE HADRON COLLIDER

The Large Hadron Collider, built by the European Organization for Nuclear Research, is the largest single machine in the world. Its operation requires a complex arrangement of accelerator systems. The four main experiments ALICE, ATLAS, CMS and LHCb are positioned along the 26.7 km long tunnel where two counter - rotating beams of protons or heavy ions collide (see Figure 7). The collisions take place at a frequency of 40 MHz. The proton beams were collided at an energy of 3.5 TeV per beam in 2010 and 2011 and at 4 TeV in 2012. For a time period of two months, the LHC also collided protons and lead ions in 2013. The LHC has been upgraded in the recent years in order to achieve higher proton beam energies, continuously increasing the center-of-mass energy up to $\sqrt{s} = 14$ TeV.
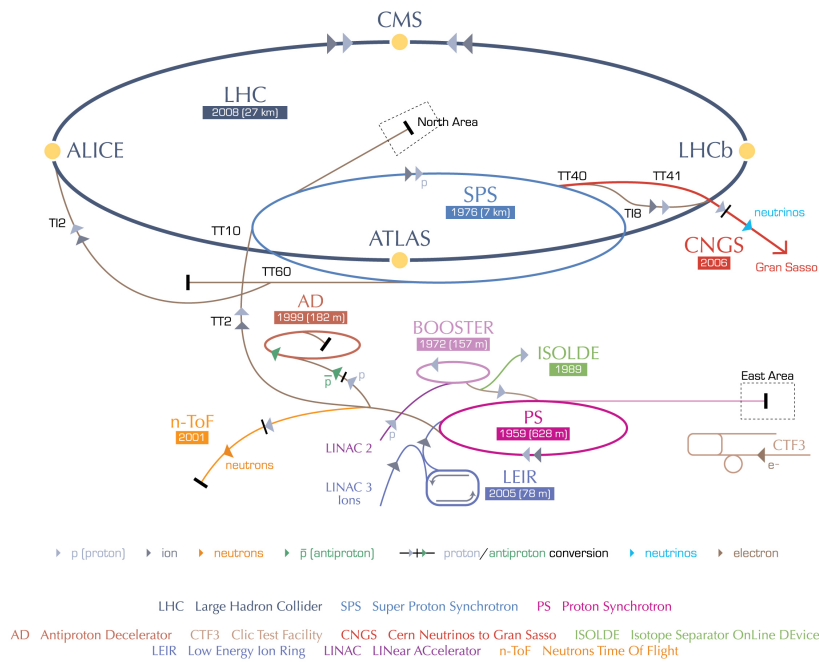
3.2 THE LHCb DETECTOR

The *Large Hadron Collider beauty* (LHCb) detector [22] has been designed to perform measurements on b and c hadrons. As the heavy b hadrons are mainly produced in the forward and backward direction, the LHCb detector (Figure 8) is built as a single-arm forward spectrometer. The geometrical acceptance of the detector ranges from 10 to 300 mrad in the bending plane of the dipole magnet (x-z-plane) and from 10 to 250 mrad in the non-bending plane (y-z-plane). This is equivalent to a pseudo-rapidity of $2 < \eta < 5$[1] (see below). It is advantageous to introduce the coordinate system used for the description of orientation of the LHCb detector elements (see also Figure 8). This coordinate system is a right-handed Cartesian system with z-axis along the beam and y-axis pointing vertically upwards[2]. From this, a spherical coordinate system can also be deduced, with an azimuthal and polar angle indicated by ϕ and θ, respectively, where the polar angle also defines the pseudorapidity: $\eta = -\ln \tan(\theta/2)$.

Heavy flavor mesons flying in the forward direction are highly boosted and travel measurable distances in the detector before they decay. Several subsystems allow for high-resolution track reconstruction, measurement of energy and momentum as well as particle identification. For the reconstruction of a specific decay chain, primary and secondary vertices must be known precisely, which requires clean and distinct track reconstruction. When the proton beams are slightly defocused in

---

1 The magnetic field provided by a large dipole magnet deflects particles in the x-direction. The x-z-plane of the corresponding trajectories is called the bending plane.

2 As a result, the x-axis points away from the center of the beam ring

Figure 7: CERN's accelerator complex and the four main experiments [21].

the intersection point of the LHCb detector, an average of 1.7 primary interactions per bunch crossing can be achieved [23], which makes the reconstruction of the primary vertex easier. The corresponding luminosity is $L = 4 \cdot 10^{32} \, \mathrm{cm}^{-2} \mathrm{s}^{-1}$. Figure 9 shows the integrated luminosities as a function of time in several data-taking periods, split into the delivered and the recorded luminosity. The total integrated luminosity recorded by the detector was approximately $40 \, \mathrm{pb}^{-1}$, $1 \, \mathrm{fb}^{-1}$ and $2 \, \mathrm{fb}^{-1}$ during 2010, 2011 and 2012, respectively.

3.3 THE TRACKING SYSTEM

The momentum and charge of a charged particle can be determined by measuring the deflection of its trajectory when it traverses a magnetic field. In the LHCb detector, this is done with a system of four sub-detectors and a dipole magnet [24]. The tracking system is comprised by the Vertex Locator (VELO), the Tracker Turicensis (TT) and the Tracking Stations (T1- T3), which include the Inner Tracker (IT) and the Outer Tracker (OT). The dipole magnet is located between the TT and the Tracking Stations. The orientation of its magnetic field points in y-direction. This magnet provides an integrated field strength of $\int B \, dl = 4 \, \mathrm{Tm}$ for a track of $10 \, \mathrm{m}$ length in z-direction. Charged particles flying in the forward direction are deflected in the $x - z$-plane. The magnet polarity is switched regularly, allowing the study of systematic effects related to potential asymmetries of the detector.
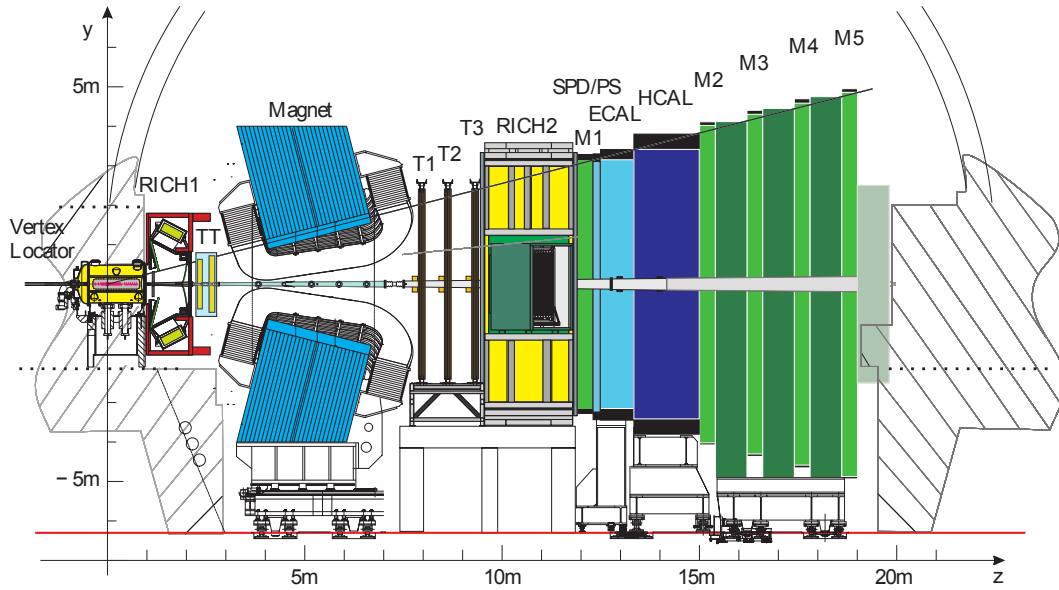
Figure 8: Schematic side view of the LHCb detector. [22]. The shown subdetectors (from left to right) are: Vertex Locator (VELO), RICH1, Tracker Turicensis (TT), the dipole magnet, the inner and outer trackers (T1-T3), RICH2, the Scintillating Pad Detector (SPD), the Preshower Detector (PS), the electromagnetic calorimeter (ECAL) and the hadronic calorimeter (HCAL) and the muon chambers (M1-M5).

3.4 VERTEX LOCATOR

The Vertex Locator (VELO) [25] is located closest to the interaction point and is designed to determine the position of the primary pp interaction, known as the primary vertex and to distinguish it from displaced vertices which originate in secondary decays or other primary vertices from additional pp collisions within the same event, called pile-up interactions. It also measures the secondary vertex, which is the decay vertex of the heavy flavored hadrons. The VELO provides the first measurements of the trajectories of charged particles which can be used as an independent segment in the track reconstruction.

Many light particles such as kaons and pions, as well as the B mesons, are formed at the primary vertex, which is determined with a resolution of $40\,\mu m$ in the direction of the beam and $10\,\mu m$ in the transverse direction. As B mesons can only decay via the weak interaction resulting in large lifetimes of $\sim 1\,ps$, and the high boost of the created particles, b hadrons travel measurable distances before decaying at the secondary vertex.

The VELO consists of 21 stations, which are divided into two semicircle shaped modules (see Figure 10). The modules can be displaced by 3 cm from the beam axis in order to avoid damage to the sensitive sensors during the injection phase. The stations have a thickness of $300\,\mu m$ and consist of two different types of silicon-strip sensors. The R-sensor measures radial distances of the particles to the beam axis, while ϕ-sensors measure the azimuthal angle ϕ of a track. Both types of sensors are situated along the z-axis, in order to determine the position in this
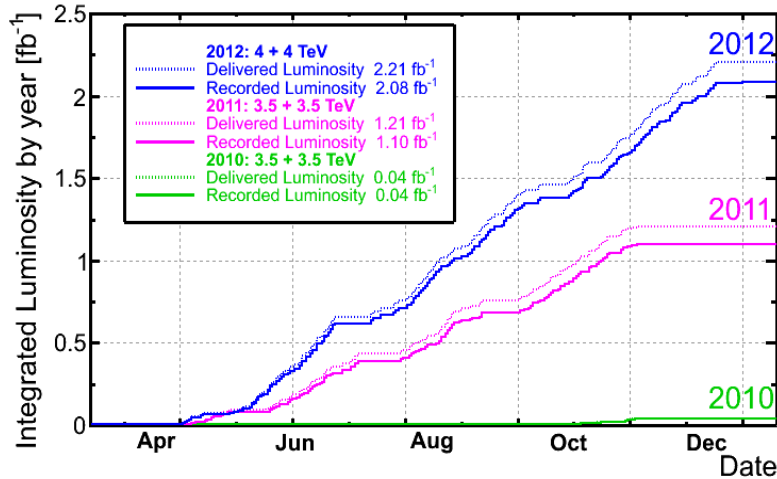
Figure 9: The luminosity by the LHCb detector as a function of time, showing separately the delivered and recorded luminosity for the different data-taking periods 2010, 2011 and 2012 [20].

third dimension. Another four R-stations are placed beyond the interaction point in negative z-direction. These form the pile-up veto station, which are designed for vetoing pile-up events.

3.5 TRACKER TURICENSIS

The TT [22] is located before the dipole magnet and behind the first Ring Imaging Cherenkov Detector (RICH) in the direction of the outgoing particles. It it designed for momentum measurement of charged particles with low energies, such as kaons and pions, since these are deflected by the strong magnetic field of the magnet and might also end up outside the acceptance of the tracking stations.

The TT consists of four single-sided detector layers each of which are composed of silicon strips. The first and fourth layer lie parallel to the y-axis while the central layers are rotated by $\pm 5°$ relative to the two vertical layers as shown in Figure 11. This is done to measure the y-coordinate of the particles and thus allow three-dimensional measurements. The spatial resolution equals approximately $50\,\mu m$. The total size amounts to $150\,cm$ in width and $130\,cm$ in height.

3.6 INNER AND OUTER TRACKER

The three main tracking stations T1, T2 and T3 are located downstream of the magnet. Due to a high particle flux near the beam pipe, the tracking stations consist of an inner part, the Inner Tracker (IT) [27] and an outer part, the Outer Tracker (OT) [28]. The Inner Tracker covers a cross-shaped region with $120\,cm$ in width and $40\,cm$ in height and is located closest to the beam pipe. Just like the Tracker Turicensis, the IT consists of silicium microstrip sensors, providing a spatial reso-
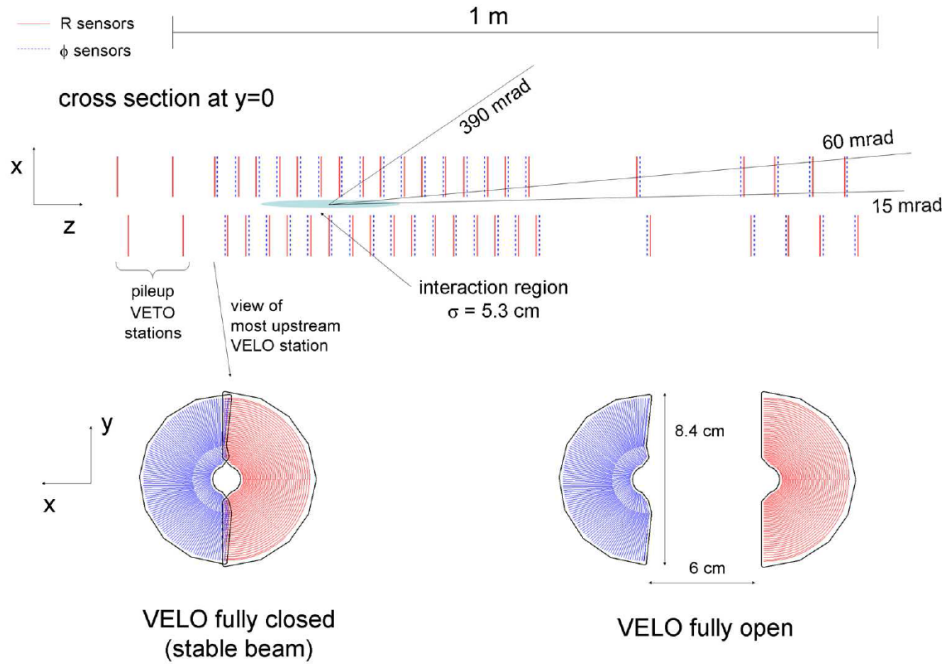
Figure 10: The upper part shows a schematic view of the 21 VELO stations and the two pileup veto stations in the x-z plane at y=0 The lower part denotes a station consisting of two semicircle modules. When the beam is unstable, the two parts can can be separated [22].
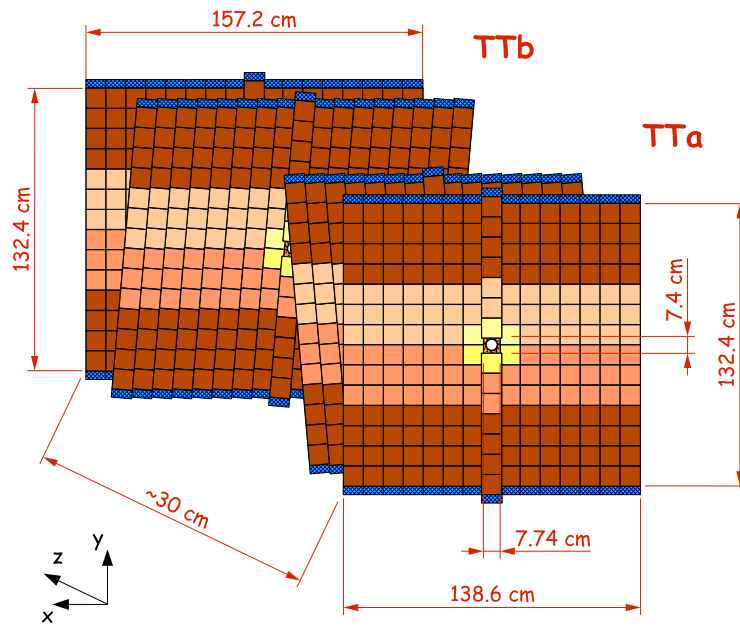
Figure 11: Geometry of the TT. Figure from [26].

lution of 50 μm, which are located around the beam pipe in the shape of a cross, as visualized in Figure 12.

The IT is surrounded by the Outer Tracker which covers the large area outside of the IT acceptance. It is comprised of an array of straw tubes (see Figure 13), which are filled with a special Ar-CO_2 mixture providing a fast maximum drift time of

43 ns which is necessary to reduce the overflow if the LHC is operated at a 25ns bunch spacing. With a spatial resolution of 200 μm [29], the performance is not as good as for the IT, but with an area of 6m × 5m, the area covered by the OT is much larger.
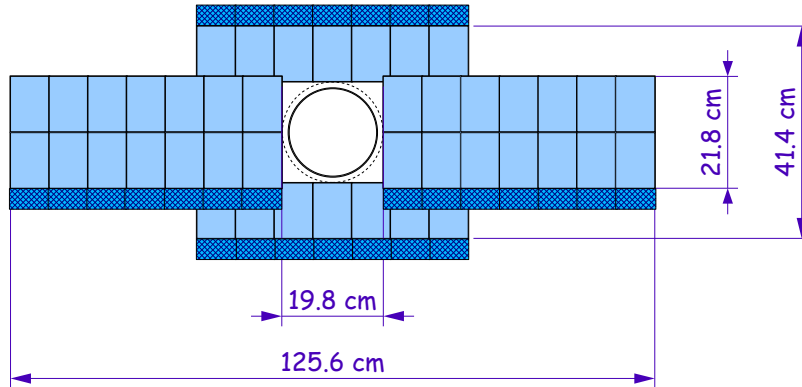
Figure 12: Geometry of an x-detection layer of the IT. Figure from [26].

The information from the individual sub-detectors can be used for track and vertex reconstruction. The single hits in the detectors are associated with different tracks which are fitted with a Kalman-Filter algorithm. This algorithm also accounts for multiple scattering effects. The quality of the fit is given by the reduced[3] χ^2.

Combining the track information with the known magnetic field, the momentum of the particles can be extracted. The momentum resolution is approximately $\delta p/p = 0.35\%$ for small momenta and $\delta p/p = 0.55\%$ for large momenta ($p \geqslant 120\,\text{GeV}$).

---

3 The reduced χ^2 is given by χ^2/ndof (number of degrees of freedom).
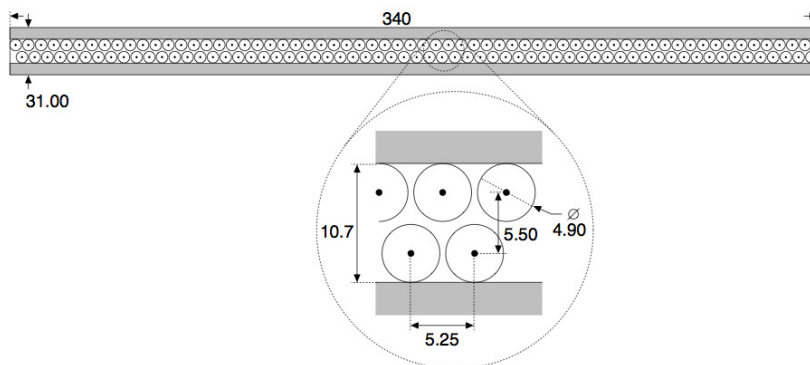
Figure 13: Cross section of a straw tube module. Figure from [26].

3.7 PARTICLE IDENTIFICATION

Aside from the momentum of the desired particle it is crucial to know the particle type. In the decay investigated in this thesis it is especially important to distinguish between pions and kaons. LHCb consists of several sub-detectors which are designed for particle identification. These include two ring-imaging Cherenkov detectors, calorimeter systems and muon chambers and are briefly explained as follows.

3.7.1 *RICH detectors*

The two ring-imaging Cherenkov detectors [30] (RICH1 and RICH2) exploit the Cherenkov effect to distinguish different charged particle species. This effect describes the behavior of highly energetic charged particles traversing material with a refractive index n. If the velocity v of these particles in the material is larger than the speed of light in the same medium, $c' = c/n$, electromagnetic radiation is emitted in the form of a cone under an angle Θ_C. This angle is related to the refractive index of the material and the particle's velocity as follows:

$$\cos(\Theta_C) = \frac{c'}{v} = \frac{1}{\beta n},$$

with $\beta = v/c$.

In the RICH detectors the light cones are projected onto a photo-detector via a mirroring system, containing spherical and planar mirrors, as illustrated in Figure 14. By measuring the radius of the projected light beams, the corresponding Cherenkov angle Θ_C can be determined. Combining this knowledge with the particle momentum from the tracking system, the mass m of the traversing particles can be inferred:

$$\cos(\Theta_C) = \frac{1}{n}\sqrt{1 + (m/P)^2}, \tag{2}$$

with $\beta = \frac{v}{c} = \frac{p}{E}$. In order to cover a large momentum range, the two RICH detectors contain different refractive materials and are positioned at different parts of the detector. RICH1, uses aerogel and C_4F_{10} gas, which is a good radiator for separating pions and kaons up to $60\,\text{GeV}$. It is located in the front part of the detector between the VELO and the Tracker Turicensis. This ensures that low-momentum particles covering a momentum range from $1\,\text{GeV}$- $60\,\text{GeV}$ to be measured before they are deflected strongly by the dipole magnet and leave the detector's acceptance. Plates of aerogel are directly placed behind the VELO exit window to identify particles with very low momenta. RICH2 is filled with gaseous CF_4 and is positioned behind the main tracking stations and covers momentum ranges up to $150\,\text{GeV}$.
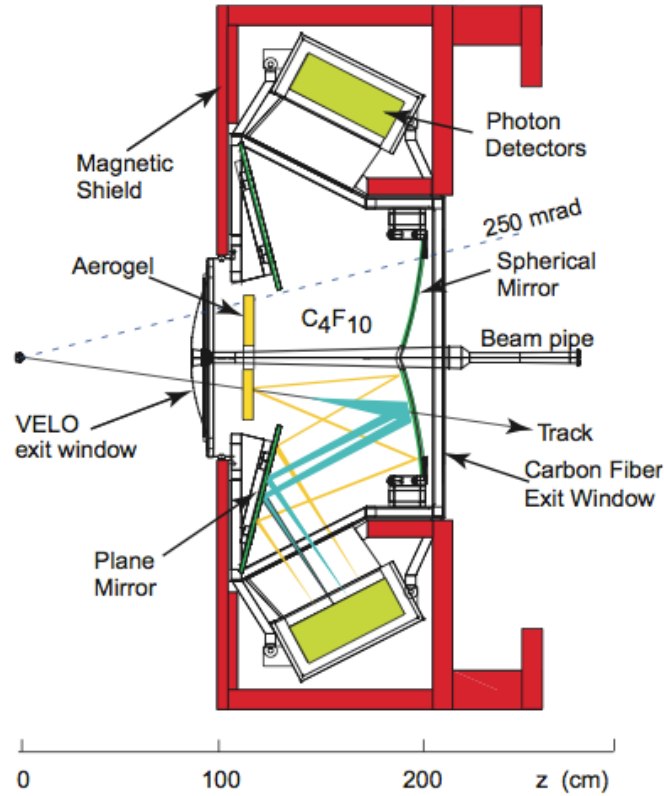
Figure 14: Left: schematic side view of the RICH detector, showing how the combination of a spherical and a plane mirror reflects the emitted Cherenkov light to the photo-detectors [31].

3.7.2 *Calorimeter System*

The calorimeter system fulfills several purposes. It is used to reconstruct photons, electrons and neutral particles, determine the total energy of all particles except muons and identify photons, electrons and hadrons depending on their signatures in each of the calorimeter components. This is done by measuring the energy of electromagnetic and hadronic showers. The calorimeter is the only detector which is sensitive to neutral particles. It consists of the following constituents: The Scintillator Pad Detector (SPD), the Preshower Detector (PS), the Electromagnetic Calorimeter (ECAL) and a Hadronic Calorimeter (HCAL). These individual parts of the calorimeter system have the following purpose and setup. The SPD and the PS allow for particle identification. They consist of rectangular shaped scintillator pads which are separated by a lead absorber with a thickness of 15 mm and a total radiation length of 2.5 X_0.

The SPD separates the signals of photons and electrons which is used for trigger purposes. This is done by the firing of a binary signal depending on the deposition energy in the cells of the SPD. Since there is only a small amount of photons that shower before the SPD, the misidentification probability is approximately 1%. The PS, built similarly, separates hadronic and electromagnetic showers due to their

different energy deposition in the detector.

With a width of 7.8 m and height of 6.3 m, the ECAL covers the full acceptance of the detector. It is located at 12.5 m downstream from the interaction point. It consists of alternating plates of lead and plastic scintillator plates with a thickness of 2 mm and 4 mm, respectively. The length of the ECAL amounts to 25 radiation lengths but only 1.1 hadronic interaction lengths. Thus the ECAL has a high sensitivity for electrons and photons, which create electromagnetic showers by bremsstrahlung and pair production. The energy resolution is

$$\frac{\sigma(E)}{E} = \frac{10\%}{\sqrt{E}} \oplus 1.5\%, \tag{3}$$

where E is the energy in GeV and $\oplus$ denotes the quadratic sum. The first term is related to statistical fluctuations and the second due to the readout. Both terms have to be summed quadratically.

Located behind the ECAL, the HCAL shows a similar setup as the ECAL, though the shower inducing material is different in order to trigger hadronic showers. The 4 mm wide scintillators are followed by iron absorbers with a thickness of 16 mm over a length of 1.2 m corresponding to 5.6 hadronic interaction lengths. The energy resolution is

$$\frac{\sigma(E)}{E} = \frac{80\%}{\sqrt{E}} \oplus 10\%, \tag{4}$$

where again E is the energy in GeV and $\oplus$ denotes the quadratic sum.

The main role of the calorimeters in terms of particle identification is to differentiate between photons, electrons, π^0 candidates and hadrons. Distinguishing charged from neutral particles is performed by studying the presence or absence of tracks in front of the energy deposits [5]. The photons are reconstructed from neutral clusters in the ECAL which are not associated with reconstructed tracks. Neutral pions dominantly decay into a pair of two photons [4]. They are reconstructed either from two photons in separated cells or from a single cluster in the ECAL. In the first case, called *resolved* π^0, photon candidates with transverse momenta larger than 200 MeV/c are paired and the corresponding invariant masses are compared to the nominal π^0 mass. For higher energies the separation of the two photons is on the order of a cell size of the ECAL, making it impossible to resolve them. A detailed explanation on the selection and classification of neutral pions is given in Section 5.4.

3.7.3   *The Muon System*

Muons have a large abundance in the final states of rare B- decays, making the muon detection vitally important. The muon system [32] acts as the final part of

---

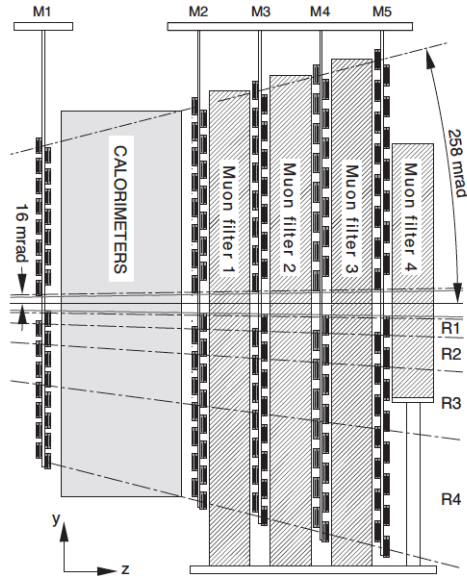4 $(98.823 \pm 0.034)\%$ of π^0 decay into two photons.

Figure 15: A schematic view of the muon system in the $y-z$ plane [32].

the LHCb detector. The entire system is divided into five muon stations M1-M5 which have a rectangular shape, as shown in Figure 15. They are placed along the beam axis. The first station is located in front of the calorimeters in order to optimize the determination of the transverse momenta for the trigger. The stations M2-M5, located behind the calorimeters, are separated by 80 cm thick iron plates so only muons can reach the last station. The first three muon stations have a very high spatial resolution in the bending plane in order to measure the direction of the track and the transverse momentum of the muon candidate. In the region of M1, which is close to the beam axis, Gas Electron Multipliers are used. The other chambers are composed of multi-wire proportional chambers which measure the trajectories of the muons by gaseous ionization detection. An additional iron absorber behind the station M5 assures that only muons coming from the proton-proton collision are detected. The minimum momentum of approximately 6 GeV is required for a muon to pass all five chambers.

The information of the RICH detectors, the calorimeters and the muon chambers is combined to form a particle hypothesis by using the likelihood ansatz[33]. With this ansatz, the maximized log-likelihood value $\ln \mathcal{L}$ can be obtained for different particle hypotheses $\ln \mathcal{L}(\pi, \mu, p, K)$. In this sense, a desired particle is selected by cutting on the ratio of likelihoods between different particle hypotheses, or equivalently on the difference of log-likelihood DLL. Since pions are the most common particles, the particle hypothesis usually is given in terms of $\mathcal{L}$. Concerning the discrimination of kaons and muons, this difference becomes:
$$\mathrm{DLL}(\mu - K) = \ln \mathcal{L}(\mu) - \ln \mathcal{L}(K) = \ln \frac{\mathcal{L}(\mu)}{\mathcal{L}(K)}.$$
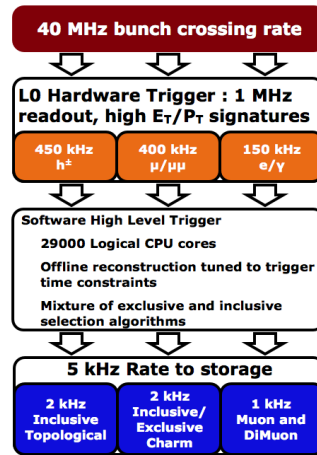
Figure 16: A scheme of the LHCb trigger system which reduces the initial bunch crossing rate of 40 MHz to a rate of approximately 5 kHz in three steps. [20].

3.7.4 *Data Selection - The trigger system*

For every pp - collision at the LHCb an enormous amount of data is produced. Computing time and storage limits the data which can be stored, thus a trigger is necessary which is used to select potentially interesting events while simultaneously rejecting as much background as possible. Potentially interesting events need to be selected by a trigger which reduces this rate to about 5 kHz. This is achieved by a dual-stage trigger system [34].

The Level-0 trigger (L0) forms the first stage of the trigger system. The selection of events in this step is called *online* selection. It is a hardware trigger which reduces the rate to approximately 1 MHz. This trigger selects the electron, hadron and photon clusters with the highest transverse energy and the two muons with the highest transverse momentum, since the B mesons have a relatively large mass. Events which are selected by the L0 trigger are further processed by the software based High Level Trigger (HLT). It is composed of two sub-triggers HLT1 and HLT2. The HLT1 trigger partially reconstructs events using information from the VELO and the tracking stations, determining primary vertices of the events and selecting events with displaced secondary vertices. The HLT1 operates at an output rate of approximately 50 kHz. Following the HLT1, the HLT2 performs a full reconstruction of the events which passed the HLT1, applying inclusive and exclusive lines to select desired events. Inclusive lines select events which originate in decays that have similar properties such as the *dimuon* line which searches for decays with two reconstructed muons in the final state such as B $\rightarrow$ J/ψ X with J/ψ $\rightarrow$ μ^+ μ^-. Topological lines cover B decays with a displaced vertex and two charged particles in the final state, being useful in detecting partially reconstructed decays where some of the final state particles are left undetected. Exclusive lines, on the other hand, reconstruct specific decay modes. The output rate at which the HLT1 stores the events is 5 kHz.

For the LHCb upgrade, the current procedure of reading out the detector at 1 MHz

after the Lo decision will be replaced by a 40 MHz readout, and the deployment of a very flexible software-based trigger running on a PC farm that will allow for significantly enhanced efficiencies, particularly for decays to hadronic final states [33].

Part 1

Determining the branching fraction of

$$B^+ \to K^{*+} \, \mu^+ \, \mu^-$$

using fully reconstructed events

ANALYSIS STRATEGY

In this thesis the relative branching fraction $\mathcal{B}$ of the rare $B^+ \to K^{*+} \mu^+ \mu^-$ decay with respect to the resonant decay channel $B^+ \to K^{*+} J/\psi$ is determined. In general, the branching fraction for a particular decay mode is the fraction of decays by this mode compared to the total number of decays. For the decay in focus, $B^+ \to K^{*+} \mu^+ \mu^-$, this can be expressed by[1]

$$\mathcal{B}(B^+ \to K^{*+} \mu\mu) = \frac{N(B^+ \to K^{*+} \mu\mu)}{2 \cdot \int \mathcal{L} dt \cdot \epsilon \cdot f_{B^+} \cdot \sigma_{b\bar{b}}}, \tag{5}$$

where N is the measured number of $B^+ \to K^{*+} \mu^+ \mu^-$ events obtained from a fit to data, and ϵ is the total efficiency of the signal selection. It is determined from simulation. $\int \mathcal{L} dt$ is the time-integrated luminosity which, multiplied with the production cross section $\sigma_{b\bar{b}}$, gives the total number of produced b and $\bar{b}$ quarks. The fraction f_{B^+} is the probability of a b quark to hadronize and form a B^+ meson. The factor 2 takes into account that the b quarks are produced in pairs. The variables are explained in more detail in the following chapter.

In order to determine the branching fraction precisely, the quantities of Equation 5 have to be measured explicitly. The luminosity, the hadronization probability, the efficiency and production cross section have large uncertainties. Taking the relative branching fraction of two decay modes consequently results in a lower total uncertainty as the uncertainties for these quantities cancel out since they are identical for both modes. For the decay in focus, the resonant $B^+ \to K^{*+} J/\psi$ decay is used as a reference channel. The J/ψ decay into a pair of muons is considered by taking the corresponding branching fraction $\mathcal{B}(J/\psi \to \mu\mu)$ into account. The value is taken from the Particle Data Group (PDG) [1]. The relative branching fraction of the non-resonant and the resonant B^+ decay thus results in:

$$\mathcal{R} = \frac{\mathcal{B}(B^+ \to K^{*+} \mu\mu)}{\mathcal{B}(B^+ \to K^{*+} J/\psi)} = \frac{N_{B^+ \to K^{*+} \mu\mu}}{N_{B^+ \to K^{*+} J/\psi}} \cdot \frac{\epsilon_{J/\psi}}{\epsilon_{\mu\mu}} \cdot \mathcal{B}(J/\psi \to \mu\mu). \tag{6}$$

The steps in determining the branching fraction are implemented as follows:

- First, the event yields for the resonant and non-resonant mode, $N_{\mu\mu}$ and $N_{J/\psi}$ have to be determined. The first step in determining the event yields is the signal selection of $B^+ \to K^{*+} J/\psi$ and $B^+ \to K^{*+} \mu^+ \mu^-$ decays. This is performed in Chapter 5. After the data sample used in this analysis has passed trigger requirements and an offline selection, it is subject to a multivariate analysis which further reduces combinatorial background. The non-

---

1 For simplicity reasons in the formulae, the dimuon pair is denoted by $\mu\mu$ instead of $\mu^+\mu^-$.

resonant signal candidates are selected by applying vetoes on the charmonium resonances J/ψ and ψ(2S).

- After having selected the B^+ signal candidates in the resonant and non-resonant decay, their mass spectrum is fitted with a model describing signal and background components, which is explained in . From this, the corresponding signal yields can be extracted. Additionally, the statistical significance of the measurement in the non-resonant channel is determined.

- Further, the ratio of efficiencies $\frac{\epsilon_{J/\psi}}{\epsilon_{\mu\mu}}$ is deduced from a simulated data sample.
  With the knowledge of the branching fraction for the resonant channel $B^+ \rightarrow K^{*+} J/\psi$, the absolute branching fraction can be determined as well.

- A quantitative study of systematic uncertainties cannot be accomplished in the scope of this thesis. Compared to the contribution from statistical uncertainties, one does not expect a significant impact of systematic uncertainties on the measurement. Nevertheless, a qualitative summary of systematics is given at the end of .

SELECTING FULLY RECONSTRUCTED DECAYS

This chapter covers the signal selection of rare $B^+ \to K^{*+} (\to K^+ \pi^0) \mu^+ \mu^-$ decays, as well as the signal selection of the reference channel decay $B^+ \to K^{*+} J/\psi$. The focus lies on decay-specific selection procedures, describing the steps from the raw data produced in each collision until the creation of the final data sample. The purpose of the trigger is designed to select only potentially interesting events which are used for physics analyses (Section 5.1). After passing the trigger requirements, the data is processed by a tighter offline selection procedure to extract signal events more (Section 5.2). Finally, a multivariate analysis is performed to effectively separate signal and combinatorial background (Section 5.7).

5.1 ONLINE RECONSTRUCTION AND SELECTION

The selection of $B^+ \to K^{*+} \mu^+ \mu^-$ decays starts with the online selection which is comprised of three trigger stages. The decay has to fire one of several trigger lines in each stage. The first trigger stage is the L0 hardware trigger. This stage requires one single muon from one of the muons in the $B^+ \to K^{*+} \mu^+ \mu^-$ decay. In the next stage, HLT1, the event has to be triggered by the single track trigger or single muon trigger. In HLT2, which is the last step in the online reconstruction, several trigger lines are used. These are either topological triggers or muon triggers. As the offline selection criteria are always tighter than the requirements from the trigger stages, the latter are not explained in detail. A detailed description of the trigger decision exceeds this the scope of this thesis, though can be found in [35].

5.2 OFFLINE RECONSTRUCTION AND SELECTION

The data which has passed the trigger requirements is further processed by a more powerful offline reconstruction, called *stripping*. Different decay specific selection criteria are adapted to the $B^+ \to K^{*+} J/\psi$ decay, with the goal to reject more background and reduce the computing time for further analysis. In addition, also particle identification requirements which are not available in the trigger, are applied, too.

FLIGHT DISTANCE, DIRECTION ANGLE, IMPACT PARAMETER Discriminating variables are the flight distance (FD), the direction angle (DIRA) and the impact parameter (IP):

The Impact Parameter is the distance of closest approach of a track to the primary vertex. Generally, It is used to identify long lived particles such as

the B^+ and reject short lived background which will emanate in the primary vertex. A cut on high IP values of tracks corresponding to the particles K^{*+}, $K\,\mu^+$ and μ^-, ensures that they stem from a displaced vertex. It is depicted schematically in Figure 17a.

The flight distance is the distance the B meson travels from the primary vertex to the secondary vertex (SV). For daughter particles, such as the K^{*+} or the J/ψ this is the flight distance with respect to the primary vertex.

DIRA is the angle between the flight direction of the particle and its reconstructed momenta. As these directions should be the same this angle is required to be small. Since the cosine of this angle is used in the selection, a small DIRA results in a large value for the cosine. The DIRA and FD are depicted in Figure 17b. Accordingly the χ^2 values for these variables can be defined by χ^2_{FD} and χ^2_{IP}.

KINEMATIC VARIABLES Additionally, kinematic variables can be used for the separation of signal and combinatorial background, most importantly the transverse momentum (p_{T}) of the daughter particles[1]. The decay products of the B^+ meson generally have large momenta in the direction transverse to the beam. With a cut on the transverse momenta, combinatorial background can be reduced.

PARTICLE IDENTIFICATION In the chapter on the LHCb detector particle identification is discussed. The DLL variable expresses the quality of the particle/-mass hypothesis and is also used in the selection.

TRACK AND VERTEX QUALITY Furthermore, Track χ^2 and Vertex χ^2 variables are used which quantify the quality of track and vertex fits. In both cases, also the χ^2 value normalized to the number of degrees of freedom, nDOF (χ^2/nDOF) can be used. The Vertex χ^2 value can indicate whether all daughter particles stem from the same vertex, which is required to be the B^+ secondary vertex in the $B^+ \rightarrow K^{*+}\,\mu^+\,\mu^-$ decay.

GHOST PROBABILITY A random association of hits which is not caused by the passage of a real particle in the detector, is referred to as a *ghost* track. A cut on the ghost probability of a track can be applied to reject ghost particles.

HIT MULTIPLICITY IN THE SPD The hit multiplicity of Scintillating Pad Detector (SPD) hits gives a measure for the activity of an event. Events with a too

---

1 According to the definition of the detector's coordinate system, the transverse momentum lies in the x-y-plane.
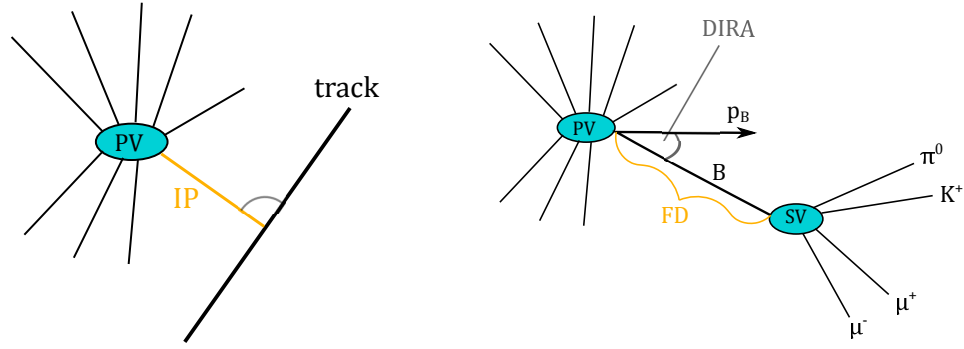
(a) The impact parameter (IP) is the shortest distance between the primary vertex (PV) and the track.

(b) Direction angle (DIRA) and flight distance (FD) of the B meson.

Figure 17: Definition of the impact parameter, the direction angle and the flight distance.

large multiplicity are rejected because of the combinatorial background [36].

Additionally, the mass of K^{*+} candidates is restricted to a certain mass window. The entire mass window is twice the value given in the table. Table 1 shows the summary of selection cuts for the B$^+$ → K^{*+} μ$^+$ μ$^-$ decay used in the stripping line *StrippingB2XMuMu*[2]. This stripping selection is used for nearly all electroweak penguin analyses.

5.3 RECONSTRUCTING B$^+$ MESONS

In the decays in focus, B$^+$ → K^{*+} (→ K$^+$ π^0) μ$^+$ μ$^-$ and B$^+$ → K^{*+} (→ K$^+$ π^0) J/ψ (→ μ$^+$ μ$^-$), the four momentum of every daughter particle, K$^+$, π^0, μ$^+$ and μ$^-$, is known. The π^0 is reconstructed as a resolved π^0. This is explained in the next section. The four momenta of particles which are reconstructed via their daughter particles, such as the K^{*+} meson, as well as the J/ψ meson in the reference channel, are determined by adding the daughter particles' four momenta. For the K^{*+} this yields:

$$p_{K^{*+}} = p_{K^+} + p_{\pi^0}.$$

The corresponding mass of the K^{*+} meson then results in:

$$m_{K^{*+}}^2 = p_{K^{*+}}^2 = (p_{K^+} + p_{\pi^0})^2.$$

This results in a mass distribution in contrast to the constant mass of the daughter particles. The simulated mass spectra of the π^0 and the K^{*+} can be seen in Figure 19a and Figure 19b, respectively. Both mass windows are restricted according to the offline selection in Table 1. The K^{*+} has a natural width of

---

2 From the *Stripping20* sample.

Description	Cut
B- Mass Minimum	$> 4800\,\text{MeV}/c^2$
B- Mass Maximum	$> 7100\,\text{MeV}/c^2$
B Vertexχ^2	< 8
B χ^2_{IP}	< 16
B DIRA	> 0.9999
B $\chi^2_{\text{FD}}{}^3$	> 121.0
π^0 p_T	$> 800\,\text{MeV}/c^2$
π^0 Mass Window	$30\,\text{MeV}/c^2$
Daughter Particle Vertexχ^2	< 12.0
Daughter Particle DIRA	< -0.9
Dimuon χ^2_{FD}	> 9.0
Muon χ^2_{IP}	> 9.0
Muon PID	> -3.0
K^{*+} χ^2_{FD}	> 9.0
K^{*+} Daughter Particles's χ^2_{IP}	> 9.0
K^{*+} Mass Window	$300\,\text{MeV}/c^2$
SPD Track Multiplicity	< 600
Track$\frac{\chi^2}{n\text{DOF}}$	< 5.0
Ghost Probability of Track	< 0.4

Table 1: Selection cuts for $B^+ \rightarrow K^{*+}\,\mu^+\,\mu^-$ in the *StrippingB2XMuMu* Stripping line.

$\Gamma_{K^{*+}} = (50.8 \pm 0.9)\,\text{MeV}/c^2$ [1]. Therefore the width of its invariant mass distribution should be dominated by the natural width and not by the momentum resolution of the detector. In this manner, the K^{*+} mass can be further restricted to $m(K^{*+}) \in [742, 1041]\,\text{MeV}/c^2$, which corresponds to a standard deviation of approximately 3σ from the nominal K^{*+} mass of $m(K^{*+}) = (891.7 \pm 0.3)\,\text{MeV}/c^2$. Small bremsstrahlung effects which are caused by the low pion mass, are neglected. Analog to the K^{*+}, also the J/ψ is reconstructed by adding the four momenta of the two muons. In the following, the dimuon spectrum refers to the invariant mass distribution $m^2(\mu\mu) = (p_{\mu^+} + p_{\mu^-})^2$. The dimuon mass spectrum is discussed and shown in Section 5.6.

The B^+ mass spectrum finally is calculated by forming the sum of all four daughter particles' four momenta:

$$m^2(B^+) = (p_{K^+} + p_{\pi^0} + p_{\mu^+} + p_{\mu^-})^2.$$

The invariant mass distribution from a simulated signal sample is shown in Figure 18a. The corresponding distribution from data is depicted in Figure 18b. The spectrum is clearly dominated by background and therefore no B^+ peak is visible in the spectrum. The corresponding π^0 and K^{*+} invariant mass distributions from measured data are not presented at this point, as they are highly dominated by backgrounds as well and there is no visible peak. This background as well as a
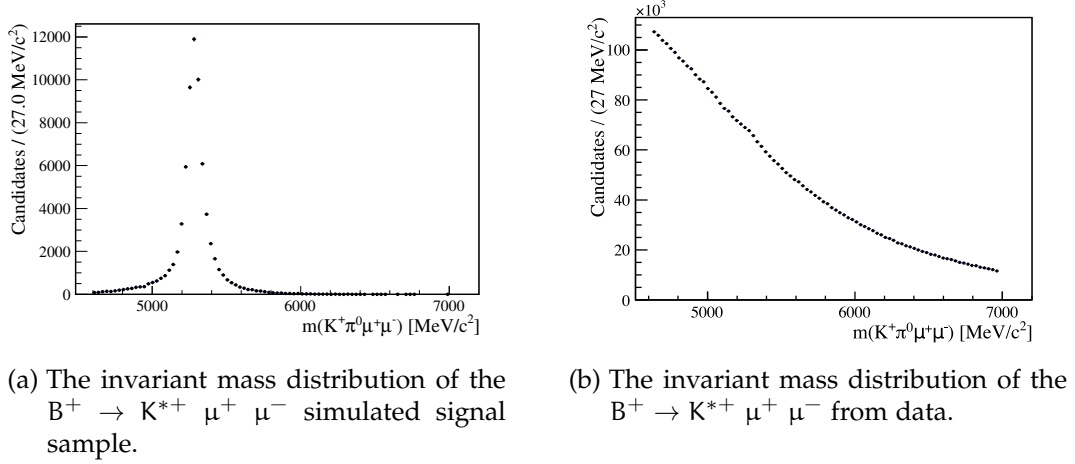
(a) The invariant mass distribution of the $B^+ \to K^{*+} \mu^+ \mu^-$ simulated signal sample.

(b) The invariant mass distribution of the $B^+ \to K^{*+} \mu^+ \mu^-$ from data.

Figure 18: Invariant B^+ mass distributions for simulation and data.

(a) The resolved π^0 mass distribution from a simulated signal sample.

(b) The K^{*+} mass distribution from a simulated signal sample.
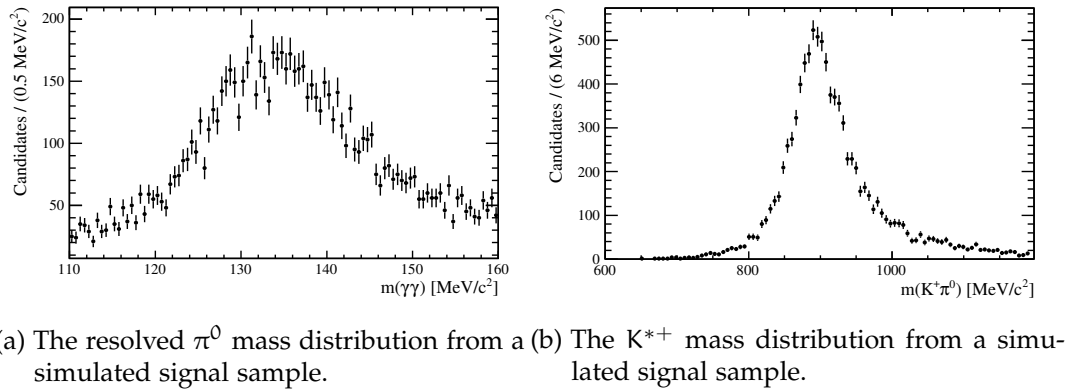
Figure 19

multivariate method to eliminate it is discussed in Section 5.5 and Section 5.7. In Chapter 6 the π^0 and K^{*+} mass distributions from measured data are finally depicted after background has been suppressed.

5.4 RESOLVED AND MERGED PIONS

As pointed out in Chapter 5, the π^0 decays into a pair of photons, which are detected by the ECAL. The invariant mass of a resolved π^0 can be written as:

$$m^2 = 2E_1 E_2 (1 - \cos \alpha)$$

where E_1 and E_2 are the photon energies and α is the opening angle between the photons.

For high photon energies, the photons are merged into one cluster such that E_1, E_2 and α cannot be extracted in the above way. It is still possible to estimate the invariant mass of the π^0 system based on the shape of the merged cluster. Two cells which have the highest energy deposit are identified and several virtual sub-

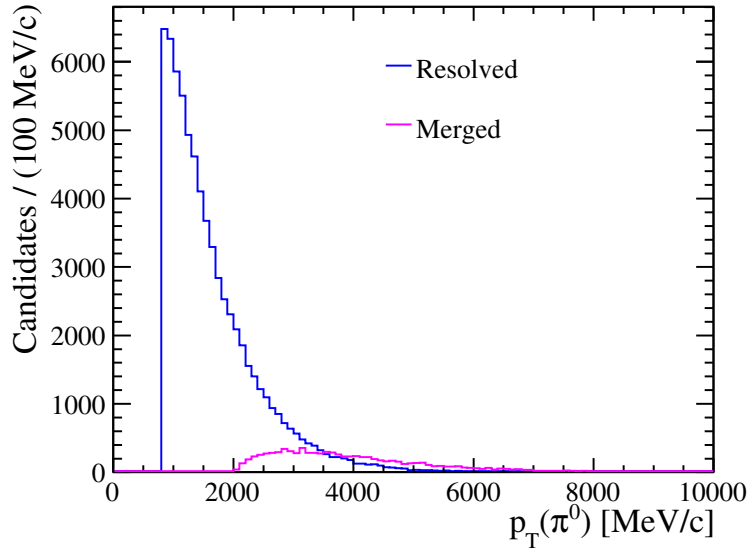Figure 20: The distribution of transverse momenta for resolved (blue) and merged (magenta) π^0 candidates. Only 4.4% of the π^0 from the $B^+ \to K^{*+} \mu^+ \mu^-$ decay are reconstructed as merged candidates.

clusters are built around each of them. The energy of the entire cell, which is the sum of the photon energies, is shared among the virtual subclusters based on the transversal shape of the photon showers. The shape of the photon showers is obtained from a sample of isolated photons. Each of the cluster is then reconstructed as a single photon hypothesis cluster and an energy of each of the clusters can be determined. The opening angle can be determined from the distribution of the cluster. This algorithm is explained in [37].

To avoid misidentification of high-energetic single photons with merged π^0, an multivariate method can be applied. It is based on the different cluster shapes of these two particles in the ECAL and PS (preshower detector). A merged π^0 will create a broad cluster shape compared to that of a single photon [5] and therefore can be distinguished. Detailed information on this method can be found in [38].

The transverse momentum distributions from simulation for resolved and merged π^0 from the decay $B^+ \to K^{*+} \mu^+ \mu^-$ can be seen in Figure 20. The resolved category clearly dominates the spectrum. At high energies around 4000 MeV/c the contribution of the merged category exceeds the contribution from resolved π^0. As the fraction of merged π^0 compared to the total number of π^0 in this decay is approximately 4.4%, only resolved π^0 are selected for the analysis. The cut on the momenta at 800 MeV/c comes from the Stripping Selection.

5.5   EXPECTED BACKGROUND SOURCES

To isolate the very rare signal while maintaining a high signal yield, it is important to understand which backgrounds can mimic the typical signature of the $B^+ \to$

$K^{*+} \mu^+ \mu^-$. As the number of resonant $B^+ \to K^{*+} J/\psi$ decays is required to determine the relative branching fraction, it is also crucial to examine background contributions in this charmonium decay mode. The background contributions can consist of physical background, where similar decays are (partially) reconstructed and taken as the signal decay, or a background component, where one or more of the final state particles are randomly combined to form a signal-like signature.

PEAKING BACKGROUNDS They consist of B decays, where one or more particles are misidentified and therefore mimic the signal decay. These decays peak in a similar mass region as the B^+ invariant mass. In the reconstruction of the resonant signal decay $B^+ \to K^{*+} J/\psi$, a charged pion can be misidentified as a K^+. The π^0 and the π^+ are daughter particles of the resonance ρ^+ meson. When this resonance is combined with the J/ψ. The sum of the four momenta of ρ^+ and J/ψ form the B^0 meson. The branching ratio of the decay $B^0 \to \rho^+ J/\psi$ is $\mathcal{B} = (5.0 \pm 0.8) \times 10^{-5}$ [1], which is two orders of magnitude smaller than the resonant $B^+ \to K^{*+} J/\psi$ decay. The ρ meson has a mass of $(775.4 \pm 0.4)\,\mathrm{MeV}/c^2$ while the K^{*+} has a mass of $(891.66 \pm 0.26)\,\mathrm{MeV}/c^2$. By limiting the reconstructed invariant mass $m(K^+ \pi^0)$ to a tighter window around the nominal K^{*+} mass, the background from $B^0 \to \rho^+ J/\psi$ decays can be eliminated (see Chapter 6).

PARTIALLY RECONSTRUCTED BACKGROUNDS These backgrounds arise when one of the daughter particles is not reconstructed. This will lead to a lower total invariant mass since one particle is missing. Therefore, partially reconstructed backgrounds will peak in the lower part of the $m(K^+ \pi^0 J/\psi)$ invariant mass distribution.

COMBINATORIAL BACKGROUND When all four final state particles are chosen randomly this results in combinatorial background. This type of background, in contrast to the peaking background, decreases exponentially as a function of $m(K^+ \pi^0 J/\psi)$. A large source of combinatorial background in the reconstruction of the π^0 is created by random photons which originate in the primary vertex. Their energy depositions in the electromagnetic calorimeter are wrongly combined to a π^0. Since this type of background features different kinematic properties a statistical separation from the signal is possible which is performed by a multivariate analysis as demonstrated in Section 5.7.

5.6 CHARMONIUM VETOES

In this analysis, the branching fraction of the decay $B^+ \to K^{*+} \mu^+ \mu^-$ with two non-resonant muons is determined. The expected branching ratio is significantly smaller than the reference decay channel $B^+ \to K^{*+} J/\psi$. Consequently it is crucial to eliminate all dimuon resonances in the transition to the non-resonant channel.

The resonant decays $B^+ \to K^{*+} J/\psi\,(1S)$ and $B^+ \to K^{*+}\,\psi(2S)$ significantly add to the overall yield in the spectrum $K^+\,\pi^0\,\mu^+\,\mu^-$. The two resonances can be seen in the invariant dimuon mass distribution obtained from data in Figure **??**. The chosen markers to demonstrate the data points are larger than the corresponding error bars. The branching fractions are:

$$B^+ \to K^{*+} J/\psi\,(1S): \qquad \mathcal{B} = (1.44 \pm 0.08) \times 10^{-3}$$
$$B^+ \to K^{*+}\psi(2S): \qquad \mathcal{B} = (6.7 \pm 1.4) \times 10^{-4}$$

Approximately 6% of the J/ψ mesons decay into two muons. Therefore the resonant $B^+ \to K^{*+} J/\psi\,(1S)\,(\to \mu^+\,\mu^-)$ decay results in a branching ratio which is approximately a factor of 80 larger than expected the nonresonant decay, $\mathcal{B}(B^+ \to K^{*+}\mu^+\mu^-) = (1.12 \pm 0.15) \times 10^{-6}$ [1]. As these resonant decays cannot be disentangled from the non-resonant components of the B^+ decay, they are removed by vetoes in the dimuon spectrum. A veto is applied to the dimuon mass in the region from $2967\,\mathrm{MeV}/c^2$ to $3176\,\mathrm{MeV}/c^2$ to remove the J/ψ and from $3568\,\mathrm{MeV}/c^2$ to $3766\,\mathrm{MeV}/c^2$ to remove the $\psi(2S)$ resonance respectively. These mass windows correspond to a 5σ significance which was determined by fitting the distributions. Because of the large abundance of the resonant decays, even a even a contribution of 1% would distort the signal yield of the non-resonant decay. Therefore it is crucial to make sure that the J/ψ and $\psi(2S)$ resonances are sufficiently removed from the dimuon spectrum. As the J/ψ and $\psi(2S)$ decay undergo final state radiation, the vetoes must be extended to exclude these radiative tails as well. The final veto cuts are shown in Table 2.

Resonance	Mass veto
J/ψ	$m(\mu\mu) \notin [2796, 3225]\,\mathrm{MeV}/c^2$
$\psi(2S)$	$m(\mu\mu) \notin [3540, 3800]\,\mathrm{MeV}/c^2$

Table 2: J/ψ and $\psi(2S)$ mass vetoes.

5.7   MULTIVARIATE SELECTION

After having applied several selection cuts in the trigger and the stripping selection, $B^+ \to K^{*+}\,\mu^+\,\mu^-$ signal events can further be separated from background by applying a multivariate analysis.

The technique to separate the rare decay from background which is used in this analysis, is the *Boosted Decision Tree* (BDT) [39] from the *Toolkit for Multivariate Analysis* (TMVA) [40]. A decision tree is a binary classifier which evaluates multiple variables with yes/no decisions considering the separation of background from signal events. It returns a single response combining all input variables in an efficient way. The separation power of the decision tree depends on statistical
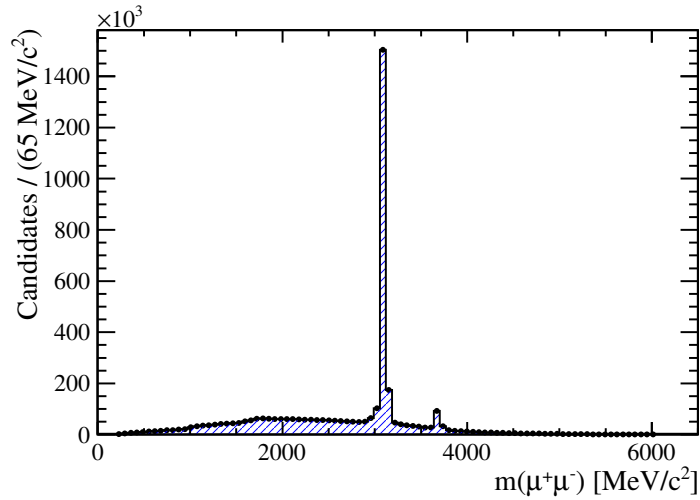
Figure 21: Histogram of invariant dimuon mass distribution from data showing the two resonances J/ψ and ψ(2S) which clearly dominate the spectrum. Data points are shown as well.

fluctuations in the background and signal samples. The robustness of the BDT toward these statistical fluctuations can be increased by applying a method called boosting. The most popular boosting algorithm is the so-called AdaBoost (adaptive boost) [41]. AdaBoost iteratively re-weights events which were misclassified by previous classifiers in the following manner. The binary classification is extended from one tree to several trees. Events that were misclassified during the training of a decision tree, i.e. a background event was assigned as a signal event or vice versa, are given a higher event weight in the training of the subsequent tree. Starting with the original event weights when training the first decision tree, the following tree is trained using a modified event sample where the weights of previously misclassified events are multiplied by a common boost weight [40]. The outcome is then combined to a single classifier with a weighted average of the individual decision trees.

5.7.1 *BDT Training and Testing*

The BDT is trained with the sideband region of a data sample from 2011 and 2012 data corresponding to $3\,\text{fb}^{-1}$, serving as a background template, and a simulation describing the signal decay. The invariant mass distribution of the simulated $B^+ \rightarrow K^{*+} \mu^+ \mu^-$ signal candidates as well as the mass distribution obtained from data has been previously shown in Figure 18. As pointed out before, the main background source is combinatorial background. This background dominates the measured $m(K^+ \pi^0 \mu^+ \mu^-)$ spectrum and therefore no B^+ peak is visible in the spectrum. Consequently a background template is needed which only includes combinatorial background. A clean region for this template is $m(K^+ \pi^0 \mu^+ \mu^-) > 5700\,\text{MeV/c}^2$ since combinatorics are expected to be the major contribution to the

total background in this region. The measure of statistical separating the distribution of the variable y for background and signal is given by the separation δ of the corresponding variable. It is defined by the integral

$$\delta = \frac{1}{2} \int \frac{(\mathcal{P}_{sig}(y) - \mathcal{P}_{bkg}(y))^2}{\mathcal{P}_{sig}(y) + \mathcal{P}_{bkg}(y)} dy$$

with the signal ($\mathcal{P}_{sig}(y)$) and background ($\mathcal{P}_{bkg}(y)$) PDF for the variable y [42]. For the training of the BDT variables are chosen to optimally separate signal and background .

A list of the variables used here is given in Table 3. The corresponding separations δ are also shown for the individual variables. Several variables have been previously explained in Section 5.2. Additionally the photon confidence level helps to increase the separation between electrons and photons. For the variables which are created in pairs, such as the two muons or the two photons, simple combinations such as the difference, minimum or maximum of the two original variables can reduce combinatorial background from the combination of a particle of the true decay with an random random particle.

Variable	Particle	Separation
p_T	B^+	$\delta = 34.7\%$
p_T	K^+	$\delta = 59.6\%$
p_T	K^{*+}	$\delta = 64.1\%$
p_T	π^0 Resolved	$\delta = 37.6\%$
p_T	γ_1	$\delta = 15.5\%$
p_T	γ_2	$\delta = 15.5\%$
FD	B^+	$\delta = 13.1\%$
χ^2_{FD}	B^+	$\delta = 34.7\%$
DIRA	B^+	$\delta = 33.8\%$
$\chi^2_{Endvertex}$	B^+	$\delta = 48.5\%$
χ^2_{IP}	B^+	$\delta = 11.8\%$
χ^2_{IP}	K^+	$\delta = 22.8\%$
CL	γ_1	$\delta = 16.1\%$
CL	γ_2	$\delta = 17.3\%$
max(CL)	γ_1 and γ_2	$\delta = 17.5\%$
min(CL)	γ_1 and γ_2	$\delta = 24.4\%$
max(p_T)	γ_1 and γ_2	$\delta = 31.8\%$
difference of χ^2_{IP}	μ^+ and μ^-	$\delta = 16.1\%$
min(χ^2_{IP})	μ^+ and μ^-	$\delta = 36.8\%$

Table 3: Variables used in the BDT and their separation. The distributions of the remaining variables used in the training and testing can be found in Appendix A

The obtained BDT response distribution for the background and signal sample, respectively, is shown in Figure 23b. Large discrepancies between the training and
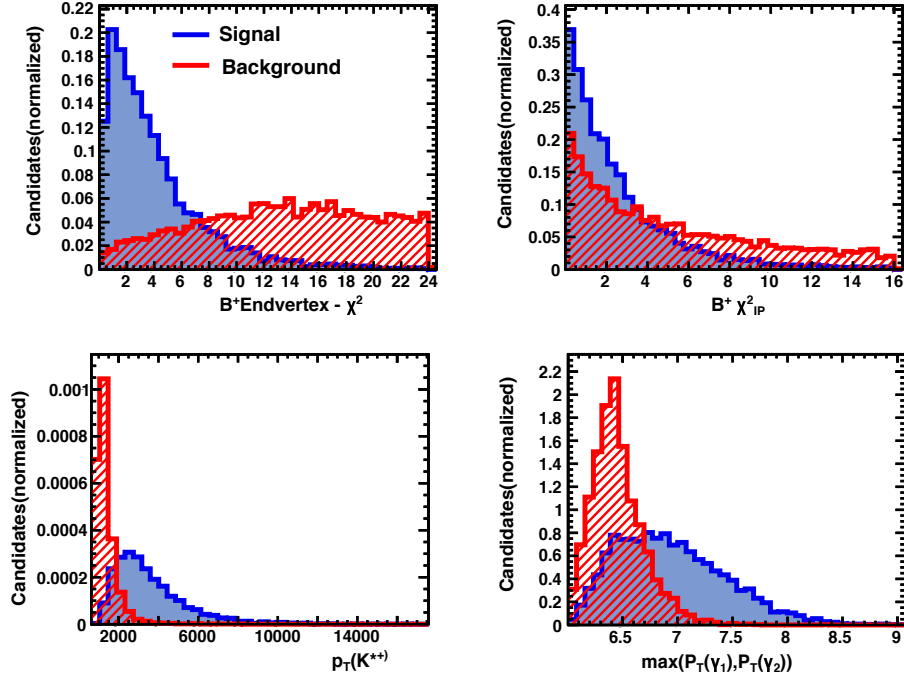
Figure 22: Distribution of signal (red) and background (blue) events for selected variables used in the BDT training.

testing samples occur when the BDT is trained on statistical fluctuations, which is called overtraining. The good agreement of the BDT response of the training and testing sample shows that this is not the case here. Figure 23a shows the dependency of the BDT response and the B^+ mass across the upper sideband. The average BDT response value, depicted by the black line, is independent of the invariant $m(K^+\pi^0\mu^+\mu^-)$ mass. Therefore no artificially peaking structures, which may fake the signal, are created by the BDT selection.

After the boosted decision tree has been trained, the available data can further be classified with the information obtained by the multivariate analysis. A cut on the BDT response will suppress combinatorial background. The BDT cut is optimized by finding the maximum of the figure of merit $S/\sqrt{S+B}$, where S and B are the simulated signal and background events from data, respectively. For each BDT cut, the signal yield is obtained by fitting the resonant $B^+ \to K^{*+} J/\psi$ events in simulation. Since the upper sideband is used in the background template, the background yield $nBkg_{\mu\mu}$ in the signal region is obtained by extrapolating the yield into the signal region.

With these parameters, the figure of merit becomes $nSig_{\mu\mu}/\sqrt{nSig_{\mu\mu}+nBkg_{\mu\mu}}$. The optimal BDT response cut is found to be: BDT response > 0.397.
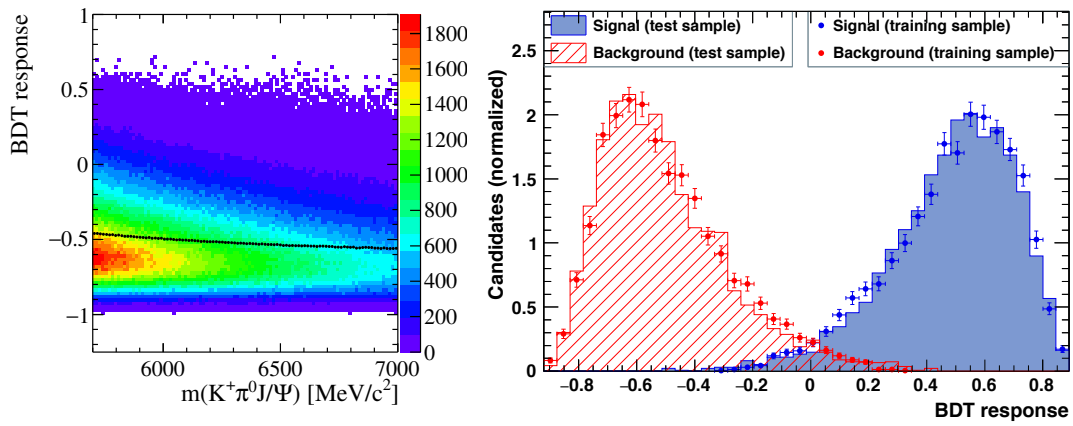
(a) Two-dimensional plot of mass and BDT response to test the effect of BDT cut on the sideband mass region $(m(K^+\pi^0 J/\psi) > 5700\,\text{MeV}/c^2)$.

(b) The BDT response distribution for the signal (blue) and background (red) template.

DETERMINING THE BRANCHING FRACTION

This chapter covers the calculation of the branching fraction of the rare $B^+ \to K^{*+} \mu^+ \mu^-$ decay relative to the resonant $B^+ \to K^{*+} J/\psi$ decay. First, the formula which is used to determine the branching fraction which has previously been defined in Chapter 4 is explained in detail. Further, fits to the reconstructed B^+ mass to determine the number of selected $B^+ \to K^{*+} \mu^+ \mu^-$ and $B^+ \to K^{*+} J/\psi$ events in simulated and measured data samples are performed. The statistical significance is also discussed. As this part mainly gives a motivation of Part 2 there is no discussion of systematic uncertainties.

6.1 PROCEDURE

The branching ratio of the rare $B^+ \to K^{*+} \mu^+ \mu^-$ decay relative to the resonant $B^+ \to K^{*+} J/\psi$ decay is calculated according to:

$$\mathcal{R} = \frac{\mathcal{B}(B^+ \to K^{*+}\mu\mu)}{\mathcal{B}(B^+ \to K^{*+}J/\psi)} = \frac{N_{B^+ \to K^{*+}\mu\mu}}{N_{B^+ \to K^{*+}J/\psi}} \cdot \epsilon_R \cdot \mathcal{B}(J/\psi \to \mu\mu),$$

where $N(X \to Y)$ is the measured number of $X \to Y$ decays. ϵ_R is the relative efficiency of the signal selection. The total efficiency ϵ which is used in the determination of the absolute branching fraction as in Equation 5 takes into account that in several stages of the $B^+ \to K^{*+} \mu^+ \mu^-$ reconstruction events are lost and therefore do not appear in the final data sample from which N is determined. An efficiency can be assigned to each effect which causes an events loss. The total efficiency ϵ then is the product of all contributing efficiencies:

$$\epsilon = \epsilon_{acc} \cdot \epsilon_{tr} \cdot \epsilon_{sel} \cdot \epsilon_{rec}.$$

ϵ_{acc} takes into account that only a fraction of the decays lies within the acceptance of the detector. ϵ_{tr} is the fraction of events that have passed the trigger requirements and ϵ_{sel} the ones which have then passed the selection cuts, such as the stripping and multivariate analysis cuts. The efficiency to finally find the required daughter particles K^+, π^0, μ^+ and μ^-, and combine their four momenta to a B^+ is given by ϵ_{rec}. When the relative branching fraction is determined, the fraction of these efficiencies in the resonant and non-resonant channel are used. Within uncertainties, which are considered to be small compared to the statistical uncertainties in determinining $N(X \to Y)$, the efficiencies ϵ_{acc}, ϵ_{tr} and ϵ_{sel} are expected to be equal in $B^+ \to K^{*+} J/\psi$ and $B^+ \to K^{*+} \mu^+ \mu^-$. Therefore, they
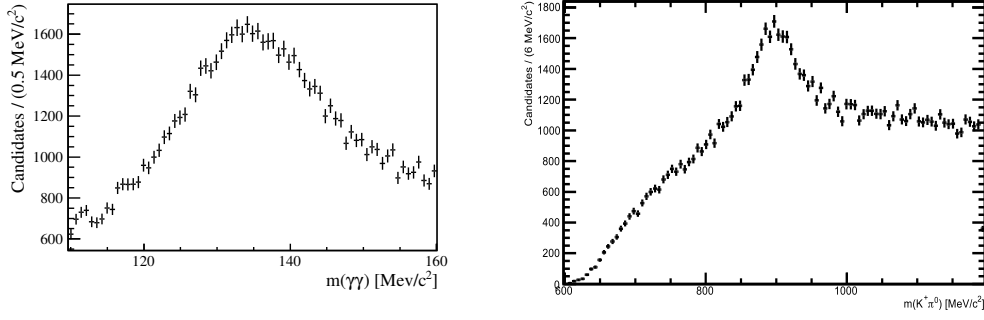
Figure 24: π^0 (left) and K^{*+} (right) invariant mass distributions from data after the application of a BDT response cut.

cancel out when calculating the relative branching fraction. The relative efficiency ϵ_R can consequently be expressed as follows:

$$\epsilon_R = \frac{\epsilon_{J/\psi}}{\epsilon_{\mu\mu}}$$

with

$$\epsilon_{J/\psi} = \frac{N_{MC}(B^+ \to K^{*+} J/\psi}{N_{MC,gen}(B^+ \to K^{*+} J/\psi)}$$

and

$$\epsilon_{\mu\mu} = \frac{N_{MC}(B^+ \to K^{*+} \mu\mu}{N_{MC,gen}(B^+ \to K^{*+} \mu\mu)}.$$

$N_{MC,gen}(X \to Y)$ represents the number of generated events for the decay $X \to Y$ and $N_{MC}(X \to Y)$ the number of events after passing the preselection and BDT cuts respectively.

The number of generated events in the simulated resonant and non-resonant data samples are:

$$N_{MC,gen}(B^+ \to K^{*+} J/\psi) = 1025796$$
$$N_{MC,gen}(B^+ \to K^{*+} \mu\mu) = 1073086.$$

In the next step, the number of reconstructed signal events in simulated and measured data is determined. In addition to the limitations on the K^{*+} mass, all charmonium resonances are eliminated in the non-resonant channel as previously explained in Section 5.6. For the resonant channel the J/ψ mass is restricted to the region from $2900\,\mathrm{MeV/c^2}$ to $3150\,\mathrm{MeV/c^2}$. The events from the simulated data sample are required to pass the same selection cuts as the real collision data.

6.2 FIT MODEL

This section describes the fit models used in the fit of simulated and measured data.

As bremsstrahlung is produced by the two muons in the decay of the B^+ meson, a model to describe the signal shape is required which accounts for these loss processes. A Crystal Ball function fulfills this property, as it is an asymmetric probability density function (p.d.f) consisting of a Gaussian core and a power-law low-end tail which adds to the Gaussian below a certain threshold. It is named after the Crystal Ball detector at the Stanford Linear Accelerator Center (SLAC) [43]. The Crystal Ball (CB) function has four parameters and is defined by:

$$
\mathcal{P}_{CB}(\alpha, n, \sigma, \mu; m) = \frac{1}{N} \cdot \begin{cases} e^{-\frac{(m-\mu)^2}{2\sigma^2}} & \text{for } \frac{m-\mu}{\sigma} > -\alpha \\ A \cdot (B - \frac{m-\mu}{\sigma})^{-n} & \text{for } \frac{m-\mu}{\sigma} \leqslant -\alpha \end{cases}
$$

The quantities A and B are

$$
A = \left(\frac{n}{|\alpha|}\right)^n \cdot e^{-\frac{|\alpha|^2}{2}}
$$

and

$$
B = \frac{n}{|\alpha|} - |\alpha|.
$$

The parameter μ gives the position of the peak and σ describes the width of the Gaussian part. The parameter α describes the transition to the power-law tails of the distributions, while n describes the form of these tail. In this fit, the sum of two Crystal Ball functions is used to account for the low-end and high-end tails.

Fit of simulated data

The double Crystal Ball p.d.f. for simulated $B^+ \rightarrow K^{*+} J/\psi$ and $B^+ \rightarrow K^{*+} \mu \, mmu$ events is given by[1]

$$
\begin{aligned}
\mathcal{P}_{CB}^{MC}(J/\psi) &= f^{J/\psi} \cdot CB_1(\alpha_1^{J/\psi}, n_1^{J/\psi}, \sigma_1^{J/\psi}, \mu^{J/\psi}; m) \\
&+ (1 - f^{J/\psi}) \cdot CB_2(\alpha_2^{J/\psi}, n_2^{J/\psi}, \sigma_2^{J/\psi}, \mu^{J/\psi}; m),
\end{aligned}
$$

with f being the fraction of the first Crystal Ball function, CB_1. $1 - f$ consequently gives the remaining fraction of CB_2. $\mathcal{P}_{CB}^{MC}(\mu\mu)$ is used analogously.

The fit results are shown in Figure 25. The displayed window is decreased to $m \in [5100, 6000] \, \text{MeV}/c^2$ to better visualize the fitted distributions. The pull dis-

---

1 The resonant and non-resonant decay channel are denoted by the upper index "J/ψ" and "$\mu\,\mu$", respectively.
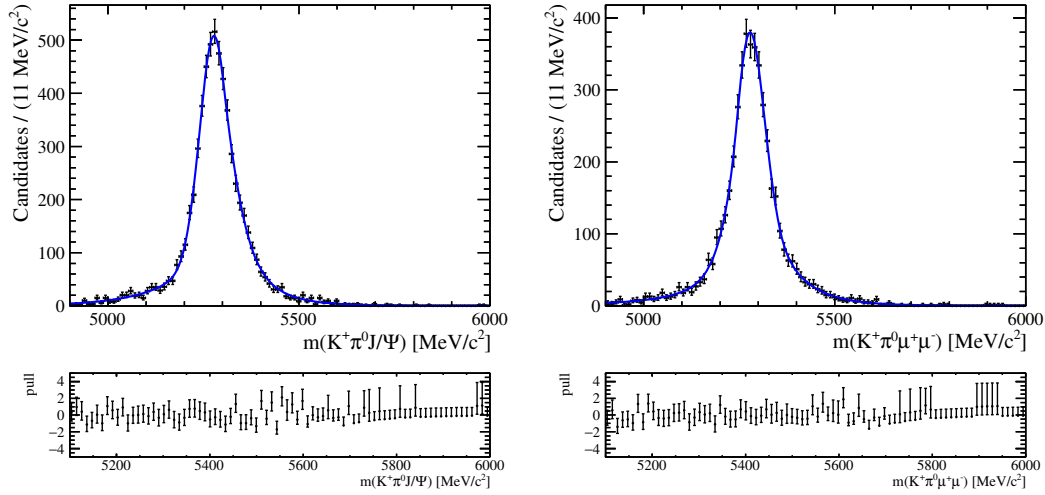
Figure 25: Resonant (left) and non-resonant (right) B^+ mass spectrum from simulation with cuts on the K^{*+} mass window and BDT response with the corresponding pull distributions. The fit model is explained in the text. The fit results are summarized in Table 4.

tributions, which are the deviations of the data distribution from the fit model in units of the error, are also shown. The fit results are summarized in Table 4. The number of reconstructed $B^+ \rightarrow K^{*+}\ J/\psi$ events can later be used to compare the reconstruction efficiencies of the full reconstruction and the partial reconstruction of $B^+ \rightarrow K^{*+}\ J/\psi$ decays (see Section 7.4).

Parameter	Fit result	Parameter	Fit result
$f^{J/\psi}_{MC}$	0.543 ± 0.079	$f^{\mu\mu}_{MC}$	0.588 ± 0.078
$\alpha^{J/\psi}_{1,MC}$	1.20 ± 0.34	$\alpha^{\mu\mu}_{1,MC}$	0.9 ± 0.13
$n^{J/\psi}_{1,MC}$	0.56 ± 0.12	$n^{\mu\mu}_{1,MC}$	2.56 ± 0.66
$\sigma^{J/\psi}_{1,MC}$	$(33.9 \pm 3.8)\,\text{MeV}/c^2$	$\sigma^{\mu\mu}_{1,MC}$	$(35.8 \pm 2.5)\,\text{MeV}/c^2$
$\mu^{J/\psi}_{1,MC}$	$(5271.1 \pm 2.3)\,\text{MeV}/c^2$	$\mu^{\mu\mu}_{1,MC}$	$(5274.5 \pm 2.7)\,\text{MeV}/c^2$
$\alpha^{J/\psi}_{2,MC}$	-1.074 ± 0.11	$\alpha^{\mu\mu}_{2,MC}$	-0.819 ± 0.11
$n^{J/\psi}_{2,MC}$	3.94 ± 0.65	$n^{\mu\mu}_{2,MC}$	5.9 ± 2.3
$\sigma^{J/\psi}_{2,MC}$	$(67.9 \pm 6.0)\,\text{MeV}/c^2$	$\sigma^{\mu\mu}_{2,MC}$	$(57.9 \pm 7.1)\,\text{MeV}/c^2$
$\mu^{J/\psi}_{2,MC}$	$(5314.0 \pm 17.0)\,\text{MeV}/c^2$	$\mu^{\mu\mu}_{2,MC}$	$(5306 \pm 10)\,\text{MeV}/c^2$

Table 4: Fit parameter values for the invariant B^+ mass distribution from data for the resonant (left) and non-resonant (right) decay .

Fit of measured data

In the proceeding step, the resonant distribution of real decays is described. Analog to the simulation fit, the B^+ mass distribution in data is best described by the sum of two Crystal Ball functions. The parameters α, n and μ and are taken from
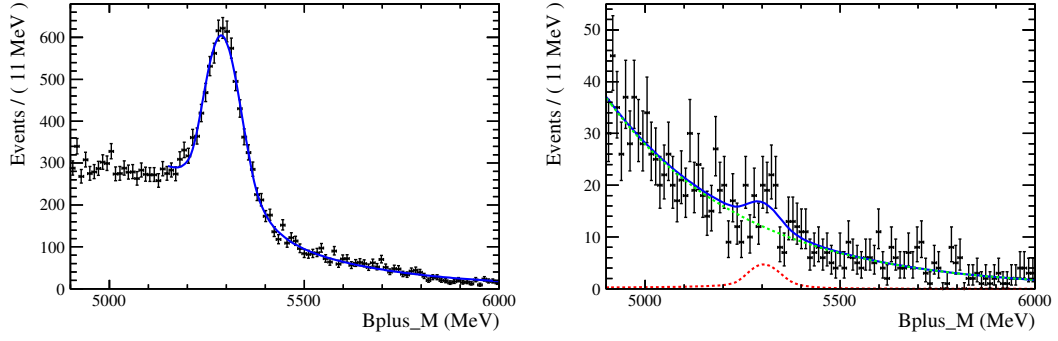
Figure 26: Resonant (left) and non-resonant (right) B^+ mass distribution. The fit models are explained in the text.

the previously determined resonant simulated fits. This ensures that the model only describes the signal region and does not include combinatorial background. The combinatorial background is described by an exponential function and is added to the double Crystal Ball function. The exponential function is defined as follows:

$$\mathcal{P}_{BG} = \frac{1}{N}e^{\lambda^{J/\psi} m}.$$

This concludes to following total fit model:

$$\mathcal{P}^{data}(B^+ \to J/\psi) = N_S^{J/\psi}\left[f_1^{J/\psi} CB_1(\alpha_1^{J/\psi}, n_1^{J/\psi}, \sigma_1^{J/\psi}, \mu^{J/\psi}; m)\right.$$
$$\left. + (1 - f_1^{J/\psi})CB_2(\alpha_2^{J/\psi}, n_2^{J/\psi}, \sigma_2^{J/\psi}, \mu^{J/\psi}; m)\right] + N_B^{J/\psi}\left[e^{\lambda^{J/\psi} m}\right].$$

N_S is the number of signal events and N_B the number of background events. The fit of the resonant sample is plotted in Figure 26 (left). The lower sideband is not fitted here as there are partially reconstructed backgrounds which cause large uncertainties in the shape. The upper sideband includes the combinatorial background which is described by the exponential function. The corresponding fit results are summarized in Table 5.

The non-resonant mass distribution is fitted by the same model as the resonant case. All parameters except the number of signal events $N_S^{K^{*+}\mu\mu}$ as well as the parameter of the exponential background are set to the fit parameters of the resonant fit. The free parameters of the exponential part are λ, which is the slope of the exponential function, and the number of background events $N_B^{K^{*+}\mu\mu}$.

$$\mathcal{P}^{data}(B^+ \to K^{*+}\mu\mu) = \mathcal{P}^{data}(B^+ \to K^{*+}J/\psi)(N_S^{\mu\mu}, N_B^{\mu\mu}, \lambda^{\mu\mu}; m).$$

The fit of the non-resonant data is plotted in Figure 26 (right) and the corresponding fit results are shown in Table 6.

The statistical significance is calculated with *Wilk's theorem* [44]. The log-likelihood value for the particle hypothesis $\mathcal{L}$ and for the background-only hypothesis $\mathcal{L}_0$ is used in order to calculate the significance according to

$$s = \sqrt{\min(2 \cdot \ln(\mathcal{L}_0)) - \min(2 \cdot \ln(\mathcal{L})}.\tag{7}$$

Parameter	Fit result	Parameter	Fit result
f_1	0.602 ± 0.028	$\alpha_{1,\mathrm{MC}}^{J/\psi}$	1.20 ± 0.34
$\sigma_1^{J/\psi}$	$(43.7 \pm 3.0)\,\mathrm{MeV}/c^2$	$n_{1,\mathrm{MC}}^{J/\psi}$	0.56 ± 0.12
$\sigma_2^{J/\psi}$	$(47.4 \pm 2.9)\,\mathrm{MeV}/c^2$	$\mu_{1,\mathrm{MC}}^{J/\psi}$	$(5271.1 \pm 2.3)\,\mathrm{MeV}/c^2$
λ	-0.00313 ± 0.00014	$\alpha_{2,\mathrm{MC}}^{J/\psi}$	-1.074 ± 0.11
$N_S^{J/\psi}$	(7386 ± 207)	$n_{2,\mathrm{MC}}^{J/\psi}$	3.94 ± 0.65
$N_B^{J/\psi}$	(51641 ± 1308)	$\mu_{2,\mathrm{MC}}^{J/\psi}$	$(5314.0 \pm 17.0)\,\mathrm{MeV}/c^2$

Table 5: Fit parameter values for the invariant B^+ mass distribution from data for the resonant decay. The right table shows the fit parameters from simulation which were used in the fit of the resonant decay mode.

Parameter	Fit result
λ	-0.00279 ± 0.00011
$N_S^{\mathrm{mmu\mu}}$	65 ± 21
$N_B^{\mu\mu}$	2667 ± 119

Table 6: Fit parameter values for the invariant B^+ mass distribution from data for the non-resonant decay.

$\min(\ln(\mathcal{L}_0))$ denotes the minimized log-likelihood value for the background-only hypothesis, while $\min(\ln(\mathcal{L}))$ represents the signal hypothesis. The statistical significance results to:

$$s = 3.23\sigma.$$

Variable	Value
$\mathcal{B}(B^+ \to K^{*+} J/\psi)$	$(1.44 \pm 0.08) \times 10^{-3}$
$\mathcal{B}(J/\psi \to \mu\mu)$	$(5.961 \pm 0.033) \times 10^{-2}$
$\epsilon^{K^{*+} J/\psi}$	0.00606
$\epsilon^{K^{*+} \mu\mu}$	0.00449
$N_S^{B^+ \to K^{*+} J/\psi}$	7386 ± 207
$N_S^{B^+ \to K^{*+} \mu\mu}$	65 ± 21

Table 7: Quantities used in the calculation of the branching fraction.

The obtained values for the variables needed to determine the branching fraction are summarized in Table 7. With the number of signal events as well as the selection efficiencies obtained from simulation, the relative branching fraction of

the rare decay $B^+ \to K^{*+} \mu^+ \mu^-$ relative to the non-resonant decay $B^+ \to K^{*+} J/\psi$ can be extracted:

$$\mathcal{R}\frac{\mathcal{B}(B^+ \to K^{*+}\mu\mu)}{\mathcal{B}(B^+ \to K^{*+}J/\psi(\to \mu\mu)} = (0.12 \pm 0.4(\text{stat.})) \times 10^{-4}.$$

With the knowledge of the absolute branching fraction of the reference channel [1], and the branching fraction $\mathcal{B}(J/\psi \to \mu\mu)$, the absolute branching fraction of $B^+ \to K^{*+}\mu\mu$ can be determined:

$$\mathcal{B}(B^+ \to K^{*+}\mu\mu) = (1.02 \pm 0.33(\text{stat.})) \times 10^{-6}.$$

6.3 DISCUSSION OF SYSTEMATIC UNCERTAINTIES

Although the systematic uncertainties cannot explicitly be taken into account in the scope of this thesis, this section will give a brief overview of the expected systematic influences, which can principally be categorized as follows:

- elimination of dimuon resonances in the non-resonant channel

- Discrepancy of Monte Carlo simulation and data

- Possible Contributions from other intermediate resonances in the resonant channel

- Influences of the fit model

ELIMINATING THE DIMUON RESONANCES In the transition of the resonant to the non-resonant decay, all resonances must be vetoed. When the mass window of the dimuon resonances, J/ψ and $\psi(2S)$, does not sufficiently cover their mass distributions, it is possible that individual events are misidentified as signal candidates. As these resonances have radiative tails, a small fraction of resonant events will always pass the veto criteria. With the branching fraction $\mathcal{B}(B^+ \to K^{*+}J/\psi) = (1.44 \pm 0.08) \times 10^{-3}$ and $\mathcal{B}(J/\psi \to \mu\mu) = (5.961 \pm 0.033) \times 10^{-2}$ even a contribution of 1% would distort the signal yield of the non-resonant decay. The mass window which is chosen for the J/ψ and $\psi(2S)$ mass vetoes is selected to be large enough in order to neglect this systematic uncertainty compared to other uncertainties.

DISCREPANCIES OF MC SIMULATION AND DATA Determining the branching ratio is strongly influenced by the comprehension of the simulated data due to the dependency of branching ratio and signal efficiency. A systematic error can arise from the inconsistency of simulated and experimentally measured data which itself can originate in an insufficient simulation of the processes occuring in the detector. Two possibilities to increase this consistency can be the reweighting of Monte Carlo data as well as a re-determination of the PID

variables. Additionally, the efficiency of generated Monte Carlo quantities carries known uncertainties which need to be accounted for.

POSSIBLE CONTRIBUTIONS FROM OTHER INTERMEDIATE RESONANCES   An additional source of systematic uncertainty can originate in the selection of the resonant channel. Cuts on the mass window of the K^{*+} reduces the contribution of higher kaon resonances which also decay into a $K^+ \pi^0$ pair, although a fraction of these contributions can remain as the mass distributions of the resonances overlap to a certain degree. In order to fully identify these contributions, simulated events of these decays can be produced and analyzed.

FIT MODELS   A systematic error is also given by the choice of fit models. The Crystal Ball function and the exponential background model used in the fits can only describe the invariant mass distributions to a certain degree. In the fit of the resonant data distribution only the upper sideband was taken into account for the background model as the lower sideband showed large uncertainties. This influences the signal region fit since there might be an overlap of the lower sideband with the region fitted by the Crystal Ball signal model. Therefore more events are possibly selected as signal events. In a further analysis the partial reconstructed backgrounds in the lower sideband can be modeled and thus the number of signal events can be determined more precisely. Additionally, some parameters are taken from the fit to simulated data. These can be left as free parameters in a further analysis.

All in all, the uncertainty of the determined branching fraction is expected to be governed by statistical uncertainties. In order to determine the final significance of this decay channel, systematic errors must be taken into account.

6.4   CONCLUSION

The branching ratio of the $B^+ \to K^{*+} \mu^+ \mu^-$ decay was determined with 2011 and 2012 data corresponding to an integrated luminosity of approximately $3\,\mathrm{fb}^{-1}$. The number of measured B^+ signal events is 65 ± 21 with a statistical significance of 3.23σ. To determine the relative branching fraction of $B^+ \to K^{*+} \mu\mu$ and $B^+ \to K^{*+}$ J/ψ decays, the invariant B^+ mass distribution was fitted in the both decay modes. The branching fraction of $B^+ \to K^{*+} \mu\mu$ relative to $B^+ \to K^{*+}$ J/ψ concludes to:

$$\frac{\mathcal{B}(B^+ \to K^{*+}\mu\mu)}{\mathcal{B}(B^+ \to K^{*+} J/\psi\,(\to \mu\mu))} = (0.12 \pm 0.4(\mathrm{stat.})) \times 10^{-4}.$$

With the knowledge of the absolute branching fraction of the reference channel [1], and the branching fraction $\mathcal{B}(J/\psi \rightarrow \mu\mu)$, the absolute branching fraction of $B^+ \rightarrow K^{*+} \mu \mu$ was determined:

$$\mathcal{B}(B^+ \rightarrow K^{*+}\mu\mu) = (1.02 \pm 0.33(\text{stat.})) \times 10^{-6}.$$

$$\mathcal{B} = (1.02 \pm 0.33) \times 10^{-6}.$$

This branching fraction is in agreement with other measurements from LHCb [10] and the PDG branching fraction of $\mathcal{B}(B^+ \rightarrow K^{*+}\mu^+\mu^-) = (1.12 \pm 0.15) \times 10^{-6}$. A smaller statistical uncertainty of the branching ratio is desirable. The statistical uncertainty of this measurement is approximately 32.5%. A dominant cause of this large statistical uncertainty originates in the poor reconstruction of π^0 mesons in the detector. This motivates the possible use of a different approach where the reconstruction of π^0 mesons in the detector is circumvented by reconstructing it from decay kinematics. This method is explained and evaluated in the following chapters.

Part 2

Partial reconstruction of
$B^+ \to K^{*+} \, J/\psi$

DEVELOPING THE PARTIAL RECONSTRUCTION TECHNIQUE

After having discussed the full reconstruction of $B^+ \to K^{*+} (\to K^+ \pi^0) \mu^+ \mu^-$ *which lead to low signal yield because of the low* π^0 *reconstruction efficiency in the previous section, the second part of this thesis is devoted to the kinematic reconstruction technique of the* π^0 *and whether this method could serve as an alternative to the standard full reconstruction of* $B^+ \to K^{*+} \mu^+ \mu^-$ *decays..*

7.1 PARTIALLY RECONSTRUCTED DECAYS AT LHCb

As the poor reconstruction of the π^0 in the detector causes large statistical uncertainties, a method of reconstructing the π^0- momentum in terms of quantities which can be well reconstructed in the LHCb detector is desirable. An algorithm can be applied which reconstructs the three momentum of the π^0 kinematically by using the four-momenta of the final state particles μ^+, μ^- and K^+, as well as the masses of the π^0, K^+ and the intermediate resonance K^{*+}.

The additional crucial information needed in order to apply this, is the B^+- flight direction. From this, the invariant B^+ mass can then be derived. This procedure can generally be applied to other decays of charged B mesons which fulfill the constraints of the knowledge of the flight direction of the hadron and a resonance in the decay chain, such as the K^{*+}.

The four momentum of the K^{*+} can then be determined by forming the sum of the K^+ and the partially reconstructed π^0 four momenta. Consequently the invariant B^+ mass can be determined by adding the four momenta of all final state particles, $K^+ \pi^0 \mu^+$ and μ^-.

7.1.1 *Mathematical Procedure*

The following section introduces the kinematical relations used to calculate the π^0 momentum from the other final state particles using the invariant masses of the K^+, K^{*+} and π^0.

As usual in high energy physics, one starts with four-momentum conservation. Further taking the intermediate K^{*+} resonance into account, this results in

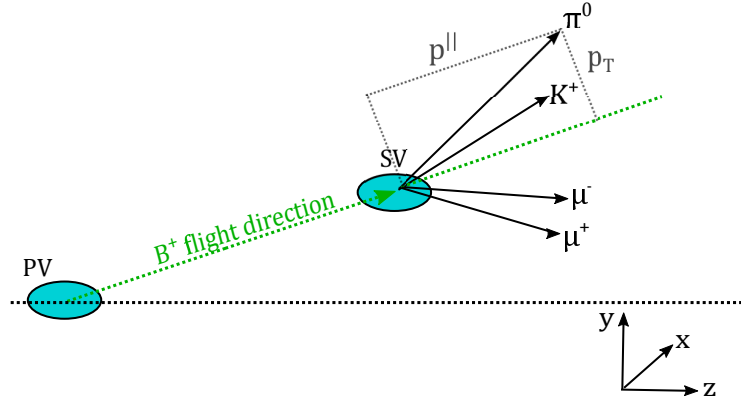$$p_B^\mu p_{B\mu} = (p_{J/\psi}^\mu + p_{K^{*+}}^\mu)^2. \tag{8}$$

Figure 27: Illustration of the projection of the daughter particles' momenta on the flight direction of the B^+. As an example, the parallel and perpendicular parts of the π^0 momentum are drawn. The same procedure applies to the other daughter particles.

The four-momentum conservation of the decay $B^+ \to J/\psi\, K^{*+}$, with the four-momenta p_B^μ, $p_{J/\psi}^\mu$ and $p_{K^{*+}}^\mu$ results in following equation for the B^+ invariant mass:

$$m_B^2 = m_{J/\psi}^2 + m_{K^{*+}}^2 + 2(E_{J/\psi} E_{K^{*+}} - \vec{p}_{J/\psi} \cdot \vec{p}_{K^{*+}}), \qquad (9)$$

with $E_{J/\psi} = \sqrt{\vec{p}_{J/\psi}^2 + m_{J/\psi}^2}$ and $E_{K^{*+}} = E_{K^+} + E_{\pi^0} = \sqrt{\vec{p}_{K^+}^2 + m_{K^+}^2} + \sqrt{\vec{p}_{\pi^0}^2 + m_{\pi^0}^2}$. The four-momentum conservation can furthermore be broken down to momentum and energy conservation, yielding four constraints on the $B^+ \to K^{*+}$ ($K^+ \pi^0$) J/ψ ($\mu^+ \mu^-$) decay chain. With the three-momenta of the B^+ meson, $\vec{p}_B$, the J/ψ meson $\vec{p}_{J/\psi}$, the K^+ meson $\vec{p}_{K^+}$ and the kinematically reconstructed π^0, $\vec{p}_{piz}$, three-momentum conservation concludes to:

$$\vec{p}_B = \vec{p}_{J/\psi} + \vec{p}_{K^+} + \vec{p}_{\pi^0}. \qquad (10)$$

Furthermore, the flight direction of the B^+ meson is used to split the momentum of the B^+ meson into parallel and transverse components with respect to its flight direction.

The parallel component of the B^+ momentum is

$$\vec{p}_B^{\,||} = \vec{p}_{J/\psi}^{\,||} + \vec{p}_{K^+}^{\,||} + \vec{p}_{\pi^0}^{\,||}, \qquad (11)$$

where $\vec{p}_{J/\psi}^{\,||}$, $\vec{p}_{K^+}^{\,||}$ and $\vec{p}_{\pi^0}^{\,||}$ are the components of $\vec{p}_{J/\psi}$, $\vec{p}_{K^+}$ and $\vec{p}_{\pi^0}$ parallel to the B^+ flight direction. The parallel components of the individual momenta are derived by projecting them on the flight direction of the B^+. This is visualized in Figure 27. If the flight direction is defined by the distance vector $\vec{d}$ pointing form the primary to the secondary vertex of the B^+, then

$$p_{J/\psi}^{||} = \frac{\vec{p}_{J/\psi} \cdot \vec{d}}{d} \left(\frac{\vec{d}}{d} \right) \qquad (12)$$

is the parallel projection of J/ψ, and

$$p_{K^+}^{\|} = \frac{\vec{p}_{K^+} \cdot \vec{d}}{d} \left(\frac{\vec{d}}{d} \right) \tag{13}$$

is the parallel projection of K^+. The components of the three-momentum are expressed in the original coordinate system. No coordinate transformation is applied. The perpendicular projection of the B^+ momentum is given by

$$\vec{p}_{B^+}^{\perp} \vec{0} = \vec{p}_{J/\psi}^{\perp} + \vec{p}_{K^+}^{\perp} + \vec{p}_X^{\perp}. \tag{14}$$

By rearranging this, the perpendicular component of the π^0 momentum can be extracted:

$$\vec{p}_{\pi^0}^{\perp} = -\vec{p}_{J/\psi}^{\perp} - \vec{p}_{K^+}^{\perp} \tag{15}$$

$\vec{p}_{J/\psi}^{\perp}$, $\vec{p}_{K^+}^{\perp}$ and $\vec{p}_{\pi^0}^{\perp}$ are the components perpendicular to the flight direction of $\vec{p}_B$. The perpendicular components of the daughter particles can simply be derived by:

$$\vec{p}_{J/\psi}^{\perp} = \vec{p}_{J/\psi} - \vec{p}_{J/\psi}^{\|}, \tag{16}$$

and

$$\vec{p}_{K^+}^{\perp} = \vec{p}_{K^+} - \vec{p}_{K^+}^{\|}. \tag{17}$$

An additional condition is gained by energy conservation,

$$\sqrt{p_B^2 + m_B^2} = \sqrt{p_{J/\psi}^2 + m_{J/\psi}^2} + \sqrt{p_{K^+}^2 + m_{K^+}^2} + \sqrt{p_X^2 + m_{\pi^0}^2}. \tag{18}$$

Rearranging this equation and substituting Equation 9 from four-momentum conservation, Equation 11 and Equation 14 from the parallel and perpendicular projections into this equation, results in a second-order equation. By solving this equation, the two solutions for the parallel component of the π^0 momentum can be derived:

$$p_{\pi^0}^{\|} = A \pm \sqrt{B}, \tag{19}$$

where

$$A = \frac{\left[m_\Delta^2 - 2\vec{p}_{K^+}^{\perp} \cdot \left(\vec{p}_{K^+}^{\perp} + \vec{p}_{J/\psi}^{\perp} \right) \right] p_{K^+}^{\|}}{2(p_{K^+}^{\perp 2} + m_{K^+}^2)} \tag{20}$$

and

$$B = \frac{\left[m_\Delta^2 - 2\vec{p}_{K^+}^{\perp} \cdot \left(\vec{p}_{K^+}^{\perp} + \vec{p}_{J/\psi}^{\perp}\right)\right]^2 E_{K^+}^2}{4(p_{K^+}^{\perp 2} + m_{K^+}^2)^2} - \frac{\left[m_X^2 + \left(\vec{p}_{K^+}^{\perp} + \vec{p}_{J/\psi}^{\perp}\right)^2\right] E_{K^+}^2}{(p_{K^+}^{\perp 2} + m_{K^+}^2)}, \quad (21)$$

with $m_\Delta^2 = m_{K^{*+}}^2 - m_{K^+}^2 - m_{\pi^0}^2$ and $E_{K^+}^2 = p_{K^+}^2 + m_{K^+}^2$.

Considering the masses used to calculate m_Δ^2, it is important to point out that the PDG masses are used in the analysis. This implies the constraint of the K^{*+} resonance to a constant mass, implying a width of zero. In fact, the resonance has a natural width of $\Gamma_{K^{*+}} = (50.8 \pm 0.9)\,\text{MeV}/c^2$ [1], as it has been previously pointed out in Chapter 5. When the K^{*+} is assigned a constant mass, the B^+ will acquire values which are either too large or too small since the real K^{*+} mass is either larger or smaller than the nominal mass $m(K^{*+}) = (891.7 \pm 0.3)\,\text{MeV}/c^2$. This will lead to a broadening of the invariant B^+ mass distribution which has to be taken into account when the invariant B^+ mass distribution is modeled (see Section 7.3.1).

Further, the momentum vector $\vec{p}_{\pi^0}^{\parallel}$ can be determined by multiplying $p_{\pi^0}^{\parallel} = A \pm \sqrt{B}$ with the normalized distance vector $\frac{\vec{d}}{d}$. As there are two solutions for $p_{\pi^0}^{\parallel}$, also two momentum vectors $\vec{p}_{\pi^0}^{\parallel}$ exist.

With the knowledge of the perpendicular and parallel components, $\vec{p}_{\pi^0}^{\parallel}$ and $\vec{p}_{\pi^0}^{\perp}$, the four momentum of the π^0 can be calculated. By adding the K^+ four momentum, the K^{*+} four momentum can be calculated: $p_{K^{*+}} = p_{\pi^0} + p_{K^+}$. Finally, the B^+ mass can be determined according to:

$$m^2(B^+) = (p_{K^+} + p_{\pi^0} + p_{\mu^+} + p_{\mu^-})^2.$$

7.2   SELECTION

In the scope of this analysis a general tool was created which allows the application of the partial reconstruction method to any other decay channels which fulfill the requirements such as an intermediate resonance and a known flight direction of the decaying particle. In this manner, it is possible to implement this tool into the *DaVinci* [45] framework to create nTuples before the application of pre-selection cuts.

Because of the higher event yield, the development and feasibility studies of the partial reconstruction technique is performed on samples which include resonant $B^+ \rightarrow K^{*+}\,J/\psi\,(\rightarrow \mu^+\,\mu^-)$ decays instead of the rare $B^+ \rightarrow K^{*+}\,\mu^+\,\mu^-$ decays .

The partial reconstruction technique is derived on a simulated data sample which is the same as the one to study the full reconstruction of $B^+ \rightarrow K^*\,J/\psi$. This simulated data sample allows to study the determination of the $p_X^{\parallel}$ momentum, since

there are two possible solutions. Examining the influence of reconstructed and true quantities on the invariant B^+ mass distribution helps delivering insight into the behavior of the partial reconstructed B^+ mass in these different scenarios. This simulated data sample includes the full reconstruction of the π^0 as well as preselection cuts on the π^0 such as a minimum transverse momentum of $800\,\mathrm{MeV/c}$ as in Table 1 in Chapter 5. Since the π^0 now is reconstructed kinematically and not in the detector, a different signal sample is desired, which does not include the reconstructed π^0 and has no restrictions on its properties such as the momentum. In this manner, the signal yield and therefore the efficiency of the partially reconstructed $B^+ \to K^{*+} J/\psi$ decay can be increased.

Thus, another simulated data sample is created which uses the stripping line *StrippingJpsiForSL* (Stripping20). This includes all $J/\psi \to \mu^+ \mu^-$ candidates. Additionally, the J/ψ must also have a common vertex with another track such that the combination is consistent with a fully or partially reconstructed $B \to J/\psi\ h$ decay, with a hadron h. The corresponding selection cuts are summarized in Table 9.

In a first approach, the partial reconstruction technique is applied to a $B^+ \to K^{*+} J/\psi$ data sample of 2011 data with positive magnet polarity, corresponding to $1\,\mathrm{fb}^{-1}$. A multivariate analysis is performed to extract the signal. It becomes clear that various peaking backgrounds contribute to the B^+ mass and need to be regarded in detail in order to extract the true number of signal events. As is it not trivial which background sources mimic the signal and which ones can be separated easily from the signal region, a study on a simulated data sample which approximately reflects background composition in measured data is crucial. A simulated *inclusive* $B \to J/\psi$ sample is therefore used which includes all charmonium decays of B mesons. The relative branching fractions are taken from [1]. Table 8 shows a list of the previously stated samples and the Stripping selection used to create them.

In the following, the index π^0_{PR} refers to the partially reconstructed π^0.

Type	Name	Stripping Selection
Simulation	Signal Sample 1	*B2XMuMu* (Stripping20)
Simulation	Signal Sample 2	*JpsiForSL* (Stripping20)
Simulation	Inclusive Sample	*JpsiForSL* (Stripping20)
Data	Data sample	*JpsiForSL* (Stripping20)

Table 8: Overview of the different samples used in this analysis of the partial reconstruction technique.

7.3 STUDY OF RESOLUTION EFFECTS

Before investigating the B^+ invariant mass distribution, several steps which lead to the partially reconstructed B^+ mass need to be discussed.

Variable description	Cut
B^+ minimum mass	$> 3400\,\mathrm{MeV}/c^2$
B^+ maximum mass	$> 6000\,\mathrm{MeV}/c^2$
B^+ minimum p_T	$> 800\,\mathrm{MeV}/c$
B^+ minimum direction angle	> 0.9995
B^+ minimum χ^2_{FD}	> 200
Muon χ^2_{IP}	> 4.0
Muon χ^2	< 3.0
Muon p_T	$> 1200\,\mathrm{MeV}/c$
Muon p	$> 6000\,\mathrm{MeV}/c$
J/ψ p_T	$> 500\,\mathrm{MeV}/c$
J/ψ minimum χ^2_{FD}	> 100
J/ψ mininum direction angle	> 0.99
SPD Track Multiplicity	< 600
Track p_T	$> 500\,\mathrm{MeV}/c$
Track p	$> 3000\,\mathrm{MeV}/c$
Track χ^2	< 3
Track χ^2_{IP}	> 9

Table 9: Selection cuts for $B^+ \rightarrow J/\psi$ X in the *StrippingJpsiForSL* Stripping line (Stripping20). "Muon" refers to a single muon, thus either μ^+ or μ^+, while "J/ψ " refers to the dimuon system.

As the π^0 mass as well as the K^{*+} mass are set to their nominal PDG masses in the kinematic reconstruction of the π^0, it does not make any sense to show the corresponding mass distributions as it was done in the full reconstruction of the B^+. Nevertheless, intermediate steps in the reconstruction of the π^0 momentum can be investigated and evaluated:

The parallel component of the π^0 momentum, $p^{||}_{\pi^0}$ has two solutions $p^{||}_{\pi^0} = A \pm \sqrt{B}$. A positive value of B, which is calculated from the final state particles of the assumed B^+ mass candidate according to Equation 21, is necessary, since the square root of this value is taken when $p^{||}_{\pi^0}$ is determined. Therefore it is crucial to study the B distribution in order to determine the number of events which correspond to a positive value of B. In Figure 28 the term B is shown. The fraction of events which correspond to a positive value of B amounts to approximately 75.9%. The negative B values occur due to resolution effects from the reconstruction of the tracks of the particles K^+, μ^+ and μ^-. Background events, on the other hand, will also often correspond to a negative B.

In a further step, the total π^0 momentum[1] distribution can be inspected. There are two solutions for the parallel momentum ($p^{||}_{\pi^0} = A \pm \sqrt{B}$) but only one solution per event is chosen to determine the total π^0 momentum. This is done as follows: The corresponding kinematically reconstructed B^+ mass is determined for both so-

---

1 This is the sum of the transverse and parallel components of the π^0 momentum.
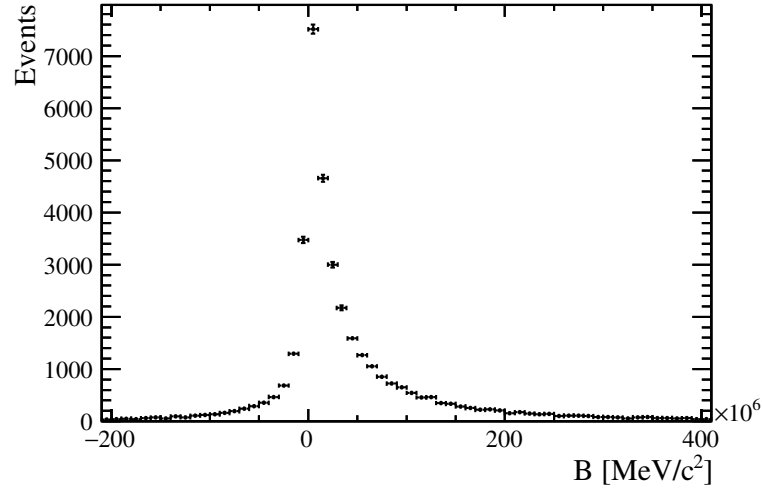
Figure 28: The distribution of term B from Equation 21 showing negative and positive values. Only 75.9% events have $B \geqslant 0$.

lutions. For each event, the B^+ mass solution which is closer to the nominal PDG B^+ mass, is chosen, which is the best possible solution, resulting in the two masses $m(B^+)_{1/2}$. The corresponding magnitude of the π^0 momentum distribution from a simulated signal sample is depicted in Figure 29. It shows the momentum of the kinematically reconstruced π^0 (magenta) as well as the π^0 momentum from full reconstruction (blue).

With the knowledge of this momentum, the mass of the B^+ meson can be reconstructed using Equation 9. To investigate the partial reconstruction method, its effect on the width of the B^+ meson is analyzed as follows.

The quantities which are used in the reconstruction of the π^0 momentum are the momenta of the particles K^+, μ^+ and μ^-, the flight flight direction of the B^+ as well as the masses of K^{*+}, K^+ and π^0. Since the masses are set to their nominal PDG value, the performance of the partial reconstruction method depends on how precisely the flight direction of the B^+ and therefore the primary and secondary B^+ vertex, as well as the momenta of the daughter particles, K^+, μ^+ and μ^- can be measured. The performance can be tested by using a simulated data sample and studying the influence of momenta and primary and secondary vertices by using generated[2] and reconstructed quantities. As in the calculation of the π^0 momentum also the calculation of the B^+ mass distribution has two solutions, $m(B^+)_{1/2}$ but only one solution per event is chosen to determine the B^+ invariant mass. This is done analog to the π^0 momentum determination: The corresponding kinematically reconstructed B^+ mass is determined for both solutions. The best possible case is obtained when the B^+ mass solution which is closest to the nominal PDG B^+ mass, is chosen, as it was done in the determination of the π^0 momentum. This is referred to as the *correct* solution in the following. The *wrong* solution, on the other hand, refers the solution which lies further from the B^+ PDG mass.

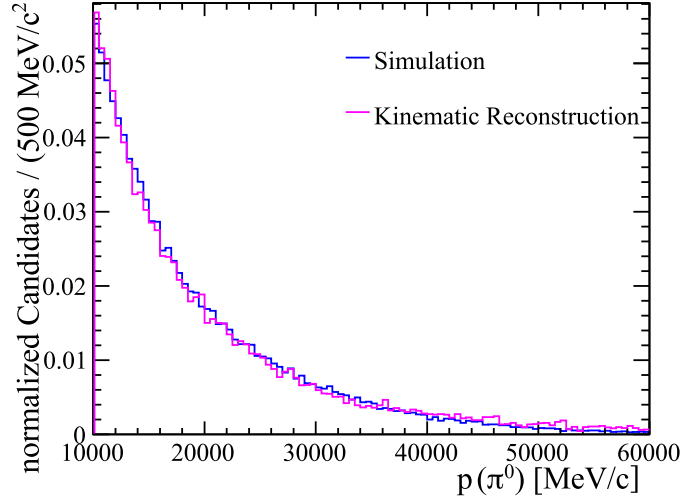2 The generated momenta and vertices are referred to as *true* in the following.

Figure 29: Superimposed histograms of the magnitude of the momentum of the π^0 as determined from full reconstruction and partial reconstruction. A simulated signal sample is used in both cases. The best solution of $p^{\parallel}_{\pi^0} = A \pm \sqrt{B}$ is chosen, as explained in the text.

The study of the performance of the partial reconstruction method combination of correct and wrong solutions with generated and reconstructed momenta of K^+, μ^+ and μ^-, as well as B^+ vertices proceeds in following steps:

CASE 1 The best solution of $m(B^+)_{1/2}$ is taken and true quantities are used for both vertices as well as the momenta.

CASE 2 The worst solution of $m(B^+)_{1/2}$ is taken and true quantities are used for both vertices as well as the momenta.

CASE 3 The best solution of $m(B^+)_{1/2}$ is taken as well as true momenta. The reconstructed primary vertex and the true secondary vertex is used.

CASE 4 The best solution of $m(B^+)_{1/2}$ is taken as well as true momenta. The reconstructed secondary and the true primary vertex is used.

CASE 5 The best solution of $m(B^+)_{1/2}$ is taken as well as true momenta. Both the primary and secondary vertex are reconstructed.

CASE 6 The best solution of $m(B^+)_{1/2}$ is taken. The primary and secondary vertices as well as the momenta are reconstructed. As the reconstructed quantities in the simulation use exactly the same reconstruction algorithms as measured data, this situation represents the most realistic scenario.

The steps are again summarized in Table 10.

Case	Choice of $p_X^{\parallel}$	Choice of PV	Choice of SV	Momenta
Case 1	Correct	True PV	True SV	True Momenta
Case 2	Wrong	True PV	True SV	True Momenta
Case 3	Correct	Rec. PV	True SV	True Momenta
Case 4	Correct	True PV	Rec. SV	True Momenta
Case 5	Correct	Rec. PV	Rec. SV	True Momenta
Case 6	Correct	Rec. PV	Rec. SV	Rec. Momenta

Table 10: Classification of the choice of solutions of Equation 19, vertex reconstruction (B^+ primary and secondary vertex and momenta of K^+ and J/ψ.

7.3.1 The fit model

The different mass distributions for the individual cases are fitted with an "empiric" model consisting of the sum of a relativistic Breit Wigner and a bifurcated Gaussian plus a Gaussian. It is important to point out here, that the shape of the partially reconstructed invariant B^+ mass distribution is not fully understood. What influences the shape, are following aspects. The non-negligible width of the K^{*+} resonance[3], and its propagation in the partially reconstructed B^+ mass as well as detector effects which are represented by the Gaussian "smearing". The signal shape is well described by the sum of the relativistic Breit Wigner with the bifurcated Gauss plus a Gaussian interference term, which are each described in the following:

The Gaussian distribution is defined by a mean and width (μ and σ) and is given by:

$$\mathcal{P}_{Gauss}(m; \mu, \sigma) = \frac{1}{N} \frac{1}{\sigma\sqrt{2\pi}} exp(\frac{-(m-\mu)}{2\sigma^2}). \tag{22}$$

In contrast to the "regular" Gaussian, the bifurcated Gaussian distribution has a different value for σ on either side of the mean:

$$\mathcal{P}_{BiGauss}(m; \mu, \sigma) = \frac{1}{N} \frac{1}{\sigma\sqrt{2\pi}} exp(-(m-\mu)^2/(2\sigma(m-\mu)^2)), \tag{23}$$

where $\sigma(m-\mu) = \sigma_L$ for $m < \mu$ and σ_R for $m \geqslant \mu$.

The Breit Wigner distribution is a continuous probability distribution, with its form arising from the propagation of unstable particles. It is similar to a Gaussian near the peak, but the tails of the curve are flatter. Its probability density function is given by the following ([46]):

$$\mathcal{P}_{RBW}(m; m_0, \Gamma_0, J, R) = \frac{1}{N} \frac{m^2}{(m^2 - m_0^2)^2 + m_0^2 \Gamma^2(m)}. \tag{24}$$

---

3 In the partial reconstruction the K^{*+} mass was set to the constant PDG value, as described in the previous section.

The width Γ of this function is dependent on the mass:

$$\Gamma(m) = \Gamma_0 \frac{m_0}{m} \left(\frac{k(m)}{k(m_0)} \right)^{2J+1} \frac{F(Rk(m))}{Rk(m_0)}, \tag{25}$$

with

$$k(m) = \frac{m}{2} \left(1 - \frac{(m_a + m_b)^2}{m^2} \right)^{1/2} \left(1 - \frac{(m_a + m_b)^2}{m^2} \right). \tag{26}$$

In Equation 25, Γ_0 is the width of the resonance, m_0 its mass, J the spin and R the interaction radius. The parameters m_a and m_b are the masses of the daughter particles, K^+ and π^0. The corresponding values for these parameters are $J = 1$, $R = 0.003 \, \mathrm{MeV}/c^{2\,-1}$, $m_a = 135 \, \mathrm{MeV}/c^2$ (π^0) and $m_b = 494 \, \mathrm{MeV}/c^2$ (K^+). As pointed out before, the K^{*+} resonance is set to the nominal PDG mass in the kinematic reconstruction of the π^0. Not taking the K^{*+} width into account will lead to a broadening of the visible B^+ mass distribution. Since this propagation effect needs to be considered, the width Γ_0 of the B^+ resonance is left as a free parameter in the fit. The function F is a spin-dependent Blatt-Weisskopf form factor:

$$F^{J=1}(x) = \frac{1}{1 + x^2} \tag{27}$$

All three distributions are normalized by the number N of events in the fitted area, in order to serve as probability density functions. Consequently, the complete fit model is given by

$$\mathcal{P}_{\mathrm{tot}} = f_{\mathrm{RBW}} \mathcal{P}_{\mathrm{RBW}} + f_{\mathrm{BiGauss}} \mathcal{P}_{\mathrm{BiGauss}} + f_{\mathrm{Gauss}} \mathcal{P}_{\mathrm{Gauss}},$$

where f_{RBW}, f_{Bigauss} and f_{Gauss} are the fractions of $mathcalP_{\mathrm{RBW}}$, f_{BiGauss} and $\mathcal{P}_{\mathrm{Gauss}}$, respectively. For case 3 - 6, the one common mean is used for the three distributions. This is done to enable the determination of a resolution of the distribution. Case 1 is fitted with different means as the Gaussian function is used to describe the lower tail in the distribution. The fractions f_{RBW}, f_{BiGauss} and f_{Gauss} are normalized to 1 and f_{Gauss} is calculated via: $f_{\mathrm{Gauss}} = (1 - f_{\mathrm{RBW}} - f_{\mathrm{Bigauss}})$. During the development of this fit model, several alternative models have been tested. As the widths of the bifurcated Gaussian only differ slightly from each other, the intuitive choice of a fit model is the sum of three Gaussian functions. This model has been tested as well and proven to agree less with the signal shape than the model stated above.

Figure 30a - Figure 30f show the fitted B^+ invariant mass distributions for the different cases and Table 11 the corresponding fit results. In Figure 30a case1 is plotted. The mass window is chosen smaller than for the other distributions since the asymptotical case has a significantly smaller width ($\sigma_{\mathrm{RBW}} = (9.58 \pm 0.37) \, \mathrm{MeV}/c^2$) than the other cases which have widths in the range of $(60 - 80) \, \mathrm{MeV}/c^2$. Taking the wrong solution clearly decreases the resolution of the distribution (Figure 30b).

Parameter	Case 1	Case 3	Case 4	Case 5	Case 6
m_0 [MeV/c^2]	5279.1 ± 0.1	5277.3 ± 0.7	5276.7 ± 0.9	5276.1 ± 0.7	5280.2 ± 1.0
σ_{RBW} [MeV/c^2]	9.24 ± 0.47	60.9 ± 2.5	79.3 ± 3.3	59.5 ± 2.4	78.6 ± 4.1
$mean_{BiGauss}$ [MeV/c^2]	5276.7 ± 1.2	5277.3 ± 0.7	5276.7 ± 0.9	5276.1 ± 0.7	5280.2 ± 1.0
σ_L [MeV/c^2]	30.2 ± 1.4	99.7 ± 3.1	121.7 ± 3.7	95.8 ± 2.4	122.2 ± 3.2
σ_R [MeV/c^2]	28.7 ± 1.2	84.2 ± 2.2	99.8 ± 2.9	81.7 ± 2.1	104.0 ± 2.5
$mean_{Gauss}$ [MeV/c^2]	5249.2 ± 1.7	5277.3 ± 0.7	5276.7 ± 0.9	5276.1 ± 0.7	5280.2 ± 1.0
σ_{Gauss} [MeV/c^2]	100.1 ± 1.9	224.4 ± 5.5	256.0 ± 6.4	218.6 ± 6.1	267.7 ± 6.5
f_{RBW}	0.365 ± 0.016	0.282 ± 0.017	0.285 ± 0.018	0.300 ± 0.016	0.238 ± 0.018
$f_{BiGauss}$	0.376 ± 0.012	0.491 ± 0.017	0.472 ± 0.019	0.492 ± 0.018	0.522 ± 0.019
f_{Gauss}	0.259 ± 0.020	0.227 ± 0.017	0.253 ± 0.026	0.208 ± 0.024	0.240 ± 0.026

Table 11: Fit results of the different cases in Table 10. The fit model is explained in the text.

Since the resolution of this distribution is very bad, it is not fitted. The implementation of reconstructed vertices degrades the mass resolution (case 3, case 4, case 5). The reconstructed secondary vertex (case 4) has a slightly more negative effect on the B^+ mass resolution than the reconstructed primary vertex (case 3). This can be explained by the fact that the secondary vertex is reconstructed by only combining the three tracks of K^+, μ^+ and μ^-, while for the reconstruction of the primary vertex more tracks are available. The impact of reconstructed momenta on the other hand, only has a small effect (case 5 $\leftrightarrow$ 6).

7.4 RESOLUTION AND EFFICIENCY

To quantify the performance of the partial reconstruction, the efficiency of partially reconstructed $B^+ \to K^{*+} J/\psi$ decays is compared to the corresponding efficiency in the full reconstruction of $B^+ \to K^{*+} J/\psi$. Additionally, the resolution of the corresponding B^+ mass distributions is compared in the partial and full reconstruction.

As previously mentioned in Section 7.2, in the partial reconstruction the restrictions on π^0 properties are omitted by choosing a different stripping line where the π^0 is not reconstructed, which is the JpsiforSL Stripping line (see Table 9. This results in a different simulated signal distribution of the invariant B^+ mass since the number of $B^+ \to K^{*+} J/\psi$ signal events which have passed the selection procedure differ from the full reconstruction. The corresponding fitted distribution is shown in Figure 32 (left). For comparison, the right plot in Figure 32 shows the simulated signal distribution obtained in the full reconstruction. The fit model consists of two double Crystal Ball functions and is explained in Chapter 6. The distribution below the mass $m(B^+) < 4900$ MeV/c^2 can not be fitted, since the stripping selection requires a minimum mass of $m(B^+) > 4900$ MeV/c^2. Nevertheless, the fit is extrapolated into the the region below the cut. The fit results for both fits are summarized in Table 12. As pointed out previously, a positive value of B is necessary, since the square root of this value is taken when $p_{\pi^0}^{\parallel}$ is determined . In Figure 31 the term B is shown. The fraction of events which correspond to a positive value of

(a) Case 1

(b) Case 2
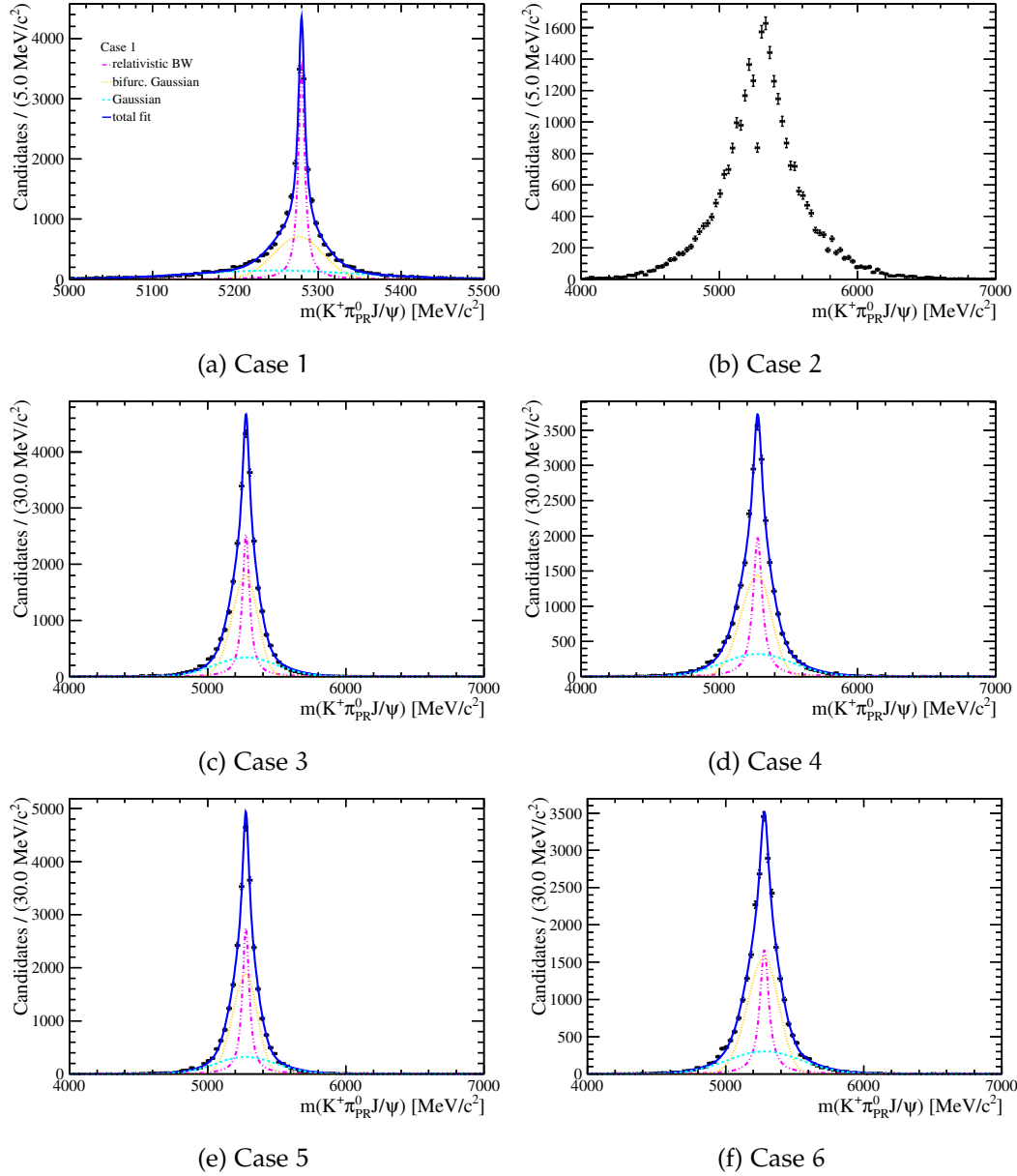
(c) Case 3

(d) Case 4

(e) Case 5

(f) Case 6

Figure 30: Distributions of the different cases in Table 10. The fit model is the sum of relativistic Breit-Wigner, bifurcated Gaussian and Gaussian. The fit results are shown in in Table 11.

B amounts to approximately 59.1%. Analog to the previous resolution studies, the B^+ mass distribution from simulation (with the new stripping selection) is fitted with the same model consisting of a relativistic Breit Wigner function, a bifurcated Gaussian and a Gaussian with common means:

$$\mathcal{P}_{tot} = f_{RBW}\mathcal{P}_{RBW} + f_{BiGauss}\mathcal{P}_{BiGauss} + f_{Gauss}\mathcal{P}_{Gauss}.$$
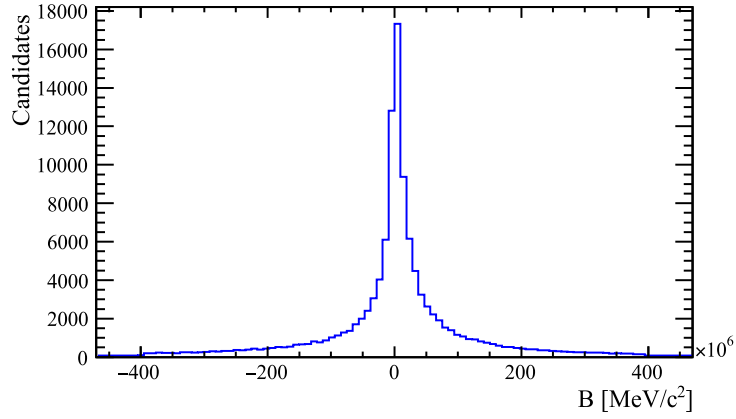
Figure 31: The distribution of term B from Equation 21 showing negative and positive values. Only 59.1% events have B ⩾ 0.
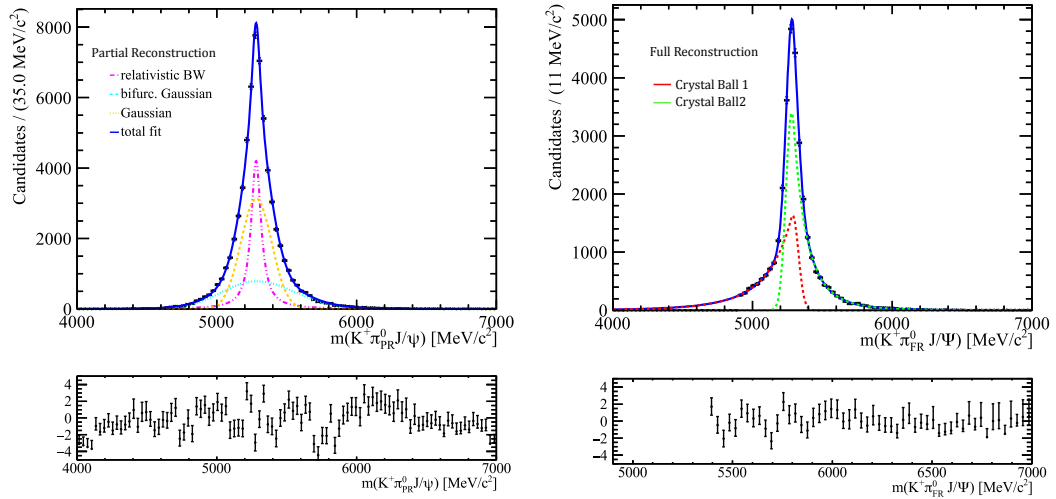
Figure 32: Left: Fit of $m(K^+\pi^0_{PR}J/\psi)$ distribution from partial reconstruction. Right: Fit of $m(K^+\pi^0_{FR}J/\psi)$ distribution from full reconstruction.

Partial Reconstruction	
Parameter	Fit result
$\mathrm{mean}[\mathrm{MeV}/c^2]$	5281.2 ± 0.9
$\sigma_{RBW}[\mathrm{MeV}/c^2]$	85.4 ± 2.5
$\sigma_{L}[\mathrm{MeV}/c^2]$	109.3 ± 2.3
$\sigma_{R}[\mathrm{MeV}/c^2]$	107.4 ± 2.0
$\sigma_{Gauss}[\mathrm{MeV}/c^2]$	253.7 ± 4.6
f_{RBW}	0.287 ± 0.012
$f_{BiGauss}$	0.445 ± 0.012
f_{Gauss}	0.268 ± 0.010

Full Reconstruction	
Parameter	Fit result
$\mathrm{mean}[\mathrm{MeV}/c^2]$	5285.2 ± 5.1
$\sigma_{1}[\mathrm{MeV}/c^2]$	40.7 ± 3.9
$\sigma_{2}[\mathrm{MeV}/c^2]$	40.5 ± 1.0
α_{1}	0.23 ± 0.08
α_{2}	-0.435 ± 0.024
n_{1}	6.0 ± 1.9
n_{2}	5.2 ± 0.3
f_{CB_1}	0.423 ± 0.031
f_{CB_2}	0.577 ± 0.031

Table 12: Fit parameter values for the invariant B^+ mass $m(K^+\pi^0_{PR}J/\psi)$ from partial reconstruction (left) and full reconstruction (right).

7.4.1 *Resolution*

To compare the B^+ mass resolution in the full and partial reconstruction, the resolution of both distributions in Figure 32 is determined by calculating the weighted widths of each distribution. For the partial reconstruction this is done as follows:

$$\sigma = \sqrt{f_{RBW}\sigma^2_{RBW} + f_{BiGauss}\sigma^2_{BiGauss} + f_{Gauss}\sigma^2_{Gauss}},$$

where the weights are given by the fractions f_{RBW}, $f_{BiGauss}$ and f_{Gauss} in the fit of the partially reconstructed B^+ mass $m(K^+\pi^0_{PR}J/\psi)$. As the bifurcated Gaussian has two different widths, this must be taken into account by weighting the two parts as well. In the full reconstruction the weights are given by the fraction of the two Crystal Ball functions used in the corresponding fit (see **??**), f_{CB_1} and f_{CB_3}:

$$\sigma = \sqrt{f_{CB_1}\sigma^2_{CB_1} + f_{CB_2}\sigma^2_{CB_2}}$$

The resolutions obtained for the partially (PR) and fully reconstructed (FR) B^+ mass distribution yield:

$$\sigma_{PR} = (184.3 \pm 1.6)\,\mathrm{MeV}/c^2$$
$$\sigma_{FR} = (174.1 \pm 1.2)\,\mathrm{MeV}/c^2$$

Consequently, the application of the partial reconstruction degrades the invariant B^+ mass resolution from simulation compared to the full reconstruction of $B^+ \rightarrow K^{*+}J/\psi$ only by about 5%.

7.4.2 *Efficiency*

Similar to Section 6.1, the total signal selection efficiency can be divided into several steps. The total signal selection efficiency ϵ^{PR} of the partial reconstruction then is the product of all individual efficiencies:

$$\epsilon^{PR} = \epsilon_{acc}^{PR} \cdot \epsilon_{tr}^{PR} \cdot \epsilon_{r_c}^{PR} \cdot \epsilon_{r_{\pi^0}}^{PR} \cdot \epsilon_{str}^{PR}.$$

Again, ϵ_{acc}^{PR} takes into account that only a fraction of the $B^+ \to K^{*+} J/\psi$ decays lies within the acceptance of the detector. ϵ_{tr}^{PR} is the fraction of events that further have passed the trigger. The stripping efficiency of the partial reconstruction is ϵ_{str}^{PR}. While a single reconstruction efficiency was previously used for the reconstruction of K^+, μ^+, μ^- and π^0 in Section 6.1, now the reconstruction efficiency of these particles is split into the reconstruction of the charged particles K^+, μ^+ and μ^-, called $\epsilon_{r_c}^{PR}$ and the reconstruction efficiency of the π^0, called $\epsilon_{r_{\pi^0}}^{PR}$.

For the full reconstruction, the total signal selection efficiency is determined in the same manner:

$$\epsilon^{FR} = \epsilon_{acc}^{FR} \cdot \epsilon_{tr}^{FR} \cdot \epsilon_{r_c}^{FR} \cdot \epsilon_{r_{\pi^0}}^{FR} \cdot \epsilon_{str}^{FR}.$$

The reconstruction efficiency $\epsilon_{r_{\pi^0}}^{PR}$ of the neutral pion cannot be determined in the partial reconstruction, since this particle is reconstructed kinematically and thus there is no π^0 truth information in the simulated data sample[4]. Therefore the π^0 reconstruction efficiency in partial and full reconstruction cannot be compared absolutely. By taking the ratio ϵ of the total efficiencies though, the efficiencies ϵ_{acc}, ϵ_{tr} and ϵ_{r_c} cancel since ϵ_{acc} and ϵ_{tr} are the same in the partial and full reconstruction as the same trigger line is used in both reconstruction methods. the number of generated $B^+ \to K^{*+} J/\psi$ decays is equal. Consequently, the relative difference in the efficiencies should originate in the difference of the π^0 reconstruction efficiency for partial and full reconstruction, respectively:

$$\epsilon = \frac{\epsilon^{PR}}{\epsilon^{FR}} = \frac{\epsilon_{r_{\pi^0}}^{PR}}{\epsilon_{r_{\pi^0}}^{FR}} \cdot \frac{\epsilon_{str}^{PR}}{\epsilon_{str}^{FR}}$$

With the number of selected events N_{sel} from $B^+ \to K^{*+} J/\psi$ decays, the relative efficiency can finally be broken down to:

$$\epsilon = \frac{N_{sel}^{PR}}{N_{gen}^{PR}} \Big/ \frac{N_{sel}^{FR}}{N_{gen}^{FR}} = \frac{N^{PR}}{N^{FR}}.$$

N_{sel} is determined from the simulated data sample which has passed the stripping selection by matching K^+, J/ψ and B^+ with their generator particles. The K^+

---

4 The truth matching of a Monte Carlo object matches the particle with its generator particle.

is required to originate in a K^{*+} and stem from a B^+ decay. The J/ψ must also originate in a B^+. As stated above, no restrictions on the π^0 can be made in the partially reconstructed $B^+ \to K^{*+} J/\psi$ selection. To be consistent, this also applies to N_{sel}^{FR}, the number of fully reconstructed $B^+ \to K^{*+} J/\psi$ events. The errors are Poisson errors [47]. N_{sel} also includes that only 59.1% of the events which have passed trigger and offline selection criteria are partially reconstructed due to the requirement of a positive value for B in the solution for the parallel momentum, $p_{\pi^0}^{\parallel} = A \pm \sqrt{B}$.

$$N_{sel}^{PR} = 64318 \pm 254$$
$$N_{sel}^{FR} = 31607 \pm 178$$

This results in a relative $B^+ \to K^{*+} J/\psi$ signal selection efficiency of:

$$\epsilon = 2.08 \pm 0.01.$$

This is an estimation which does not take into account the systematic uncertainties of ϵ_{acc}, ϵ_{tr} and ϵ_{r_c} as well as systematic uncertainties in the number of generated $B^+ \to K^{*+} J/\psi$ decays. Nevertheless, this preliminary estimation still shows that the efficiency of partially reconstructing $B^+ \to K^{*+} J/\psi$ decays is significantly larger than the full reconstruction of $B^+ \to K^{*+} J/\psi$ decays. Therefore, the application of the partial reconstruction method to measured data is a useful approach in reconstructing $B^+ \to K^{*+} J/\psi$ decays. Determining the branching fraction of $B^+ \to K^{*+} \mu\mu$ via the full reconstruction resulted in a large statistical uncertainty which arose from the bad π^0 reconstruction efficiency. By applying the kinematic reconstruction to measured data, this statistical uncertainty can be lowered as the π^0 reconstruction efficiency is significantly larger. The resolution of the invariant B^+ mass distribution is only slightly degraded in the partial reconstruction. The application of the partial reconstruction technique is demonstrated in the following chapter.

APPLICATION STUDIES

In this chapter, application studies of the partial reconstruction technique are shown. After performing a multivariate analysis to eliminate background contributions, the partial reconstruction technique is applied to a $B^+ \to K^{*+} J/\psi$ data sample. The application of the partial reconstruction method to measured data shows that various peaking backgrounds contribute to the B^+ signal and need to be regarded in detail in order to extract the true number of signal events. As is it not trivial which background sources mimic the signal and which ones can be separated easily from the signal region, a study on a simulated data sample which approximately reflects the content of backgrounds in measured data is performed.

8.1 MULTIVARIATE SELECTION

Various background sources can be suppressed by the application of a multivariate selection. For the training, simulated $B^+ \to K^{*+} J/\psi$ events are used as the signal template[1], while real data is used as the background template. A data sample of 2012 data with positive magnet polarity is used, corresponding to $1\,\text{fb}^{-1}$. In the full reconstruction of $B^+ \to K^{*+} \mu \mu$, the sideband region of the B^+ invariant mass distribution, $m(B^+) > 5700\,\text{MeV/c}^2$, was used as the background template. This was done since the main background contribution in the full reconstruction is combinatorial background and the sideband region is assumed to exclusively include this type of background. The effect of using the sideband region $m(B^+) > 5700\,\text{MeV/c}^2$ as a background template in the partial reconstruction can be seen in Figure 33. The left plot shows the B^+ mass distribution before cuts[2]. After the application of the BDT cut the shape is nearly unchanged. As $m(B^+) > 5700\,\text{MeV/c}^2$ mainly includes combinatorial background, this indicates that the background composition in the partial reconstruction is mainly not of combinatorial nature. A better background template for the partial reconstruction is found to be $m(B^+) < 5100\,\text{MeV/c}^2$. As the partial reconstruction method does not select π^0 candidates, also the resonant three-body decay $B^+ \to K^+ J/\psi$ can contribute to the $B^+ \to K^{*+} J/\psi$ signal, if the π^0 is not kinematically reconstructed. Performing the full reconstruction on the simulated data sample corresponds to the reconstruction of $m(K^+ J/\psi)$. By limiting the mass of the three - body decay to $m(K^+ J/\psi) < 5100\,\text{MeV/c}^2$, this resonance can be removed.

The variables used for the training and testing are similar to the ones used in the full reconstruction. These include the flight distance, the direction angle, the

---

1 This sample was used to study the efficiency in the previous chapter.
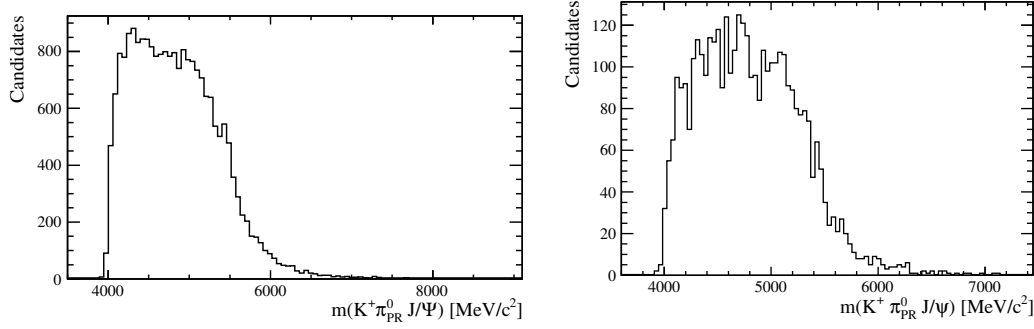2 The distribution only shows a fraction of the data sample.

Figure 33: B^+ invariant mass distribution before (left) and after (right) the application of a BDT cut which was trained on the $m(B^+)$ sideband ($m(B^+) > 5700 \, \text{MeV}/c^2$).

vertex variable $\chi^2_{endvertex}$ and the χ^2 value of the impact parameter. The description of these variables can be found in Chapter 5. Additionally, the kinematically reconstructed momenta of B^+ and π^0 are taken into account. They are denoted by the index "PR". A vertex isolation variable, the B^+- smallest $\Delta\chi^2$ value of one track is used. This variable describes the difference of secondary vertex - χ^2 values when an additional track is added to the decay. In the $B^+ \to K^{*+} \, J/\psi$ decay, for instance, the secondary vertex is formed by three tracks: K^+, μ^+ and μ^-. When an additional track is added, the χ^2 value of the newly reconstructed secondary vertex will be shifted by a value $\Delta\chi^2$. As the $B^+ \to K^{*+} \, J/\psi$ decay does not include an additional track since the π^0 is a neutral particle, the smallest $\Delta\chi^2$ - value of this decay will be slightly smaller than decays which include an additional track, such as $B^+ \to K^* (\to K^+ \, \pi^-) \, J/\psi$.

Figure 8.1 shows a list of the BDT variables used in the training and testing and their separation power. Figure 34 shows distributions of four of the most discriminating input variables used in the BDT training. The distributions of the remaining variables used in the training and testing can be found in Appendix A. The BDT response distribution for the signal and background template are illustrated in Figure 35.

- Transverse momenta of B^+_{PR1} ($\delta = 2.8\%$), B^+_{PR2} ($\delta = 2.5\%$), K^+ ($\delta = 10.5\%$), K^{*+}_{PR1} ($\delta = 10.3\%$), K^{*+}_{PR2} ($\delta = 4.6\%$), π^0_{PR1} ($\delta = 3.3\%$) and π^0_{PR2} ($\delta = 3.1\%$).

- B^+ flight distance ($\delta = 1.1\%$)

- B^+ χ^2_{FD} ($\delta = 1.2\%$)

- B^+ Direction Angle ($\delta = 1.5\%$)

- B^+ $\chi^2_{Endvertex}$ ($\delta = 1.8\%$)

- B^+- χ^2_{IP} ($\delta = 1.6\%$), K^+- χ^2_{IP} ($\delta = 3.7\%$), μ^+- χ^2_{IP} ($\delta = 0.8\%$) and μ^-- χ^2_{IP} ($\delta = 1.0\%$)

- B^+ Smallest $\Delta\chi^2$ of one track ($\delta = 0.3\%$)
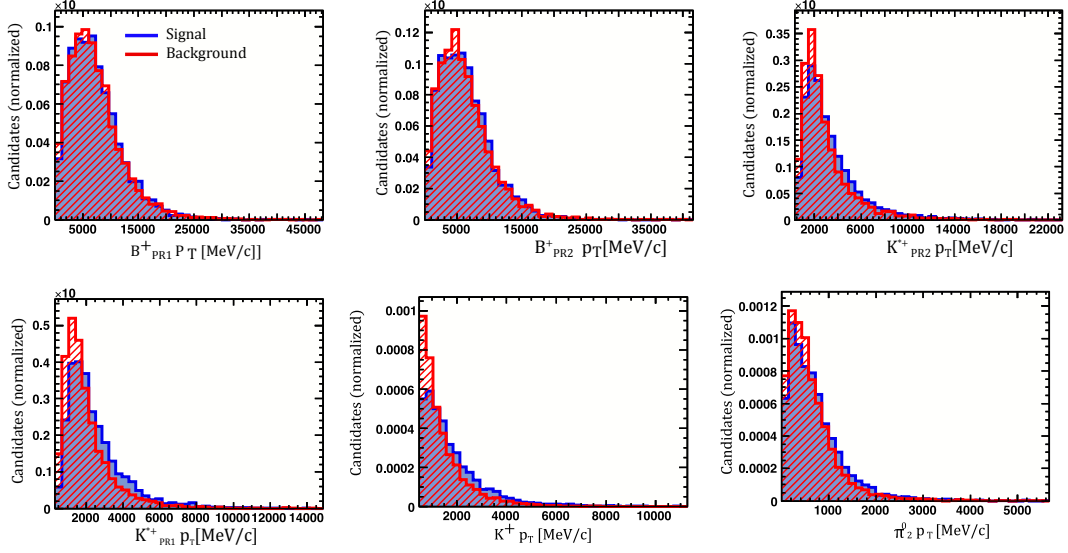
Figure 34: Six input variables used in the BDT training and testing showing signal (blue) background distributions (red). The distributions of the other input variables can be found in Appendix A.

The BDT response cut applied in this part of the analysis is again obtained by maximizing the figure of merit $N_S/\sqrt{N_S + N_B}$. In the full reconstruction the number of signal events N_S is obtained by a fit to the resonant decay channel and the number of background events N_B are determined from the extrapolation of the sideband fit. In the analysis of the partial reconstruction, on the other hand, N_S is obtained by determining the B^+ signal candidates from a simulated signal sample, N_B is obtained from data. The BDT response cut as well as additional cuts on the particle hypothesis of K^+, μ^+ and μ^- are displayed in Table 13.

Variable name	Cut
BDT response	> 0.40
μ^+ PID_μ	> 0
μ^- PID_μ	> 0
K^+ PID_K	> 3
$m(K^+ J/_\psi)$	< 5100

Table 13: This table shows the cuts applied on the invariant B^+ mass distribution. $m(B^+_{FR})$ refers to the full reconstructed B^+ mass of the three-body decay $B^+ \rightarrow K^+ J/\psi$.

8.2 SIMULATED SIGNAL DISTRIBUTION

The simulated signal distribution which is used as the signal template was previously explained in Section 7.4. Figure 36 shows the corresponding B^+ mass spectrum after the application of the BDT response cut and the particle identification cuts from Table 13 as well as the corresponding pull distribution. The pull expresses the deviation of the entries from the fit function in units of the error. In
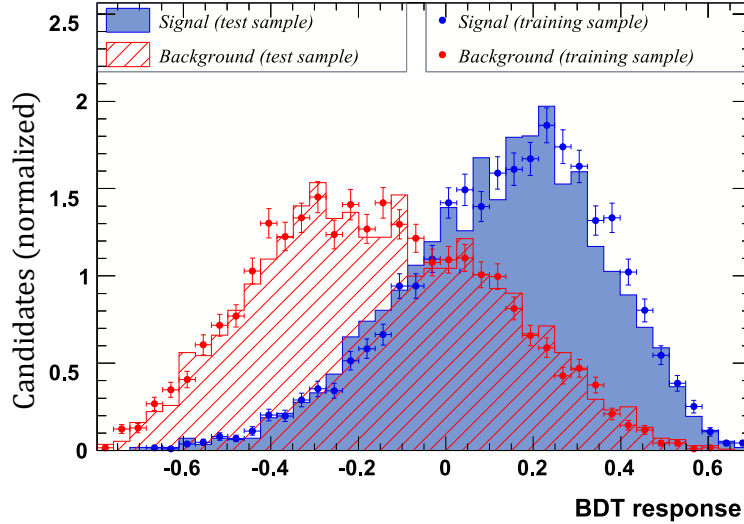
Figure 35: The BDT response distribution for the signal (blue) and the background (red) template.

the following analysis, the solution best of Equation 19 is taken (see Section 7.3). Although a more detailed investigation on the exact signal shape can be performed, the phenomenological model $\mathcal{P}_{\text{tot}} = f_{\text{RBW}}\mathcal{P}_{\text{RBW}} + f_{\text{BiGauss}}\mathcal{P}_{\text{BiGauss}} + f_{\text{Gauss}}\mathcal{P}_{\text{Gauss}}$ sufficiently describes the signal shape for this preliminary analysis. In order to later identify the signal contribution in the real data sample, the fit is again performed by using fractions instead of the absolute number of signal events in each contribution. By doing so, the absolute signal yield can be adjusted while the relative amount the individual components contribute stays the same. The fit results are summarized in Table 14.

Parameter	Fit result
$\text{mean}[\text{MeV}/c^2]$	5281.2 ± 0.9
$\sigma_{\text{RBW}}[\text{MeV}/c^2]$	85.4 ± 2.5
$\sigma_{\text{L}}[\text{MeV}/c^2]$	107.4 ± 2.0
$\sigma_{\text{R}}[\text{MeV}/c^2]$	111.7 ± 2.3
$\sigma_{\text{Gauss}}[\text{MeV}/c^2]$	261.4 ± 4.9
f_{RBW}	0.287 ± 0.012
f_{biGauss}	0.268 ± 0.010
f_{Gauss}	0.555 ± 0.016

Table 14: Fit parameter values for the invariant B^+ mass $m(K^+\pi^0_{\text{PR}}J/\psi)$ from Figure 36.

8.3   APPLICATION TO MEASURED DATA

In a first approach, the partial reconstruction technique which was previously developed on simulated data is applied to real data. Again only a fraction of the measured data is reconstructed with positive solutions for the value of B. As shown in the distribution of B in Figure 37, only $\sim 31.9\%$ of the events have $B \geqslant 0$. Compared
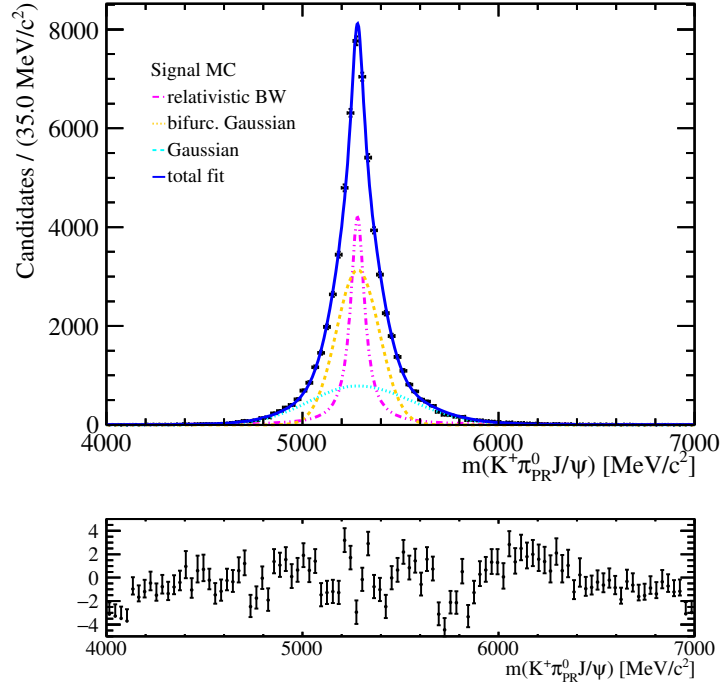
Figure 36: Fit of $m(K^+\pi^0_{PR}J/\psi)$ simulation after application of BDT cuts. The best solution of $m_{1/2}(B^+)$ is chosen analog to Section 7.3. The lower plot shows the pull distribution. The fit results are shown in Table 14.

to $\sim 59.1\%$ which are available in the simulated signal sample, the lower value in this data sample reflects the abundance of background contributions. This value can later be compared to the simulated inclusive sample to check the compatibility of background elimination in both cases since background events will often correspond to a negative B.
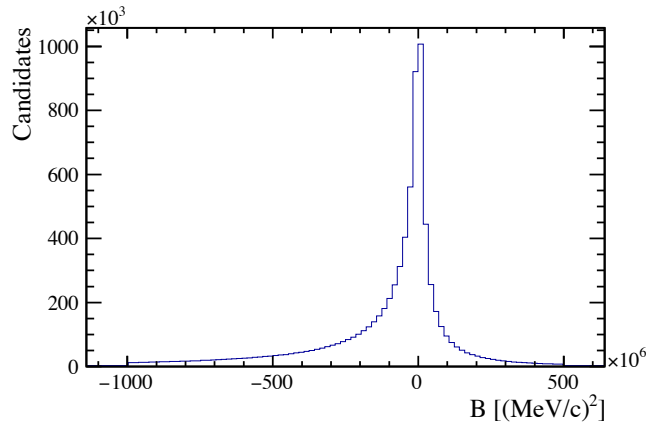
Figure 37: The distribution of term B showing negative and positive values. A fraction of $\sim 31.9\%$ of the events have $B \geqslant 0$.

As pointed pout previously in the study of the B^+ mass resolution, the π^0 mass as well as the K^{*+} mass are set to their nominal PDG masses in the kinematic reconstruction of the π^0. Therefore it does not make any sense to show the corresponding mass distributions as it was done in the full reconstruction of the B^+.

Figure 38 shows the distributions of the two invariant B^+ mass solutions before the application of any cuts. The multivariate analysis which was performed in the previous section is now applied to data with the aim of suppressing the background. Figure 39 shows the B^+ mass distributions after the application of the BDT response and the particle hypothesis cuts. The signal shape which was previously obtained from a simulated signal sample is fitted to this distribution. The fractions of the individual model contributions are fixed and the number of events is normalized to the number of events in the data sample. Although the BDT eliminates a large fraction of background when compared to Figure 38, there is still a clear "shoulder" structure at lower masses. The residual distribution of the B^+ mass spectrum visualizes the shape of this structure. As the signal-like part of the B^+ mass distribution has a shape which is very similar to the signal shape obtained from simulation, it can misleadingly be identified as the real signal contribution of the $B^+ \rightarrow K^{*+} J/\psi$ decay, while the shoulder can be spuriously categorized as background. Although the signal shape is indeed comparable to the signal shape from simulation, the content of this peak does not only stem from the desired $B^+ \rightarrow K^{*+} J/\psi$ decays as it is shown in the next section.
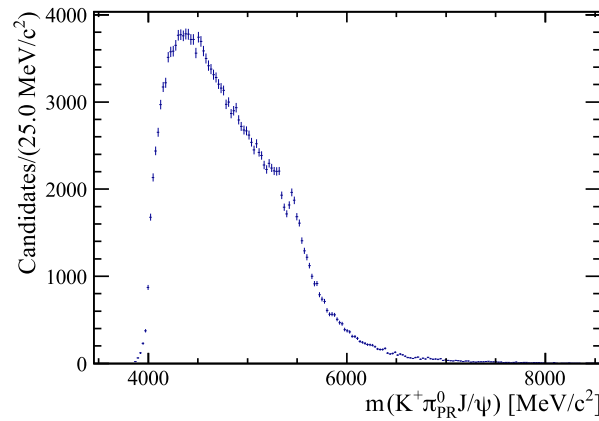
Figure 38: The B^+ invariant mass distribution from data without cuts.
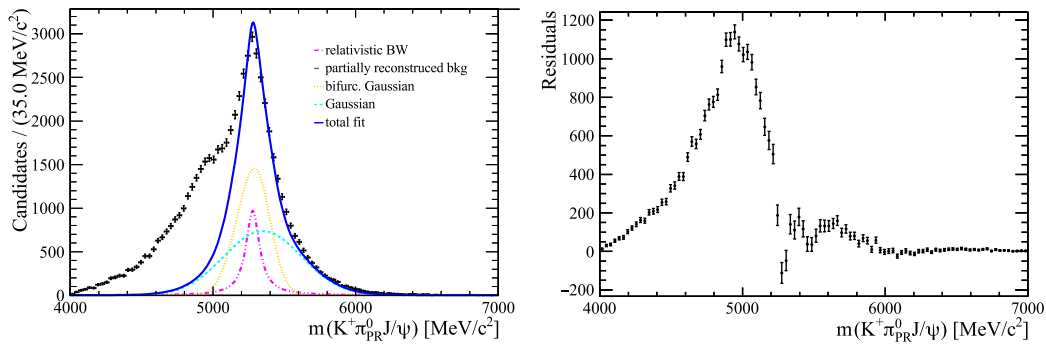
Figure 39: Left: B^+ mass spectrum with the signal shape from simulation. Right: Residual distribution.

8.4 APPLICATION TO SIMULATED DATA SAMPLE WITH INCLUSIVE DECAYS

As is it not trivial which background sources mimic the signal and which ones can be separated easily from the signal region, a study on a simulated data sample, which approximately reflects the content of backgrounds in measured data, is crucial. A simulated *inclusive* $B \rightarrow J/\psi$ sample is therefore used which includes all charmonium decays of B mesons. The relative branching fractions are taken from [1]. The inclusive sample is used as a reference sample in order to understand the contamination from other decays which influence the B^+ invariant mass distribution to a greater degree.

Again only a fraction of the simulated data sample is reconstructed with positive solutions for the value of B. As shown in the distribution of B in Figure 40, only $\sim 32.2\%$ of the events have $B \geqslant 0.$ compared to $\sim 31.9\%$ in the data sample As background tend to correspond to a negative B, this reaffirms the resemblance of the inclusive MC sample and the data sample considering the backgrounds.
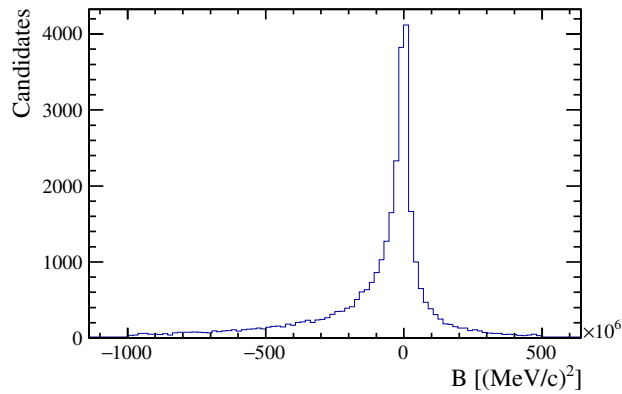
Figure 40: The distribution of term B showing negative and positive values. A fraction of $\sim 32.2\%$ of the events have $B \geqslant 0$.

8.4.1 *Expected background sources*

Ideally, a multivariate selection combined with PID cuts eliminate backgrounds to allow a separation of the signal and background shapes. In the case of the full reconstruction in Chapter 6, this was easily feasible, since the combinatorial background followed an exponential distribution, distinguishing its shape from the Gaussian signal distribution. In the partial reconstruction, this is not as straightforward. Since one of the decay products is partially reconstructed, this allows other resonant decays to mimic the $B^+ \rightarrow K^{*+} J/\psi$ decay such as $B^0 \rightarrow K^* (\rightarrow K^+ \pi^-)$, where the partially reconstructed particle is a π^-. The simulated inclusive sample allows for the study of background contributions which mimic the typical signature of the B^+ decay. In a detailed analysis, the background contributions require a quantitative treatment in the sense of modeling each individual

contribution. In the scope of this preliminary analysis, the study of background contributions merely demonstrates the importance of considerable background sources as well as their origin. The following gives a list of different categories for the relevant background contributions. A summary of the individual contributions with corresponding branching fractions can be found in Table 15. The first column describes the decay which is misidentified as a $B^+ \rightarrow K^{*+} J/\psi$ decay. The third column shows which particles are misidentified and consequently lead to the wrong decay.

PURE COMBINATORICS

Analogous to the selection of fully reconstructed events, combinatorial background from $b\bar{b}$ decays is present (see Chapter 5) when the B^+ candidate is made by three randomly associated tracks. As mentioned before, this background features different kinematic properties which allow a statistical separation from the signal which is achieved by the multivariate analysis.

MISIDENTIFIED KAONS

In proton-proton collisions, a large amount of charged pions is produced as they are the lightest existing mesons. A charged pion can be misidentified as a K^+, mimicking the $B^+ \rightarrow K^{*+} J/\psi$ decay. Also random muons, prompt kaons or protons can be misidentified as a K^+.

OTHER PARTIALLY RECONSTRUCTED DECAYS

As there are no restrictions on the missing particle which is kinematically reconstructed, other particles can be reconstructed and incorrectly identified as kinematically reconstructed π^0. When the partially reconstructed particle is not the neutral pion but a kaon or a charged pion, peaking backgrounds from other decays to multi-body final states are created. Their branching fractions are generally large and they have a similar kinematic signature as the desired decay. The decay $B^0 \rightarrow K^* (\rightarrow K^+ \pi^-) J/\psi (\rightarrow \mu^+ \mu^-)$ is an example for another partially reconstructed decay, when the charged pion is partially reconstructed. The invariant mass of the four daughter particles then peaks in the B^+ mass region.

NON-RESONANT CONTRIBUTIONS

In addition to the reconstruction of other resonant decays, non-resonant contributions arise when no particle is kinematically reconstructed. The decay $B^+ \rightarrow K^+ J/\psi$ for instance has a branching fraction which is in the same order of magnitude

Channel	Branching ratio	Contribution
$B^0 \to K^* (\to K^+ \pi^-) J/\psi$	$(1.32 \pm 0.06) \times 10^{-3}$	$\pi^- \leftrightarrow \pi^0$
$B^0 \to K(1270)^0 J/\psi$	$(1.3 \pm 0.5) \times 10^{-3}$	K^+ from higher resonance
$B^0 \to K^* (\to K^+ \pi^-) \chi_{c1}$	$(2.42 \pm 0.21) \times 10^{-4}$	$\pi^- \leftrightarrow \pi^0$ and J/ψ from χ_{c1}
$B^0 \to K^* (\to K^+ \pi^-) \chi_{c2}$	$(1.7 \pm 0.4) \times 10^{-4}$	$\pi^- \leftrightarrow \pi^0$ and J/ψ from χ_{c2}
$B^0 \to K^* (\to K^+ \pi^-) \psi(2S)$	$(6.0 \pm 0.4) \times 10^{-4}$	$\pi^- \leftrightarrow \pi^0$ and J/ψ from $\psi(2S)$
$B^0 \to K^+ \pi^- J/\psi$	$(1.2 \pm 0.6) \times 10^{-3}$	$\pi^- \leftrightarrow \pi^0$
$B^0 \to \pi^+ \pi^- K^0 J/\psi$	$(1.0 \pm 0.4) \times 10^{-3}$	$\pi^+ \leftrightarrow K^+$, $\pi^- \leftrightarrow \pi^0$ K^0 not reconstructed
$B^0 \to K^+ \pi^- \psi(2S)$	$(5.8 \pm 0.4) \times 10^{-4}$	$\pi^- \to \pi^0$ and J/ψ from $\psi(2S)$
$B^0_s \to \phi(\to K^+ K^-) J/\psi$	$(1.07 \pm 0.09) \times 10^{-3}$	$K^- \leftrightarrow \pi^0$
$B^0_s \to \phi(\to K^+ K^-) \psi(2S)$	$(5.4 \pm 0.6) \times 10^{-4}$	$K^- \leftrightarrow \pi^0$ and J/ψ from $\psi(2S)$
$B^0_s \to K^+ K^- J/\psi$	$(2.49 \pm 0.17) \times 10^{-5}$	$K^+ \leftrightarrow \pi^0$
$B^+ \to K_1(1270)^+ J/\psi$	$(1.8 \pm 0.5) \times 10^{-3}$	K^+ from higher kaon resonance
$B^+ \to K_1(1400)^+ J/\psi$	$< 5.0 \times 10^{-4}$	K^+ from higher kaon resonance
$B^+ \to K^{*+} \chi_{c2}$	$< 1.2 \times 10^{-4}$	J/ψ from χ_{c2}
$B^+ \to K^{*+} \chi_{c1}$	$(3.0 \pm 0.6) \times 10^{-4}$	J/ψ from χ_{c1}
$B^+ \to K^{*+} \chi_{c0}$	$< 2.1 \times 10^{-4}$	J/ψ from χ_{c0}
$B^+ \to K^{*+} \psi(2S)$	$(6.7 \pm 1.4) \times 10^{-4}$	J/ψ from $\psi(2S)$
$B^+ \to K^+ \chi_{c2}$	$(1.1 \pm 0.4) \times 10^{-5}$	J/ψ from χ_{c2} and π^0 not reconstructed
$B^+ \to K^+ \chi_{c1}$	$(4.79 \pm 0.23) \times 10^{-4}$	J/ψ from χ_{c1} and π^0 not reconstructed
$B^+ \to K^+ \chi_{c0}$	$(1.50^{+0.15}_{-0.14}) \times 10^{-4}$	J/ψ from χ_{c0} and π^0 not reconstructed
$B^+ \to K^+ \psi(2S)$	$(6.27 \pm 0.24) \times 10^{-4}$	J/ψ from $\psi(2S)$ and π^0 not reconstructed
$B^+ \to K^+ \psi(3770)$	$(4.9 \pm 1.3) \times 10^{-4}$	J/ψ from $\psi(3770)$ and π^0 not reconstructed

Table 15: Resonant and non-resonant background contributions to B^+. Reported branching ratios are taken from Ref. [1].

as the $B^+ \to K^{*+} J/\psi$ decay. Also B^0 and B^0_s decays provide backgrounds from non-resonant contributions.

B DECAYS WITH DIFFERENT RESONANCES

Another type of potential background are decays where the J/ψ originates from another resonance. An example for this type of background is $B^+ \to \chi_{c1}(P)(\to J/\psi (\to \mu^+ \mu^-) \gamma) K^{*+}$. The photon is not detected in this decay and therefore the reconstructed B^+ mass will be slightly shifted toward lower masses as a fraction of its four momentum is carried away by the photon. These backgrounds are omitted in the analysis of the non-resonant decay $B^+ \to K^{*+} \mu^+ \mu^-$.

Additionally, B^+ or B^0 decays to other intermediate resonances which have similar decay products can contribute. This can include the B^+ or B^0 decay to higher K^+ states such as $K_1(1270)^0$ or $K_1(1270)^+$. For instance, $K_1(1270)^0$ can decay to $K^{*+} \pi^0$. When the additional π^0 is not reconstructed, this mimics the $B^+ \to K^{*+} J/\psi$ decay. The B^+ mass distribution is then shifted to lower masses.

8.4.2 *Background contamination*

Figure 41 shows the B^+ mass spectrum obtained from the inclusive J/ψ sample before the application of cuts. Although the number of simulated events is signif-

icantly smaller in this sample, causing a larger statistical uncertainty, the resemblance of real data is clearly given when compared to Figure 38. In the following, the various types of background contributions are categorized according to the list stated above. The BDT response cut and particle hypothesis cuts from Table 13 are applied to all distributions. Additionally, a cut on the pseudorapidity $\eta > 2$ is applied to ensure that the tracks of the decay products lie in the acceptance of the detector which is $2 < \eta < 5$. Although the selections eliminate a large fraction of background contamination, they also remove signal events whereas peaking backgrounds remain:
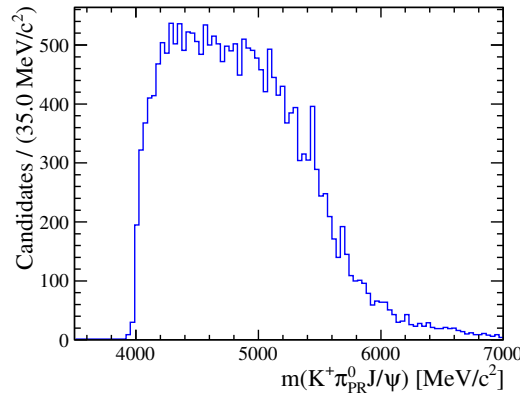
Figure 41: The B^+ mass spectrum obtained from the inclusive sample without any cuts.

Figure 42 (left) shows the background contributions where J/ψ originates in another resonance such as χ_{c1}, χ_{c2} and $\psi(2S)$. As the photon is not detected in this decay, the reconstructed B^+ mass is slightly shifted toward lower masses. As only a small fraction of its four momentum is carried away by the photon, this background still peaks in the signal region and cannot be disentangled in the resonant $B^+ \to K^{*+} J/\psi$ decay.

Also decays where the K^+ meson stems from higher kaon resonances create a non-negligible background source as depicted in Figure 42 (right). For instance, the $K_1(1270)^+$ meson can decay into pairs of $(K\,\rho)$ $(42 \pm 6)\%$ or $(K^* (892)\pi)$ $(16 \pm 5)\%$ [1]. The kinematically reconstructed mass will therefore be smaller than the $B^+ \to K^{*+} \pi^0$ mass as there are additional particles in the final state which carry away a fraction of the momentum. In the full reconstruction of the $B^+ \to K^{*+} J/\psi$ decay, this background is also present when the additional pions or kaons are not reconstructed, though this background is eliminated to a high degree by applying a cut on the mass window of the K^{*+} resonance, which removes the higher resonances. In the partial reconstruction, on the other hand, it is not possible to constrain the K^{*+} in this way, since the K^{*+} mass is set to its nominal mass. Therefore, this background contribution must be modeled and thereby separated from the signal shape.

The non-resonant contributions are plotted in Figure 43 (left). Among others, these include the non-resonant $B^+ \to K^+ \pi^0 J/\psi$ decay as well as the non-resonant B^0
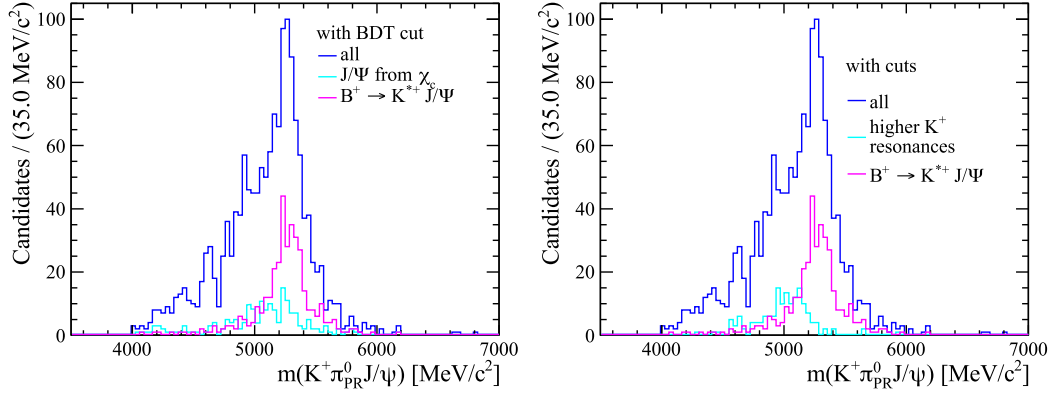
Figure 42: Left: Background contributions where the J/ψ meson stems from charmonium decays (cyan). Right: The K^+ meson originates in higher kaon resonances (cyan) instead of the K^{*+} resonance. The signal distribution (magenta) and the entire sample (blue) is shown.

and B_s^0 contributions which also decay into a K^+ plus a missing particle, denoted as $B \to K^+ X J/\psi$. The shape of this background category is slightly shifted to lower masses, though a non-negligible amount is present in the signal region. As there is a discrepancy in the shape of this background compared to the signal shape, the background shape can be modeled and separated from the signal.

Finally, Figure 43 (right) shows the contributions of partially reconstructed decays where a wrong particle is kinematically reconstructed. These resonances peak in the signal region and stem from the resonant decays $B^0 \to K^* J/\psi$ and $B_s^0 \to \Phi J/\psi$. Their contributions are comparable to the magnitude of the signal decays. As there is no restriction on the missing particle, they cannot be kinematically disentangled from the signal since their three-body decay topology is identical to the $B^+ \to K^{*+} J/\psi$ decay. In data, they will add to the measured signal yield and cannot be separated from the signal. This can again be seen in Figure 39. The signal-like part has a similar distribution as the signal shape from simulation since the $B^0 \to K^*$ J/ψ and $B_s^0 \to \Phi J/\psi$ resonances peak in the signal region. Therefore the sum of the mass distribution from $B^+ \to K^{*+} J/\psi$ decays and the mass distributions from the resonances $B^0 \to K^* J/\psi$ and $B_s^0 \to \Phi J/\psi$ can be mistaken for signal. The actual signal contribution is smaller and thus cannot be separated from the peaking background.
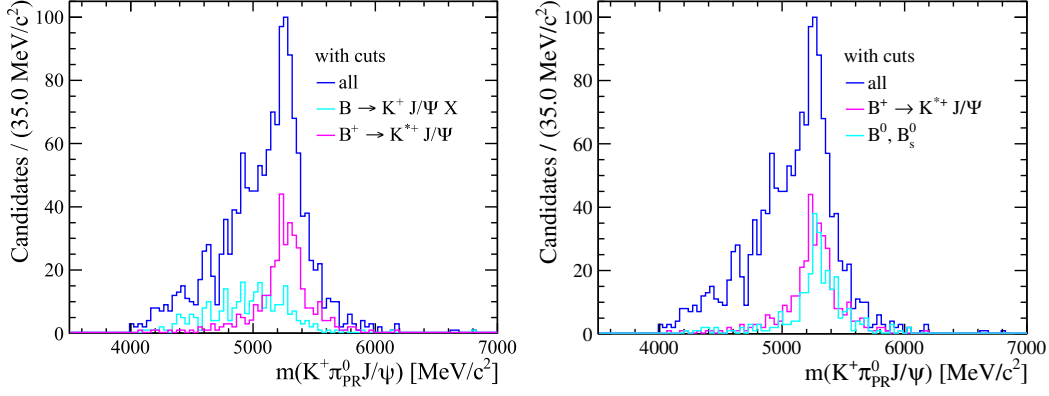
Figure 43: Left: S-wave contributions (cyan). Right: Peaking background contributions of partially reconstructed decays where a wrong particle is kinematically reconstructed (cyan). The signal distribution (magenta) and the entire sample (blue) is shown in both cases.
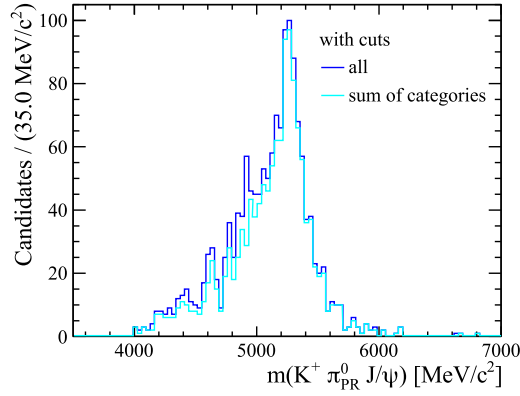
Figure 44: The sum of all background categories from Figure 42 and Figure 43 (cyan) after cuts. The entire sample (blue) is shown as well. The small difference arises from combinatorics and misidentified kaons or muons.

8.4.3 Conclusion

The analysis of the inclusive J/ψ simulation has shown that a large amount of background contamination is present in the spectrum of partially reconstructed B^+ decays. The background contamination can be categorized into four different contributions:

- The J/ψ meson stems from charmonium decays.

- The K^+ meson originates in higher kaon resonances (cyan) instead of the K^{*+} resonance.

- Non-resonant contributions.

- Peaking background contributions of partially reconstructed decays where a wrong particle is kinematically reconstructed.

The background from charmonium decays is not present in the non-resonant $B^+ \rightarrow K^{*+} \mu^+ \mu^-$ decay channel and therefore can be neglected. Higher kaon resonances and non-resonant contributions on the other hand, significantly contribute to the yield as they overlap with the signal region. In contrast to the full reconstruction, the kaon resonances cannot be eliminated by a constraint on the K^{*+} mass window, as the K^{*+} mass is set to its nonimal PDG value in the kinematic reconstruction procedure. In order to extract these decays from the signal decay, their shapes need to be modeled. The peaking background contributions of the partially reconstructed decays $B^0 \rightarrow K^* J/\psi$ and $B_s^0 \rightarrow \phi J/\psi$ cannot be separated from the signal contributions as easily. Common separating variables used in this analysis such as track and vertex isolation, kinematic variables or variables which include the flight direction of the decaying particle, have a low separation power, as these variables have similar distributions for signal and background candidates. Therefore, cuts on these variables also decrease the signal yield. For instance, several B^+ vertex isolation variables in the multivariate analysis, such as $B^+ \chi^2_{Endvertex}$ or the smallest $\Delta\chi^2$ value when adding one track, have a very small separation power. This can be explained by the fact that the B^+ decay vertex is reconstructed by using the tracks of the charged particles K^+, μ^+ and μ^-. Since these particles are also final state particles of B_s^0 and B^0, for instance, their decay vertices are easily mistaken for the $B^+ \rightarrow K^{*+}$ decay vertex. Therefore, the discrimination of the resonances B_s^0 and B^0 is difficult when the mentioned vertex isolation variables of the B^+ are used. In a further analysis, additional variables can be inspected to find quantities which discriminate well between signal and peaking backgrounds. The scope of this thesis did not allow for a further detailed analysis of such well-separating variables. Nevertheless, possible variables which have better separations are variables which use information on the π^0. A possible variable to study is the track separation relative to the direction of the kinematically reconstructed π^0 momentum p_{π^0}. A conus of certain size is applied around p_{π^0} and it is required that no tracks are found in the conus. In this manner, it can be assured that the kinematically reconstructed particle is a π^0. If the kinematically reconstructed particle was a charged particle, such as a π^-, on the other hand, a track of this particle would be visible in the conus. Further, information of the energy deposits originating from the two photons from the π^0 decay in the electromagnetic calorimeter can also possibly be used to ensure that the reconstructed particle is a π^0.

SUMMARY AND OUTLOOK

This analysis covers two approaches for the reconstruction of the electroweak penguin decay $B^+ \to K^{*+} (\to K^+ \pi^0) \mu^+ \mu^-$:

In the first approach a full reconstruction of the final state particles was performed on a data sample taken at the LHC in 2011 and 2012 with center of mass energies of $\sqrt{s} = 7\,\text{TeV}$ and $\sqrt{s} = 8\,\text{TeV}$, respectively. The total integrated luminosity of these measurements is approximately $3\,\text{fb}^{-1}$. The full reconstruction results in a $B^+ \to K^{*+} \mu^+ \mu^-$ signal yield of $N_S = 65 \pm 21$ events with a statistical significance of 3.23σ. From this, the relative branching fraction of $B^+ \to K^{*+} \mu^+ \mu^-$ decays relative to $B^+ \to K^{*+} J/\psi$ decays was determined:

$$\frac{\mathcal{B}(B^+ \to K^{*+} \mu\mu)}{\mathcal{B}(B^+ \to K^{*+} J/\psi (\to \mu\mu))} = (0.12 \pm 0.4(\text{stat.})) \times 10^{-4}.$$

With the knowledge of the branching fraction of the reference channel $B^+ \to K^{*+} J/\psi$ and the fraction of J/ψ decays to a dimuon pair $\mathcal{B}(J/\psi \to \mu\mu)$, the absolute branching fraction of $B^+ \to K^{*+} \mu\mu$ was be determined [1]:

$$\mathcal{B}(B^+ \to K^{*+} \mu\mu) = (1.02 \pm 0.33(\text{stat.})) \times 10^{-6}.$$

The low reconstruction efficiency of the neutral pion leads to a large statistical uncertainty of approximately 32.5%. This branching fraction is in agreement with other measurements from LHCb [10]. Due to the large statistical uncertainties and the scope of this thesis, no attempt to estimate a systematic uncertainty was done, though a qualitativee discussion of systematic uncertainties was given.

Motivated by the possible gain of a higher signal significance, the feasibility of a new technique was exploited in which the neutral pion is reconstructed by decay kinematics. The mathematical algorithm which is used to kinematically reconstruct the π^0 momentum was explained. In this technique, the π^0 momentum is calculated by using the B^+ flight direction constraining the masses of K^+, π^0 and K^{*+} to their nominal PDG masses. The π^0 momentum results in two solutions $p_{\pi^0}^{\parallel} = A \pm \sqrt{B}$, where A and B depend on the kinematical variables of the daughter particles K^+, μ^+ and μ^-. Studies on simulated data have shown that the reconstructed vertices degrade the resolution of the invariant B^+ mass more than the reconstructed momenta. The choice of the solution of $m(B^+)_{1/2}$ significantly effects the mass resolution. By choosing the best solution, which is the solution that is closest to the nominal B^+ mass, the best resolution can be achieved. To compare the performance of the partial reconstruction with the full reconstruction, the efficiency of partially reconstructed $B^+ \to K^{*+} J/\psi$ decays is compared to the corresponding efficiency in the full reconstruction of $B^+ \to K^{*+} J/\psi$. Ad-

ditionally, the resolution of the corresponding B^+ mass distributions is compared in the partial and full reconstruction. It was shown that the relative efficiency $\epsilon = \frac{\epsilon^{PR}}{\epsilon^{FR}} = 2.08 \pm 0.01$. Considering that systematic uncertainties are not taken into account and no restrictions are applied to the π^0 in both cases, this preliminary estimation still shows that the efficiency of partially reconstructing $B^+ \rightarrow K^{*+} J/\psi$ decays is significantly larger than the full reconstruction of $B^+ \rightarrow K^{*+} J/\psi$ decays while the resolution of the invariant B^+ mass is only slightly degraded. Therefore, the application of the partial reconstruction method to measured data is a useful approach in reconstructing $B^+ \rightarrow K^{*+} J/\psi$ decays.

In the scope of this analysis a tool was created which allows to create nTuples before implementing pre-selection cuts. This makes it possible to apply the partial reconstruction technique to other decay channels as well.

The partial reconstruction technique was further applied to real data and a multivariate analysis was performed to remove background contamination. The data sample used in this part corresponded to a total integrated luminosity of $1\,\text{fb}^{-1}$. A simulated data sample which reflects measured data enables the study of background contributions. Several peaking backgrounds mimic the signal distribution. These backgrounds cannot be separated from the signal events by the use of common discriminating variables. Reconstructing the B^+ from decay kinematics therefore is not feasible in a straightforward way as the background contributions are highly entangled with the signal.

While this first preliminary study determined the relative efficiency of reconstructing $B^+ \rightarrow K^{*+} J/\psi$ decays, in a further analysis, the reconstruction efficiency of the kinematically reconstructed π^0 can be determined absolutely. This can be done to have direct comparison to the efficiency of π^0 reconstructed in the detector and to establish a more precise statement on how well the partial reconstruction method works.

To reduce the backgrounds which occur from kinematically reconstructing the B^+ mass to measured data, additional variables which separate signal and background better must be found. Possible additional variables use different properties of π^0 such as track separation or information on the energy deposits in ECAL which come from the $\pi^0 \rightarrow \gamma\gamma$ decay. Given the significantly larger reconstruction effciency of partially reconstructed $B^+ \rightarrow K^{*+} J/\psi$ decays compared to the full reconstruction, the partial reconstruction has the potential to serve as an alternative approach in the reconstruction of $B^+ \rightarrow K^{*+} J/\psi$ when backgrounds can be separated from the signal.

A

DISTRIBUTIONS OF BDT INPUT VARIABLES

This chapter shows the distributions of all input variables used in the multivariate analysis. It is divided into three sections: Input variables of full reconstruction Chapter 5, those variables for the multivariate analysis of the inclusive J/ψ sample Section 8.4 and those for the application to data Section 8.3.

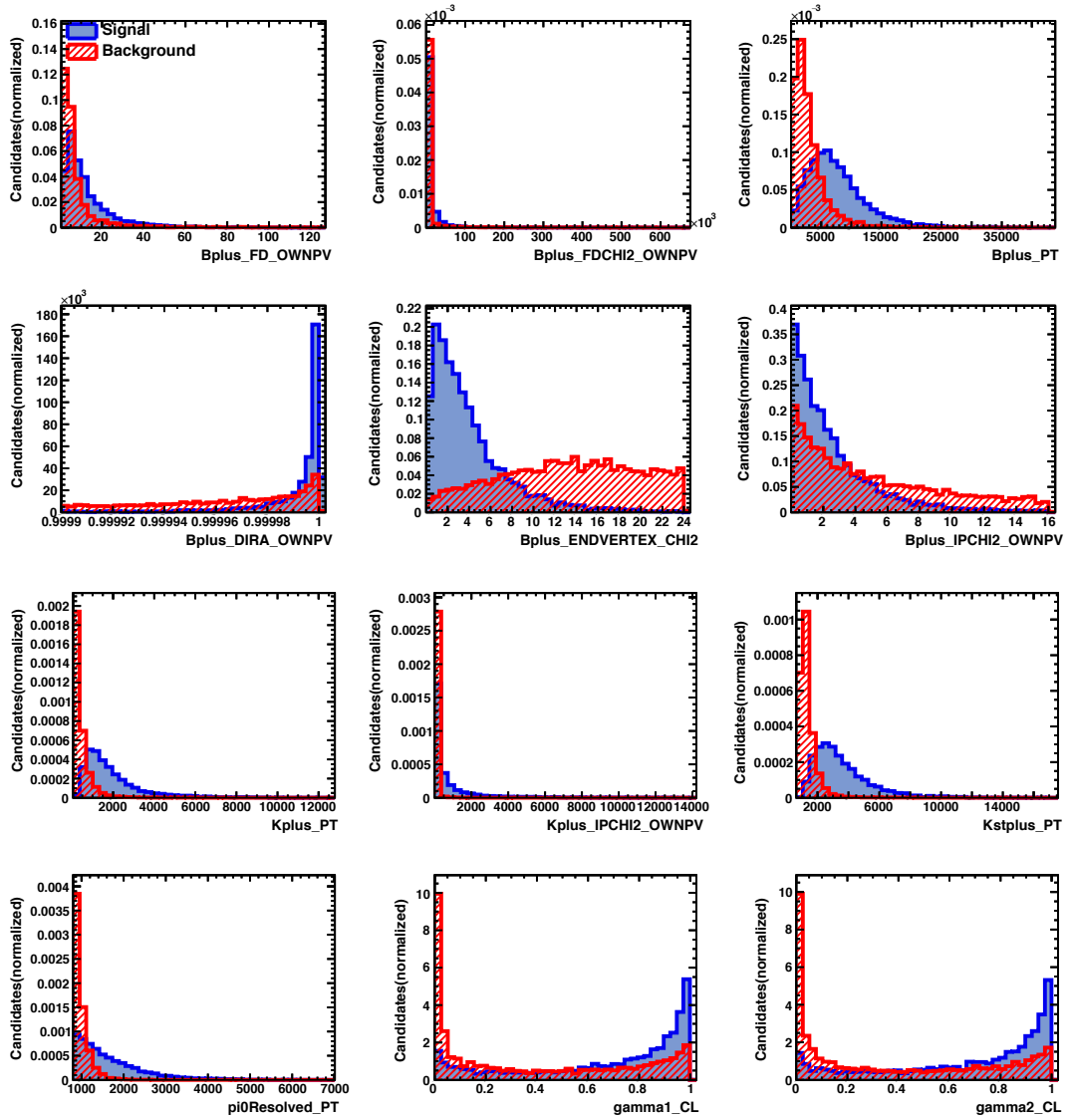### A.1 INPUT VARIABLES FOR FULLY RECONSTRUCTED $B^+ \to K^{*+} \mu^+ \mu^-$

Figure 45: The distribution of the input variables for the Signal (blue) and background (red) template.
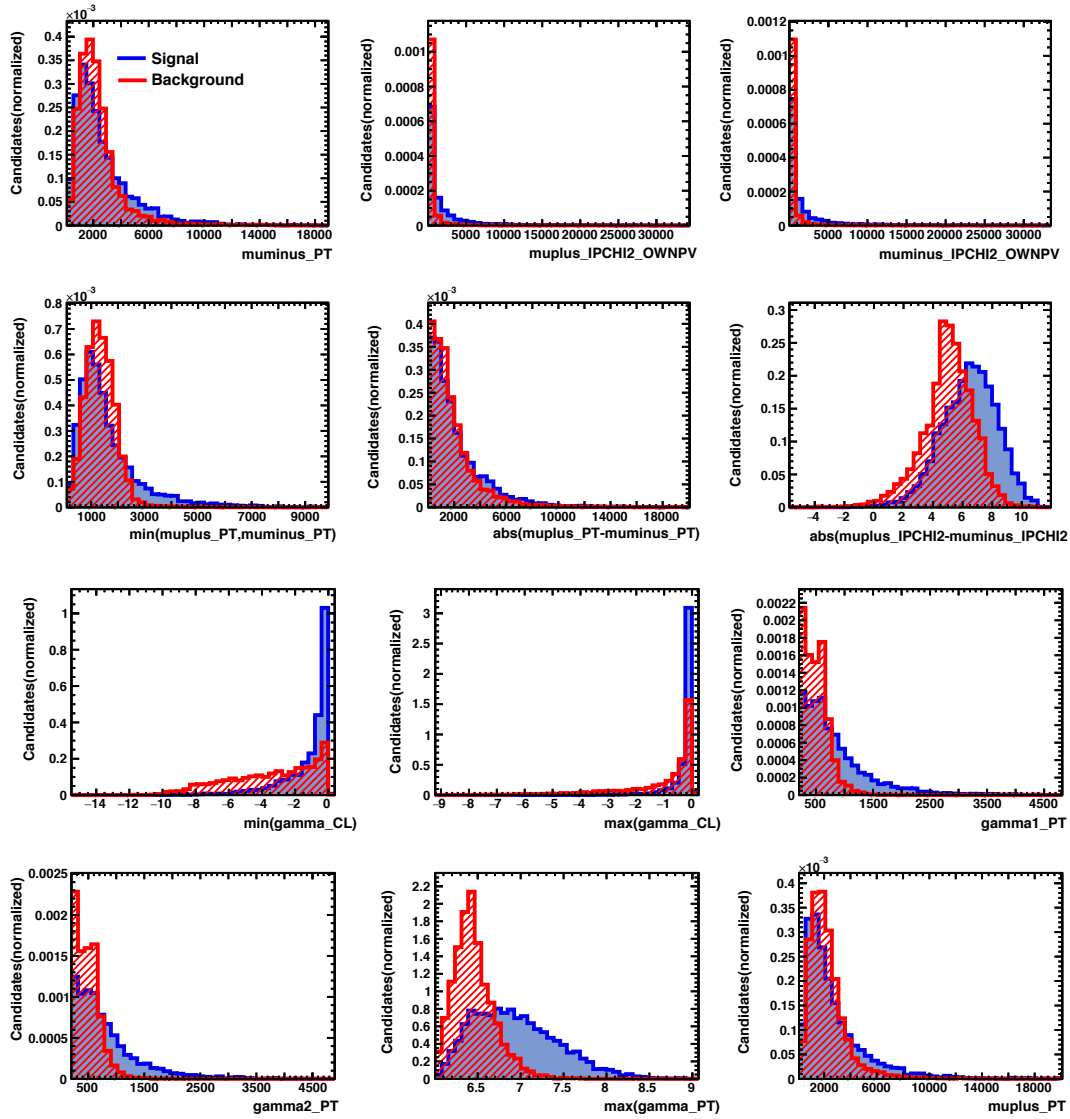
Figure 46: The distribution of the input variables for the Signal (blue) and background (red) template.

A.2 INPUT VARIABLES FOR KINEMATICALLY RECONSTRUCTED $B^+ \to K^{*+}$ J/ψ
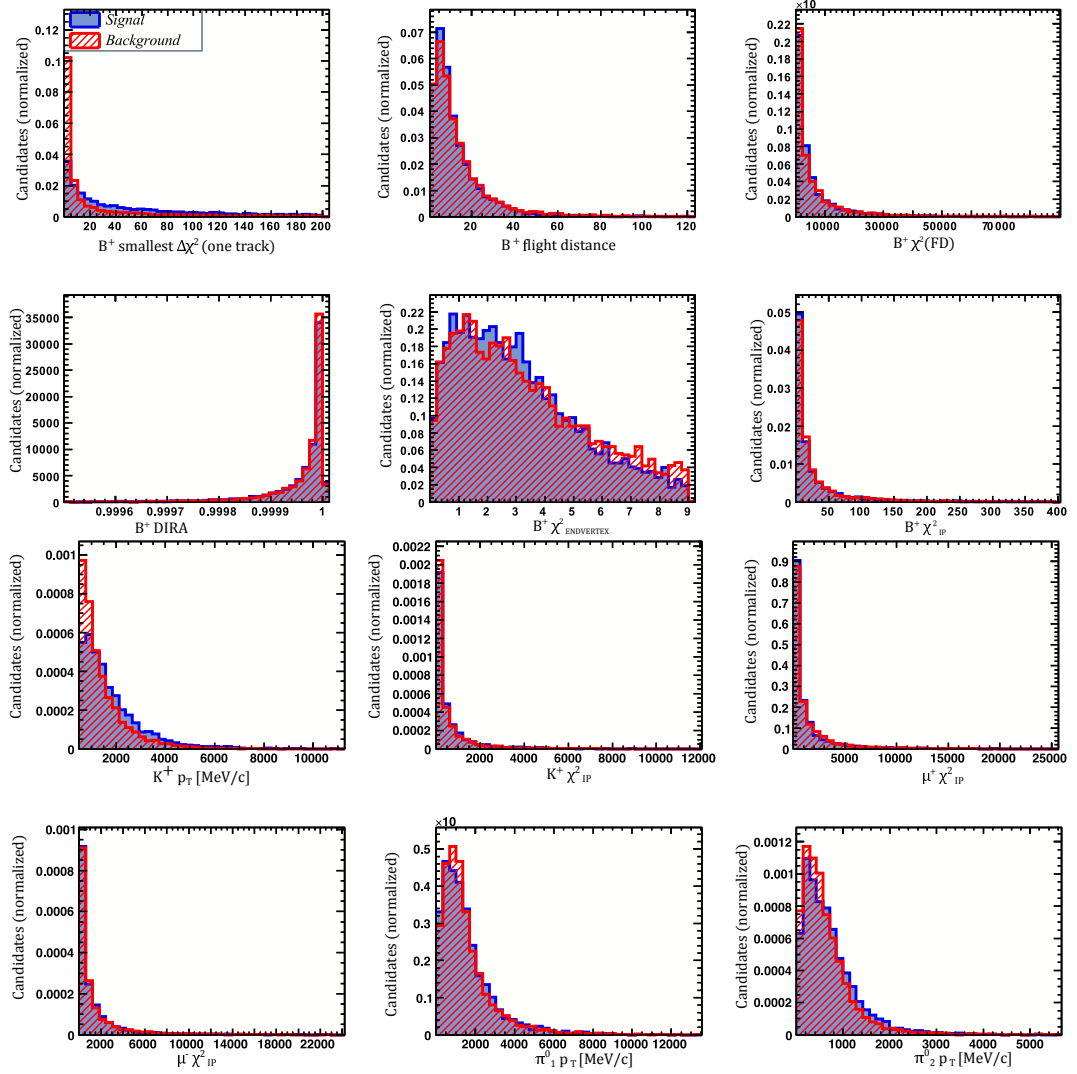
Figure 47: The distribution of the input variables for the Signal (blue) and background (red) template.
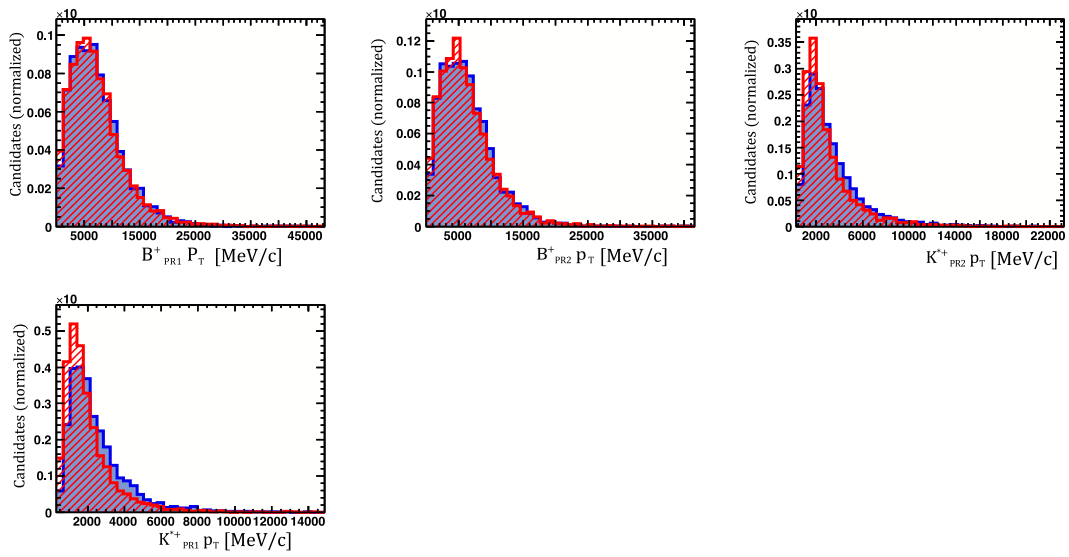
Figure 48: The distribution of the input variables for the Signal (blue) and background (red) template.

ACKNOWLEDGMENTS

[1] K.A. Olive et al. Review of particle physics. *Chin.Phys.*, C38:090001, 2014. doi: 10.1088/1674-1137/38/9/090001.

[2] Stephen Playfer and Sheldon Stone. Rare b decays. *Int.J.Mod.Phys.*, A10:4107–4138, 1995. doi: 10.1142/S0217751X9500190X.

[3] R. Aaij et al. Measurement of $\sigma(pp \to b\bar{b}X)$ at $\sqrt{s} = 7$ TeV in the forward region. *Phys.Lett.*, B694:209–216, 2010. doi: 10.1016/j.physletb.2010.10.010.

[4] A. Straessner. *Electroweak Physics at LEP and LHC*. Springer tracts in modern physics. Springer, 2010. ISBN 9783642052132. URL http://books.google.de/books?id=_ilkmPHp48YC.

[5] Roel Aaij et al. LHCb Detector Performance. *Int.J.Mod.Phys.*, A30(07):1530022, 2015. doi: 10.1142/S0217751X15300227.

[6] http://upload.wikimedia.org/wikipedia/commons/0/00/Standard Model of Elementary Particles.svg.

[7] J. Beringer et al. Review of particle physics. *Phys. Rev. D*, 86:010001, 2012.

[8] Karen Lingel, Tomasz Skwarnicki, and James G. Smith. Penguin decays of B mesons. *Ann.Rev.Nucl.Part.Sci.*, 48:253–306, 1998. doi: 10.1146/annurev.nucl.48.1.253.

[9] Hitoshi Murayama. Supersymmetry phenomenology. pages 296–335, 2000.

[10] R Aaij et al. Measurement of the isospin asymmetry in $B \to K^{(*)}\mu^+\mu^-$ decays. *JHEP*, 1207:133, 2012. doi: 10.1007/JHEP07(2012)133.

[11] Bernard Aubert et al. Direct CP, Lepton Flavor and Isospin Asymmetries in the Decays $B \to K^{(*)}\ell^+\ell^-$. *Phys.Rev.Lett.*, 102:091803, 2009. doi: 10.1103/PhysRevLett.102.091803.

[12] Christoph Bobeth, Gudrun Hiller, and Giorgi Piranishvili. CP Asymmetries in bar $B \to \bar{K}^*(\to \bar{K}\pi)\ell\ell$ and Untagged $\bar{B}_s$, $B_s \to \phi(\to K^+K^-)\ell\ell$ Decays at NLO. *JHEP*, 0807:106, 2008. doi: 10.1088/1126-6708/2008/07/106.

[13] Ian C Brock and Thomas Schorner-Sadenius. *Physics at the terascale*. Wiley, Weinheim, 2011. URL https://cds.cern.ch/record/1354959.

[14] Donald Hill Perkins. *Introduction to high-energy physics; 4th ed*. Cambridge Univ. Press, Cambridge, 2000. URL https://cds.cern.ch/record/396126.

[15] R. Aaij et al. Differential branching fractions and isospin asymmetries of $B \to K^{(*)}\mu^+\mu^-$ decays. *JHEP*, 1406:133, 2014. doi: 10.1007/JHEP06(2014)133.

[16] Y. Amhis et al. Averages of B-Hadron, C-Hadron, and tau-lepton properties as of early 2012. 2012.

[17] E. Norrbin and T. Sjostrand. Production and hadronization of heavy quarks. *Eur.Phys.J.*, C17:137–161, 2000. doi: 10.1007/s100520000460.

[18] PhD thesis.

[19] C. Elsasser (Universität Zürich). Feynman Diagram Library (FDL). URL http://www.physik.uzh.ch/~che/FeynDiag/index.php.

[20] LHCb Speakers' Bureau. URL http://lhcb.web.cern.ch/lhcb/speakersbureau/excel/default.html.

[21] C. Lefèvre. The CERN accelerator complex. complexe des accélérateurs du CERN. Dec 2008.

[22] D.R. Alves et al. (LHCb Collaboration). The LHCb Detector at the LHC. *J. Instrum.*, 3:S08005, 2008.

[23] V.V. Gligorov. Performance and upgrade plans of the LHCb trigger system. *Nucl.Instrum.Meth.*, A718:26–29, 2013. doi: 10.1016/j.nima.2012.08.076.

[24] S. Amato et al. (LHCb Collaboration). *LHCb magnet: Technical Design Report*. Technical Design Report LHCb. CERN, Geneva, 2000.

[25] P. R. Barbosa-Marinho et al. (LHCb Collaboration). *LHCb VELO (VErtex LOcator): Technical Design Report*. Technical Design Report LHCb. CERN, 2001.

[26] URL http://lhcb.physik.uzh.ch/ST/public/material/index.php.

[27] Barbosa-Marinho et al. (LHCb Collaboration). *LHCb inner tracker: Technical Design Report*. Technical Design Report LHCb. CERN, 2002.

[28] P. R. Barbosa-Marinho et al. (LHCb Collaboration). *LHCb outer tracker: Technical Design Report*. Technical Design Report LHCb. CERN, 2001.

[29] R Arink et al. Performance of the LHCb Outer Tracker. *JINST*, 9(01):P01002, 2014. doi: 10.1088/1748-0221/9/01/P01002.

[30] S. Amato et al. (LHCb Collaboration). *LHCb RICH: Technical Design Report*. Technical Design Report LHCb. CERN, 2000.

[31] Jr. Alves, A. Augusto et al. The LHCb Detector at the LHC. *JINST*, 3:S08005, 2008. doi: 10.1088/1748-0221/3/08/S08005.

[32] P. R. Barbosa-Marinho et al. (LHCb Collaboration). *LHCb muon system: Technical Design Report*. Technical Design Report LHCb. CERN, 2001.

[33] LHCb Collaboration. LHCb PID Upgrade Technical Design Report. Technical Report CERN-LHCC-2013-022. LHCB-TDR-014, CERN, Geneva, Nov 2013. URL http://cds.cern.ch/record/1624074.

[34] LHCb Collaboration. *LHCb trigger system: Technical Design Report*. Technical Design Report LHCb. CERN, 2003.

[35] R Aaij, J Albrecht, F Alessio, S Amato, E Aslanides, et al. The LHCb Trigger and its Performance in 2011. *JINST*, 8:P04022, 2013. doi: 10.1088/1748-0221/8/04/P04022.

[36] O. Callot, M. Ferro-Luzzi, and P. Perret. Using the SPD multiplicity in the Level-0 trigger. 2003.

[37] O. Deschamps, F.P. Machefert, M.H. Schune, G. Pakhlova, and I. Belyaev. Photon and neutral pion reconstruction. 2003.

[38] The Calorimeter Objects Tools Group. URL https://twiki.cern.ch/twiki/bin/viewauth/LHCbPhysics/CalorimeterObjectsToolsGroupDOC.

[39] L. Breiman, J. Friedman, R. Olshen, and C. Stone. *Classification and Regression Trees*. Wadsworth and Brooks, Monterey, CA, 1984. new edition [**?**]?

[40] Andreas Hocker, J. Stelzer, F. Tegenfeldt, H. Voss, K. Voss, et al. TMVA - Toolkit for Multivariate Data Analysis. *PoS*, ACAT:040, 2007.

[41] Yoav Freund and Robert E Schapire. A decision-theoretic generalization of on-line learning and an application to boosting. *Journal of Computer and System Sciences*, 55(1):119 – 139, 1997. ISSN 0022-0000. doi: http://dx.doi.org/10.1006/jcss.1997.1504. URL http://www.sciencedirect.com/science/article/pii/S002200009791504X.

[42] Jan Therhaag. TMVA Toolkit for multivariate data analysis in ROOT. *PoS*, ICHEP2010:510, 2010.

[43] Elliott D. Bloom and C. Peck. Physics with the Crystal Ball Detector. *Ann.Rev.Nucl.Part.Sci.*, 33:143–197, 1983. doi: 10.1146/annurev.ns.33.120183.001043.

[44] Harrison B. Prosper. Practical Statistics for Particle Physicists. pages 195–216, 2014. doi: 10.5170/CERN-2014-008.195.

[45] LHCb Collaboration. The DaVinci project. http://lhcb-release-area.web.cern.ch/LHCb-release-area/DOC/davinci/.

[46] Fergus Wilson Adrian Bevan. AFit User Guide. http://pprc.qmul.ac.uk/ bevan/afit/afit.pdf.

[47] Stefaan Tavernier. Experimental Techniques in Nuclear and Particle Physics. 2010.

ERKLÄRUNG

Ich versichere, dass ich diese Arbeit selbstständig verfasst und keine anderen als die angegebenen Quellen und Hilfsmittel benutzt habe.

Heidelberg, den 15.06.2015 ....